# AUTOMATED MACHINE LEARNING BASED ANALYSIS OF INTRAVASCULAR OPTICAL COHERENCE TOMOGRAPHY IMAGES

by

RONNY SHALEV

Submitted in partial fulfillment of the requirements

For the degree of Doctor of Philosophy

Dissertation Adviser: Dr. David L. Wilson

Department of Electrical Engineering and Computer Science

CASE WESTERN RESERVE UNIVERSITY

May, 2016

**CASE WESTERN RESERVE UNIVERSITY**
**SCHOOL OF GRADUATE STUDIES**

We hereby approve the dissertation of

**Ronny Y. Shalev**

Candidate for the degree of **Ph.D***.

Committee Chair
**M. Cenk ÇAVUŞOĞLU**

Committee Member
**David L. Wilson**

Committee Member
**Hiram G. Bezerra**

Committee Member
**Soumya Ray**

Committee member
**Francis Merat**

Date of Defense
**February 23rd, 2016**

*We also certify that written approval has been obtained

for any proprietary material contained therein

# Contents

## List of Tables

## List of Figures

**Acknowledgements**

Over the past four years I have received support and encouragement from a great number of individuals. Many thanks go to my advisor, Dave Wilson, for his advising on this research; his dedication to my work is very much appreciated. I would like to thank the members of my committee for their extreme patience in the face of numerous obstacles and for their support as I moved from an idea to a completed study. I would like to thank my fellow lab students, those who have moved on, those in the quagmire, and those just beginning, for their support, feedback, and friendship. I would also like to thank the various members of University Hospital Core Lab who were always there to answer questions and help in data collection.

Finally, and ***most importantly***, I would like to thank Annette Shalev, my wife and my best friend who not only gave me a push to start this journey but also supported me at every step of the way.

I have learned much during this period !!

## List of Abbreviations

CAD – coronary artery disease or computer aided diagnosis

DES – drug eluting stent

OCT – optical coherence tomography

IVOCT – intravascular coherence tomography

TCFA – thin cap fibrous atheroma

NSTEMI – non-ST segment elevation myocardial infarction

ECG - electrocardiogram

PCI – percutaneous coronary intervention

NIH – neointima hyperplasia

CT – computed tomography

MRI – magnetic resonance imaging

TD-OCT – time domain OCT

FD-OCT – Fourier domain OCT

SS-OCT – swept-source OCT

OFDI – optical frequency domain interferometry

SNR – signal-to-noise ratio

AMI – acute myocardial infarction

SVM - support vector machine

DAG – directed acyclic graph

Adaboost – adaptive boosting

RBF – radial basis function

ROI – region of interest

TP – true positive

FP – false positive

FN – false negative

TN – true negative

IVUS – intravascular ultrasound

PSF – point spread function

DP – dynamic programming

ROC – receiver-operating characteristic

# Automated Machine Learning Based Analysis of Intravascular Optical Coherence Tomography Images

## Abstract

by

RONNY SHALEV

Coronary artery disease (CAD) is the leading cause of death in the world. Most acute coronary events (e.g. heart attacks) are due to the rupture of atherosclerotic plaques inside the arteries, however, calcified lesion is the most widely treatable, typically, by stent implantation via percutaneous coronary intervention (PCI). Intravascular Optical Coherence Tomography (IVOCT) imaging has the resolution, contrast, and penetration depth to characterize coronary artery plaques. Conventional manual evaluation of IVOCT images, based on qualitative interpretation of image features, is tedious and time consuming. The aim of this PhD dissertation was to develop advanced algorithms to fully automate the task of plaque characterization, thereby significantly reduce image analysis time, enable intervention planning, and increase IVOCT data usability. We based our algorithms on machine learning combined with advanced image processing techniques.

We developed a processing pipeline on a 3D local region of support for estimation of optical properties of atherosclerotic plaques from coronary artery, IVOCT pullbacks. Performance was assessed in comparison with observer-defined standards using clinical pullback data. Values (calcium $3.58\pm1.74mm^{-1}$, lipid $9.93\pm2.44mm^{-1}$ and

fibrous 1.96±1.11mm$^{-1}$) were consistent with previous measurements. We, then, created a method to automatically classify plaque tissues as fibrous, calcified, or lipid-rich. For this multi-class problem, we used one-versus-rest SVM classifiers for each of the three plaque types, rules to exclude many voxels called "other," and both physics-inspired and local texture features to classify voxels. Experiments on the clinical training data yielded 5-fold, voxel-wise accuracy of 87.7±8.6%, 96.7±4.9% and 97.3±2.4% for calcified, lipid-rich and fibrotic tissues, respectively. Experiments on the independent validation data (ex-vivo image data accurately labeled using registered 3D microscopic cryo-imaging and was used as ground truth) yielded overall 87.1% accuracy indicating generalizability. This was followed by a development of a novel approach for real-time calcium segmentation. The trained algorithm was evaluated on the independent validation data. We achieved 5-fold cross validation calcium classification with $F_1$ score of 93.7±2.7%, recall of ≥89%, precision of ≥97%, and running time of 2.6 seconds per frame suggesting possible on-line use.

We conclude with an application whose purpose is to be a complementary to the cardiologist in data analysis, off-line and on-line.

# Chapter 1 Background

## 1.1 Coronary Artery Disease

Cardiovascular diseases are the leading cause of death worldwide. About 610,000 people die of heart disease in the US every year–that's 1 in every 4 deaths [1] (note that the reference was released in 2015). The underlying disease process in the blood vessels that results in coronary heart disease and cerebrovascular disease (stroke) is known as atherosclerosis. It is a complex pathological process where fatty material and cholesterol are deposited inside the lumen of medium and large-sized blood vessels (arteries). These deposits (plaques) cause the inner surface of the arteries to become irregular and the lumen to become narrow, making it harder for blood to flow through. Further, the plaque can rupture, triggering the formation of a blood clot, which may eventually lead to an obstruction of the blood vessel and an acute coronary event, a heart attack.

CAD development can start at early age. Cholesterol plaque starts to deposit in the blood vessel walls. As the person gets older, the plaque burden builds up, inflaming the blood vessel walls and raising the risk of blood clots and heart attack [2]. The plaques release chemicals that promote the process of healing but make the inner walls of the blood vessel sticky. Then, other substances, such as inflammatory cells, lipoproteins, and calcium that travel in the bloodstream start sticking to the inside of the vessel walls [3]. Eventually, a narrowed coronary artery may develop new blood vessels that go around the blockage to get blood to the heart. However, during times of increased exertion or stress, the new arteries may not be able to supply enough oxygen-rich blood to the heart

muscle. In some cases, a blood clot may totally block the blood supply to the heart muscle, causing heart attack.

## 1.2 Atherosclerotic Plaques

The most common cause of coronary thrombosis is plaque rupture followed by plaque erosion [4]. However, current practice is to treat mainly occlusions using percutaneous coronary intervention (PCI, commonly known as balloon angioplasty), aiming at improving survival and relieving patient symptoms [5]. With intervention success, there has been a trend to treat ever-more complex lesions, including chronic total occlusions [6]. Success of these complex procedures will depend upon intravascular imaging.

There are three major plaque components of atherosclerotic plaques associated with CAD: fibrous tissue, lipid pool and calcified plaques (Figure 1). Once an atherosclerotic plaque has formed, it shows the highly characteristic architecture of a fibrous cap covering a central core of extracellular lipids and debris (‘atheroma'). Fibrous tissue provides the structural integrity of a plaque. On the other hand, the atheroma is soft, weak and may rapture easily. Any combination of cap thickness and atheroma size may occur. However, the extremes at both ends of the spectrum appear to have a totally different clinical outcome. Essentially clinically stable are fibrous plaques, composed of solid fibrous tissue and only small amounts of extracellular lipid or no lipid at all. In coronary arteries most of these lesions remain clinically silent [7]. On the other hand, typically vulnerable plaques are characterized by large lipid pools and have a thin (<65μm) or virtually absent fibrous cap (often referred to as TCFA, Thin Cap Fibroatheroma).

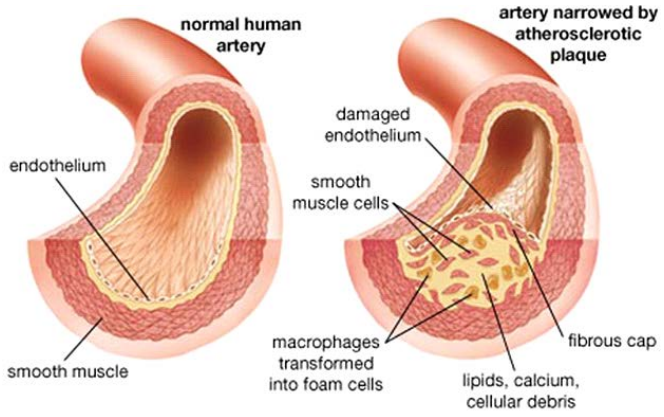


Figure 1: Comparison of healthy coronary artery (left) and coronary artery with plaque buildup (right.) (Source: http://www.pharmaceutical-networking.com/merck-mk-0524b-treatment-of-atherosclerosis/)

Calcified plaque is an important marker of atherosclerosis, and can provide an estimate of total coronary plaque burden for a patient [8-12]. However, there is no clear relationship between calcification and plaque vulnerability [13]. Calcified plaques are mechanically stiff and heavily calcified lesions can result in under-expansion of coronary stents where current treatment of occlusions (PCI) highlight the need for Intravascular Optical Coherence Tomography (IVOCT). First, there is a need to guide plaque modification. The presence of calcium is the strongest factor affecting "stent expansion," a well-documented metric for clinical outcome [14, 15]. IVOCT provides the location, circumferential extent, and thickness of calcium. Angiography gives no such details. IVUS detects calcium but gives no information about thickness, as the signal reflects from the front surface. As interventional cardiologists tackle ever-more complex vascular lesions and use bioresorbable stents, there is a recent growing interest in using atherectomy devices for lesion "preparation" (i.e. grinding away hardened plaque narrowing the lumen). Since there is a substantial economic cost and risk of complications with atherectomy [16], we should un-blind physicians with IVOCT and provide them with improved assessment of the need for atherectomy and with angular

location for “directed” atherectomy. Second, there can be a geographic miss, where the stent either misses the lesion along its length or is improperly expanded, affecting its ability to stabilize the lesion and/or provide appropriate drug dosage. There is well-documented impact on restenosis [17] . Plaque dissections at the edge of a stent clearly visible in IVOCT were detected by angiography in only 16% of cases [18]. Plaque dissection at the edge of the stent happens almost exclusively in areas with eccentric calcium/lipid [18], characteristics only available with intravascular imaging. Under IVOCT guidance, one can use a longer stent or apply a second stent to reduce effects of geographic miss. Third, plaque sealing is the treatment of a remote lesion that is insignificant (<50% stenosis) but that may appear vulnerable under intravascular imaging. Because approximately 50% of coronary events after stenting happen at remote, non-stented sites, plaque sealing is an attractive concept under investigation in trials. IVOCT’s high sensitivity for lipid plaque will be advantageous for guidance of plaque sealing.

The goal of this work is to develop automated algorithms for plaque characterization from intravascular OCT (IVOCT), for the purpose of creating a powerful tool for live-time treatment planning of coronary artery interventions and for off-line assessment of drug and biologic therapeutics. We do it in three ways: (i) reduce the effort involved, (ii) improve the accuracy of high-risk plaque identification and (iii) make the diagnosis available as early in the process as possible. The prevalence of atherosclerosis means achieving these goals can have a major impact on health worldwide.

## 1.3 Imaging Technologies for Assessing CAD

The complex atherosclerotic disease process is frequently not reflected in the luminal silhouette generated by modalities, which are commonly referred to as non-invasive modalities, such as CT that reliably distinguishes calcified plaque; MRI, which assesses plaque in larger vessels; and radionuclide imaging, which uses various imaging agents to image vascular inflammation. However, most intravascular lesions silently develop over a long time before they obstruct the lumen and direct imaging of the vessel wall has become a new goal in the assessment of CAD progression and prevention. Intravascular ultrasound (IVUS) represents the first clinical imaging technique enabling routine tomographic imaging of coronary arteries [19]. Unfortunately, the microscopic features that characterize vulnerable plaque are not reliably identified by IVUS [20-22].

Several other technologies were tested [23], however no method to date has been shown to reliably identify all of the characteristic features of the intravascular lesions. There are research-only, emerging intravascular imaging techniques including photoacoustic [24], fluorescence lifetime [25], and combined systems: IVOCT-NIR [26], IVOCT-IVUS [27], etc. Of all of the methods, IVOCT is the best clinically available candidate for plaque characterization at the time of intervention.

## 1.4 Optical Coherence Tomography (OCT)

OCT is a minimally invasive, high-resolution (<10μm axial; 20-40μm lateral resolution) imaging modality that has been developed for the identification of vulnerable plaque [28-30]. It generates cross-sectional images of tissue microstructure to penetration depths approaching 2mm [31]. Among a number of imaging modalities that have been

investigated for studies of cardiovascular diseases, only OCT provides sufficient resolution to visualize the majority of clinically important microstructures of atherosclerotic plaques [32]. OCT acquires cross-sectional images of tissue reflectance and, since it may be implemented through an optical fiber probe, it is readily adaptable to coronary catheters [33] for insertion into coronary arteries and circumferential imaging of arterial pathology creating the idea of Intravascular OCT (IVOCT). IVOCT is an optical analog of intravascular ultrasound (IVUS) that can be used to examine the coronary arteries and has 10-fold higher resolution than IVUS; by measuring the delay time of optical echoes reflected from subsurface structures in biological tissues, structural information can be obtained. Because of the high speed of light propagation in tissue, the time delay of the returning light is measured using low-coherence interferometry where light reflected or backscattered from inside the specimen is measured by correlating with light that has traveled a known reference path. Consequently, IVOCT can differentiate tissue characteristics (fibrous, calcified, or lipid-rich plaque).

There are two types of OCT (Figure 2), the first generation, called time domain (TD)-OCT [31, 34], and second-generation frequency domain (FD)-OCT [35-38], also known as optical frequency domain imaging (OFDI) [37, 39], which has advantages that currently make it the preferred technique in interventional cardiology.

In TD-OCT systems, a broadband light source is split into a reference arm, directed onto a mirror, and a sample arm that directs the light into the artery wall. When the distance travelled by the light in each arm of the interferometer is within the coherence length of the source, the returning light, once recombined, will form an interference pattern. The amplitude of the detected interference pattern is subsequently

mapped to a pixel intensity value corresponding to the discrete axial location, or depth, within the tissue. To generate image information for an entire axial (i.e. along the A-line direction) depth profile, the reference mirror is translated, altering the optical path length of the reference arm, and hence the imaging depth inside the sample. Systematic scanning of the imaging beam across the tissue can be performed to build 2-dimensional and 3-dimensional images. Because of the strong attenuation of light by blood, OCT systems require the removal of blood during OCT examinations.

In FD-OCT/OFDI, rather than utilizing a broadband light source and a mechanically translating reference arm, interference is generated using a rapidly tuned wavelength swept source and a stationary reference arm [37]. Each frequency component of the detected interference signal is associated with a discrete depth location within the tissue. To generate an A-line, Fourier transform is used to convert the interference information to depth resolved reflectance [37]. FD-OCT system has a faster frame rate and pullback speed, making the OCT procedure more user-friendly and not requiring proximal balloon occlusion.

As for most catheter-based optical imaging modalities, it is necessary to clear blood from the imaging field of view to obtain information on the artery wall because blood scatters and attenuates light. IVOCT has been successfully demonstrated in vivo using either a flush with an optically transparent media such as saline or radiocontrast, or combined flushing with proximal balloon occlusion. While effective for displacing blood, the nonocclusive method only provides a limited view of the vessel, containing few images, and balloon occlusion may be associated with myocardial ischemia and chest pain during the procedure [40, 41].

The second-generation OCT, FD-OCT, has, to a large part, solved the blood limitations of TD-OCT. In 2003, FD-OCT/OFDI [35, 36, 38] was shown to have a sensitivity advantage over TD-OCT. This realization led to the development of second-generation intracoronary OCT systems that perform OCT imaging at significantly higher frame rates than TD-OCT, and with superior image quality [37]. When used in conjunction with a saline/radiocontrast flush and rapid helical pullback scanning of the catheter, FD-OCT/OFDI makes it practical to conduct 3-dimensional (3D) OCT imaging of long coronary artery segments without balloon occlusion [39, 42]. The fast pullback rate (10 to 20mm per second) allows the injection of only a small amount of contrast media to clear the artery, therefore greatly reducing the risk of ischemia. Intracoronary OFDI is now poised to become a widely used imaging modality in interventional cardiology. In fact, intracoronary TD-OCT has been performed on thousands of coronary patients at several hundred sites around the world and, with the recent FDA approval of intracoronary FD-OCT systems in the United States, it is anticipated that these numbers will greatly increase. In addition, due to its relatively slow image acquisition speed, the TD-OCT allows visualization of only a short segment of the vessel following proximal balloon occlusion or nonocclusive saline or contrast agent flush. Taking advantage of the high detection sensitivity of FD-OCT, comprehensive imaging of a long coronary segment in vivo was demonstrated with a short and nonocclusive flush [39]. Three-dimensional (3D) visualization of coronary microstructures reconstructed from comprehensive intracoronary imaging became possible and has been utilized as a useful complementary tool to the 2D cross-sectional OCT images.

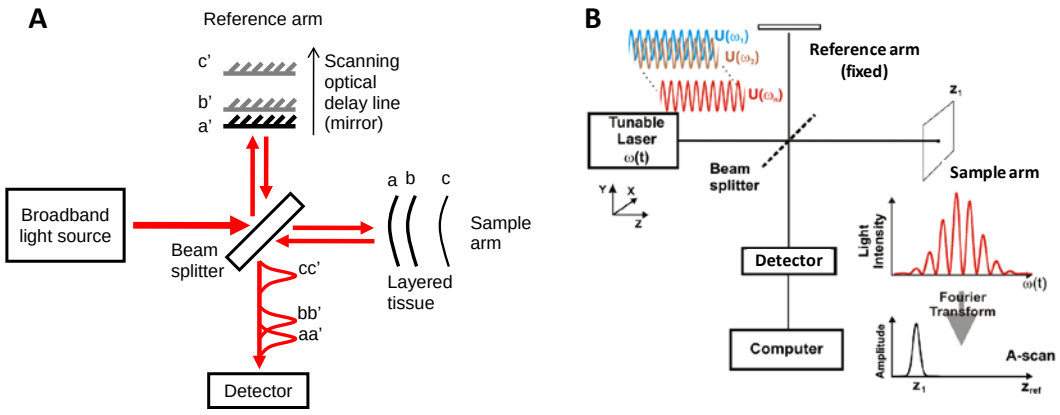


Figure 2: Diagrams of the two types of OCT machine. (A) Time domain OCT, TD-OCT and (B) swept-source OCT FD-OCT. TD-OCT scans different depths by physically moving a reference arm. FD-OCT measures interference by sweeping the optical frequency. Interference is obtained as a function of frequency and image is reconstructed by taking the Fourier Transform of the detected signal. (Source: http://archive.nrc-cnrc.gc.ca/eng/projects/ibd/oct.html)

IVOCT has demonstrated that it can provide images of superior resolution when compared to IVUS and allowed visualization of features not seen by ultrasound [43], such as the intima, including intimal flaps and defects, disruptions in the media, and stent strut apposition. Generally, the three systems (TD-OCT, FD-OCT and IVUS) differ in several respects, as described by Bezerra et al. [44] (summary shown in Table 1). The resolution of OCT (10-20 μm) is about 10-fold higher than that of IVUS (to 100-150 μm), but the maximum depth of tissue penetration, when no plaque is present, is lower with OCT (1-2 mm) than with IVUS (4-8 mm). Another important difference is related to the strong attenuation of light by blood, which originates from two sources: absorption by hemoglobin and scattering by red blood cells. As described before, to examine coronary arteries, blood must first be removed during an OCT examination to eliminate massive scattering of light by red blood cells.

| Specifications | IVUS | TD-OCT | FD-OCT |
|---|---|---|---|
| Axial resolution, μm | 100-150 | 15 | 10-15 |
| Lateral resolution, μm | 150-300 | 90 | 20-40 |
| Frame rate, fps | 30 | 15-20 | 200 |
| Pullback speed, mm/sec | 0.5-2.0 | 3 | 20 |
| Scan diameter (FOV), mm | 8-10 | 6.8 | 6-11 |
| Tissue penetration, mm | 4-8 | 1-3 | 2-3.5 |

Table 1: Comparison of IVUS and first-generation time-domain (see below) OCT (sources: [44, 45])

Since its initial demonstration, IVOCT has been used extensively by a number of investigators in the clinical realm for assessing coronary plaque features [46-50], stent placement [51-53]), apposition [50, 51, 54], stent strut coverage [55-59] (Figure 3) and thrombus [60]. It has been used to image microstructural features of the artery wall in a number of post-mortem studies where the image data can be directly correlated to histopathology, the gold standard [23, 32, 61-65]. These studies document the development and validation of image criteria for detecting features that correspond to tissue microstructures with high sensitivity and specificity. The detected microstructural features include macrophages [62, 65], cholesterol crystals [23, 64], red and white thrombus [43, 61], calcium deposits [32, 63], fibrous plaques [32, 63], and lipid-rich plaques [32, 61, 63]. These studies have provided the foundation necessary for the interpretation of intracoronary OCT images.

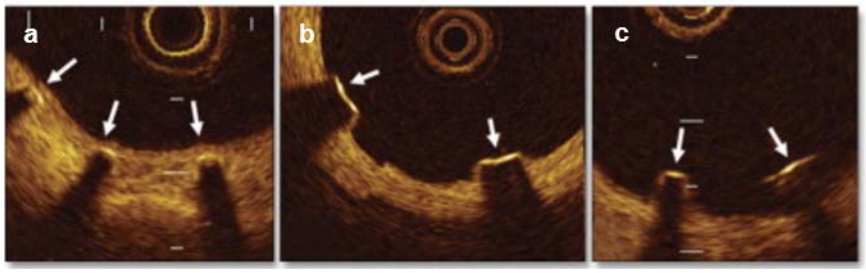


Figure 3: Stent classification using IVOCT images: (a) Well-apposed with neointimal coverage (arrows). (b) Well-apposed without neointimal coverage (arrows). (c) Malapposed without neointimal coverage (arrows)

"The use of intravascular IVOCT to date has been primarily investigational, and therefore its clinical use warrants further exploration" [66]. Despite the greatly improved resolution compared to IVUS, the penetration depth of OCT is limited in lipid-containing plaque, and therefore, the full thickness of the artery wall may, in some cases, not be visible. As a result, certain measurements that require visualization of the external elastic membrane, such as plaque burden (a measure of the stenosis severity), cannot be reliably performed with OCT. Despite this limitation, it is expected that OCT use will increase and will complement or even replace IVUS for many clinical applications, including thrombus and superficial plaque characterization, evaluating the results of stent placement, lesion coverage, apposition of stent struts to the vessel wall, and edge dissections.

## 1.5 IVOCT in Intravascular Imaging

IVOCT has been used in research and clinical application solving numerous analysis problems. IVOCT has been shown to discriminate fibrous, lipid-rich, and calcified plaques [32, 42, 43]. It has been validated against histology for accurate measurement of cap thickness and tissue composition (fibrous, calcific, lipid-rich/necrotic) [23, 32, 67-69].

Validation of TCFA by OCT against histology has shown excellent sensitivity (100%) and specificity (97%) but limited positive predictive value (41%) [70]. It can also detect macrophage accumulations, plaque rupture, micro-calcifications, neovascularization, and thrombus [71]. Macrophage accumulations can be visualized by OCT as signal-intense punctuate regions with strong signal attenuation [71]; quantification of macrophage accumulations within fibroatheroma caps has shown good correlation with human histology [65]. The specificity of detecting macrophages defined as 'bright spots' (not necessarily with shadowing) at any location in the artery wall is lower due to components seen elsewhere in the intima that also appear as bright spots in OCT (e.g. cellular fibrous tissue, calcium-fibrous tissue interfaces, micro-calcifications, cholesterol crystals) [72]. Optical coherence tomography can also detect micro vessels that have been correlated with plaque progression and vulnerability [73]. This may enable better treatment decisions to be made based on detailed morphologic information, which may result in better interventional outcomes [74, 75].

IVOCT has been widely used in clinical trials to assess the efficacy and safety of stent designs [76, 77]. With superior resolution, sensitivity and imaging speed, IVOCT has enabled visualizing delicate vessel structures and arterial healing after stent implantation [43, 78, 79]. Our group has developed advanced computational approaches for analyzing stents using IVOCT images [80-82]. Lu et al. [80, 83], applied bagged decision trees as the classifier on initial screen of candidate struts, and achieved promising results in the a small number of validation set. Such classification-based methods can take advantage of human expert knowledge, and can easily combine multiple features for decision making. Later on, Lu et al. [81] employed a more

advanced approach by using feature extraction and classification techniques to facilitate stent detection robustly. In a follow up study, Wang et al. [84] used a Bayesian network based upon physical principles of OCT imaging and computed a probability of stent strut appearance in an A-line. Second, they exploited stent wire continuity from adjacent frames and proposed a novel method based on graph algorithms to detect the stent strut locations in an en-face view. Further, they considered the physical stent model and localized the depths of all the stent struts in a pullback simultaneously using a graph cut algorithm. By doing so, Wang et al. took into consideration the continuity of stent wires or the 3-D cylindrical shape of stents and created a more robust technique. The success level of the evaluation of these studies (algorithm evaluation was done with >20,000 images) where results has shown to be as good as, or better than, experts on very tough problems in IVOCT stent analysis, caused us to approach machine plaque characterization with confidence.

In this PhD dissertation, however, since some of the above analyses are subjective and probably unimportant for intervention decision-making, we do not focus on them. The focus of this PhD dissertation is on the aspect of IVOCT image analysis as a means to support treatment decision making via automatic plaque characterization of the three main plaque types (calcium, lipid, and fiber).

## 1.6 Plaque Characterization Using IVOCT

IVOCT has a significant opportunity to improve percutaneous interventions. Physicians perform these procedures under x-ray angiography and fluoroscopy, which show the vessel lumen and maybe a hint of potential calcifications, but nothing more. As

a result, cardiologists are treating vessels blind to the actual location, extent, and constituents of vascular lesions, especially when there is remodeling. Significant lipid or calcium deposits can affect the treatment plan. If initial balloon inflation does not expand a calcified artery, the physician applies high pressure, performs atherectomy, or aborts, all tough decisions needing imaging support. In the case of lipid, a physician can extend a stent to seal off the affected area or at least avoid placing the stent edge in a lipid region, an occurrence that raises the risk of vascular dissection. Successful live-time IVOCT plaque characterization/visualization software would greatly aid treatment planning. Two reports document that IVOCT before stenting changes perception and strategy of treatment in a majority of cases for experienced users [85, 86]. First, in a 60-day study with 150 patients at our site, we found a remarkable 82% of angiography-based strategies were altered following consideration of IVOCT [86]. Over 9% of cases had a TCFA at the edge of a lesion, where one would extend a stent to limit additional injury. Second, in the 418-patient, multicenter ILUMIEN I trial, pre-PCI IVOCT altered the procedure plan in 57% of stenoses [85].

The main approaches to perform quantitative studies of coronary atherosclerosis are: manual analysis, semi-automatic analysis where an interaction with the clinician is required to achieve the desired results, and fully automatic analysis.

Manual analysis suffers from three main disadvantages. First, while a number of studies demonstrate that experienced observers can identify plaque and wall borders in IVOCT images that agree with histology and angiography [87], the utility of analysis approaches relying upon manual border identification is limited by the need for observers with substantial experience and by the tedious nature of manual tracing. Second, the

manual analysis approach suffers from another disadvantage, accuracy. Third, the significant inter-observer variability is a limiting factor in accuracy.

The manual analysis' shortcoming has been shown to be very significant at times. In [88] it is shown that when three analysts independently assessed the minimum cap thickness of the same 14 lesions, at least one of them gave a different call on TCFA in 10 out of 14 lesions. In this experiment, three expert analysts where given the same 323 cross-sectional images from the same 14 lipid-rich lesions. Each analyst independently selected the image frame where they suspected the FC was thinnest and determined the FC thickness by a single measurement. Subsequently, all 323 cross-sectional images from the same 14 lipid-rich lesions were manually segmented by analyst 1 and by the computer algorithm. The accuracy of the computer algorithm was evaluated by comparison with the manual segmentation. In order to assess intra-observer variability, all images were re-analyzed by operator 1 two weeks later. To assess inter-observer variability of manual segmentation of FC boundaries, 50 randomly selected cross-sections were analyzed by operators 2 and 3. At all times, each analyst was blinded to the analysis results performed by the other analysts and the computer algorithm. Only the common region of FC selected by all three analysts was used for comparison. If the FC was blocked by the guide wire shadow, only the shadowed region was excluded for validation.

Development of methods for automated identification of lumen and plaque structures has been limited by the relatively poor quality of intravascular ultrasound images [89]. Even with the recent substantial improvements in imaging catheters and signal processing hardware, accurate and robust segmentation of IVOCT images presents a very challenging problem, partly due to artifacts such as residual blood etc. Studies

correlating in-vitro and in-vivo IVOCT measurements with histology and angiography [32, 47] suggest that experienced observers can identify important luminal and mural structures. These studies suggest that when combined with appropriate a priori knowledge, the information necessary to perform such identification is present in the image data. This observation together with our accumulated experience developing robust numerical analysis and machine learning methods approaches to medical images forms the impetus for the current work.

## 1.7 Machine Learning

### *1.7.1 Overview*

Machine learning is the study of algorithms that that improve their performance as they are given more data [90]. It plays an emerging role in the medical imaging field, including computer-aided diagnosis (CAD), image segmentation, image registration, image fusion, image-guided therapy, image annotation, and image database retrieval. Machine learning tasks are typically classified into three broad categories: supervised, unsupervised and reinforcement learning. In supervised machine learning the computer is presented with example inputs and their desired outputs, given by a "teacher" or an expert, and the goal is to learn a general rule that maps inputs to outputs. In unsupervised machine learning, no labels are given to the learning algorithm, leaving it on its own to discover the hidden patterns in the data. In reinforcement learning, a computer program interacts with a dynamic environment in which it must perform a certain goal (such as driving a vehicle), without a teacher explicitly telling it whether it has come close to its goal [91].

In this thesis, the vast amount of data calls for automated methods of data analysis, which is what machine learning provides. In particular, we make specific use of supervised and unsupervised machine learning algorithms depending on the task at hand. We define machine learning as a set of methods that can automatically detect patterns in data, and then use the uncovered patterns to estimate novel data, or to perform other kinds of decision making under uncertainty. We refer to a machine learning algorithm as an “classifier”. We adopt the view that the best way to solve the challenges we face is to use the tools of probability. In our specific application, uncertainty comes in the form of what is the best model to explain the data? In this thesis we will describe the machine learning approach used for the specific task within each of the individual chapters.

### *1.7.2 Feature Selection*

Given a very large number of features which exist in medical images, it is customary to reduce dimensionality and remove noisy (i.e. irrelevant) and redundant features. Dimensionality reduction techniques can be categorized mainly into feature extraction and feature selection. Feature extraction approaches project features into a new feature space with lower dimensionality and the new constructed features are usually combinations of original features. Examples of feature extraction techniques include Principal Component Analysis (PCA) [92], Linear Discriminant Analysis (LDA) [93] and Canonical Correlation Analysis (CCA) [94]. On the other hand, the feature selection approaches aim to select a small subset of features that minimize redundancy and maximize relevance to the target such as the class labels in classification. Representative feature selection techniques include Information Gain [95], Relief [96], Fisher Score [97] and Lasso [98]. Both Feature extraction and feature selection are capable of improving

learning performance, lowering computational complexity, building better generalizable models, and decreasing required storage. Feature extraction maps the original feature space to a new feature space with lower dimensions by combining the original feature space. It is difficult to link the features from original feature space to new features. Therefore further analysis of new features is problematic since there is no physical meaning for the transformed features obtained from feature extraction techniques. While feature selection selects a subset of features from the original feature set without any transformation, and maintains the physical meanings of the original features. In this sense, feature selection is superior in terms of better readability and interpretability. In this thesis, depending on the task, we apply the concept of feature selection where we employ both the physics of IVOCT image formation and image analysis to compute features from 3D regions within the IVOCT pullback volume.

### *1.7.3 Evaluating classifier performance*

Learning the parameters of a prediction function and testing it on the same data is a methodological mistake: a model that would just repeat the labels of the samples that it has just seen would have a perfect score but would fail to predict anything useful on novel (yet-unseen) data. This situation is called overfitting. To avoid it, it is common practice when performing a (supervised) machine learning experiment to hold out part of the available data as a test set. Note that the word “experiment” is not intended to denote academic use only, because even in commercial settings machine learning usually starts out experimentally.

When evaluating different settings (“hyperparameters”) for classifiers, there is still a risk of overfitting *on the test set* because the parameters can be tweaked until the

classifier performs optimally. This way, knowledge about the test set can "leak" into the model and evaluation metrics no longer report on generalization performance. To solve this problem, yet another part of the dataset can be held out as a so-called "validation set": training proceeds on the training set, after which evaluation is done on the validation set, and when the experiment seems to be successful, final evaluation can be done on the test set. However, by partitioning the available data into three sets, we drastically reduce the number of samples which can be used for learning the model, and the results can depend on a particular random choice for the pair of (train, validation) sets. A solution to this problem is a procedure called cross-validation (CV for short). A test set should still be held out for final evaluation, but the validation set is no longer needed when doing CV. In the basic approach, called *k*-fold CV, the training set is split into *k* smaller sets. The following procedure is followed for each of the *k* "folds":

- A model is trained using *(k – 1)* of the folds as training data;
- The resulting model is validated on the remaining part of the data (i.e., it is used as a test set to compute a performance measure such as accuracy).

The performance measure reported by *k*-fold cross-validation is then the average of the values computed in the loop. This approach can be computationally expensive, but does not waste too much data (as it is the case when fixing an arbitrary test set), which is a major advantage in problem such as inverse inference where the number of samples is very small. We further improve on the regular CV approach and perform leave-one-pullback-out (LOPO) validation. Although this approach repeats the same logic as the CV approach described above, there is one important difference: the left out set is not randomly selected from the dataset but is chosen such that all samples belong to the same

pullback are held out. This represents a much more realistic condition in our application, thus is a better indication of the classifier's ability to generalize. The above two approaches are summarized in the following table.

| | |
|---|---|
| *k*-fold CV | Randomly split training set, D, into K folds (K disjoint sets)<br>Initialize the error, $E_{cv}$ to some high value<br>for k=1:K<br>1. hold the fold k as the validation set, $D_{cv}$ and the others as the training set, $D_t$<br>2. train using $D_t$<br>3. predict error on $D_{cv}$, $E_{cv}$ and record it.<br>4. Save model corresponding to average $E_{cv}$<br>end |
| LOPO | For n=1:N<br>1. Use sample *n* as the validation set (making sure all points belong to the same pullback), $D_{cv}$, and the other N-1 as training set, $D_t$<br>2. train using $D_t$<br>3. predict error on $D_{cv}$, $E_{cv}$<br>end |

Table 2: CV and LOO validation algorithms. The LOO approach has significant advantage since it represents a much more realistic condition.

### *1.7.4 Learning Curve and Performance Measures*

Every machine learning classifier has its advantages and drawbacks. Typically, an classifier is trained on a training set that is as large as possible, and evaluated on an independent test set [99]. It is expected that more training data results in a better performance of the classifier, because with more data the parameters of a classifier can be estimated more reliably. A learning curve (Figure 4) shows the change in classification error for a varying training set size. Often not only the true error is estimated, but also the apparent error, i.e. the error on the training set as opposed to the validation set. When the difference between the apparent error and the true error (also referred to as "generalization error" or "validation error" and is calculated using an independent validation set) is large, the classifier is called ***overtrained***, or ***overfitted***. The performance

on the training set gives a too optimistic estimate on what can be expected in practice. We can decompose the generalization error in terms of ***bias***, ***variance*** and ***noise***. The bias of an classifier is its average error for different training sets. The variance of an classifier indicates how sensitive it is to varying training sets. Noise is a property of the data.

We plot the learning curve and show the classification (true) and training error (apparent error) of a classifier for varying numbers of training samples. This enabled us to extrapolate if our classifier may gain significantly in performance when more training data is added. Therefore, we use it as a tool to find out how much we benefit from adding more training data and whether the classifier suffers more from a variance error or a bias error. If both the validation error and the training error converge to a value that is low with increasing size of the training set, we will not benefit much from more training .

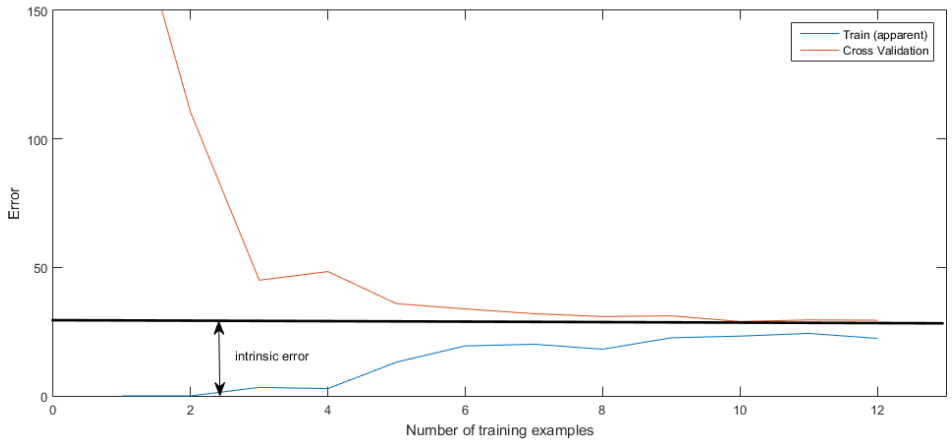


Figure 4: Learning curve illustration

### *1.7.5 Machine Learning That Matters*

A final note on the proposed machine learning approaches taken in this work addresses the issue of the considerable efforts we made in order to make the tests (described above) be applicable to real world problems. A lot of current machine learning research has lost

its connection to problems of importance to the “real world”. From this perspective, there exist limitations in the data sets investigated, the metrics employed for evaluation, and the degree to which results are communicated back to their originating domains [100] (in our case, Cardiology). We made all possible efforts in order to test our results using data from clinical settings and avoided using evaluation of the new algorithms on a handful of isolated benchmark data sets. Rather than phrase our challenge in the form of a pure mathematical objective function to be optimized, we tried to ask a question of larger scope: what is the Cardiologist’s objective function? We wanted to characterize the progress of our algorithms in a meaningful way rather than simply maximize performance on isolated data sets. This was not always easy, given that we work in an academic environment, thus, at times, limited by time, expertise or both.

## 1.8 Thesis Overview

In this thesis, advanced image processing techniques, supervised and unsupervised machine learning algorithms, large database of manually annotated blood vessel plaques (in the Core Lab), large amount of cryo-images and blood vessel are all combined to develop highly automated software for comprehensive analysis of IVOCT pullbacks. The rest of this dissertation is organized as follows. Chapter 2 describes algorithms for computation and verification of optical properties of the three main plaque types in the blood vessel using a blood vessel phantom. Chapter 3 describes a complete pre-processing pipeline developed for the purpose of improvement of automated plaque classification. In chapter 4 we propose to use Support Vector Machine (SVM) as a classifier that can be used for off-line plaque classification. In chapter 5 we use a

different approach and develop a close-to-real-time calcium classification algorithm. Chapter 6 introduces the software which developed targeted towards on-line and off-line automated IVOCT image analysis software based on the algorithms developed in the previous chapters. Finally, we summarize and discuss future work in Chapter 7.

# Chapter 2 Validation of parameter estimation methods for determining optical properties of atherosclerotic tissues in intravascular OCT

## 2.1 Introduction

Intravascular optical coherence tomography (IVOCT) is an invaluable tool for vascular assessments due to its high contrast and microscopic resolution. It has been shown that IVOCT is able to distinguish between lipid, calcium, and fibrous plaques [32, 43], quantify microscopic features such as macrophage content [65], and aid in assessment of new coronary artery stent designs [83, 101]. However, fast IVOCT systems can produce 500+ image frames in a single 2.5s pullback scan, resulting in an explosion of image data which can be very difficult and labor intensive to analyze manually, thereby precluding measurements from every image frame. We are developing computational methods for automatically classifying tissue types in order to address many of the aforementioned challenges. Our methods employ both the physics of image formation and image analysis to compute features from 3D regions within the IVOCT pullback volume, which will then be employed for an automated and highly precise tissue classification as a follow up study.

There have been previous studies relating to tissue identification and classification in OCT images [32, 61, 75, 102, 103]. Yabushita et al. [32] published a qualitative plaque classification scheme where he describes fibrous plaques as characterized by homogeneous, signal-rich regions; calcium plaque by well-delineated, signal-poor regions with sharp borders; and lipid-rich plaques by signal-poor regions with diffuse

borders. Kume et al. [61] have demonstrated *in vivo* evaluation of the different types of plaques with IVOCT but argues that interpretation of OCT images based on qualitative criteria alone might be ambiguous. Xsu et al. [102] used transverse imaging of ex vivo arteries using a high-resolution OCT microscopic system. They imaged fixed tissue sections of coronary arteries and calculated attenuation and backscattering coefficients based on average of 400 –lines (over time). Using single scattering light model, they performed least squares fitting of log compressed data. They were able to discriminate numerically between the different plaque types. Using a catheter based system and a stationary acquisition. Van Soest et al. [75] measured $\mu_t$ in both *in vivo* and *ex vivo* specimens. They corrected for the non-ideal imaging system, used a linear equation model on *log* compressed data and applied an elegant algorithm to determine regions in one dimension corresponding to a single, homogenous tissue type. They argued in favor of $\mu_t$ values as a function of depth within tissue.

In this study, we develop a method for assessing optical properties of tissue from 3D pullbacks, the standard clinical acquisition method for IVOCT data. In this way, we can avoid the second injection of contrast agent to clear the lumen for a stationary acquisition. We operate on a volume of interest (VOI) consisting of about 20-50 A-lines spread across the angle of rotation ($\theta$) and along the artery, $z$. This presents many challenges including eccentricity of the catheter relative to the lumen surface, catheter motion, etc. We meet this challenge using multiple processing steps including pixel shifting, noise reduction, and robust estimation. Results from the new pullback analysis method are statistically compared to those from a more traditional, “gold standard,”

stationary acquisition. In order to do this in a controlled fashion, we use a realistic artery phantom containing multiple “tissue types”.

## 2.2 Methods

### *2.2.1 Image acquisition and selection of volumes of interest (VOIs)*

Images were collected with the C7-XR system from St. Jude Medical Inc., MA. The swept source OCT system had a 1310*nm* center wavelength, 110 nm wavelength range, 50 kHz sweep rate, 20 mW output power, and ~12 mm coherence length. For pullbacks, the nominal speed was 20 mm/s over a length of 54 mm, resulting in a 100 fps frame rate and 271 frames per pullback. For stationary data acquisition, 121 frames were recorded with the catheter stationary at a predetermined location.

The optical tissue phantoms used in this experiment are described in detail in [104, 105]. These phantoms were carefully fabricated with tightly controlled optical parameters allowing us to use them as gold standard while assessing clinically viable pullback data. Three phantoms were used in this experiment. Each phantom simulated one type of plaque (lipid, fibrous, and calcium) with known optical characteristics. For stationary imaging, the phantom was placed in a water bath and immobilized. The imaging catheter was moved along the lumen until the site of interest (containing phantom plaque) was identified. Then, the catheter sheath was held firmly on both sides to avoid any motion artifacts and five stationary acquisitions were obtained for each phantom. For pullback acquisitions, the same process as above was repeated except that we recorded 271 frames over a pullback length of 54mm (at 20mm/s) along the segment of phantom tissue. The protocol for *in vivo* imaging is described in [106].

The method used for identification of VOI's by an expert is detailed in [106]. The criteria used during human expert VOI identification is described in [1] (fibrous plaques were characterized by homogeneous, signal-rich regions; calcified regions by signal-poor regions with sharp borders; and lipid plaques by signal-poor regions with diffuse borders). TCFA was the most challenging type of plaque to identify [107]. The expert used the A-line intensity profile for each of the A-lines of the VOI while paying most attention to the separation between the lipid pool and the thin cap inside the signal-rich region described in [102].

In the stationary phantom acquisitions, there were 15 datasets in all (5 data sets for each plaque type). In these datasets, the expert marked between 5 and 20 VOIs depending on the plaque type and image quality. Markings were similarly done on the pullback data.

## 2.3 Image Analysis Algorithms

### *2.3.1 IVOCT Pipeline*

The processing pipeline used in our IVOCT image data analysis consisted of the following steps:

1. Pre-process in r-θ view: Correct for catheter optics.
2. Remove Speckle noise using enhanced Lee filter [108, 109] on 2D r-θ images introducing minimum bias while preserving the sharp intensity level changes.
3. Determine and remove baseline.
4. Pixel-shift A-line within VOI’s ensemble.
5. Log compress the data.

6. Average across time to obtain an averaged image (stationary sequences).
7. Compute parameters using robust estimation approach.[106]

This procedure is shown graphically in Figure 5.

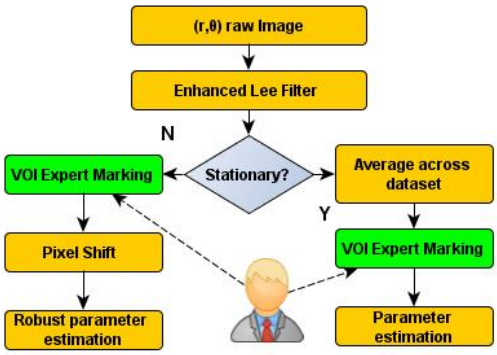


Figure 5: graphical illustration of (r-θ) pipeline processing. The green indicates human operation while the rest is performed by our software.

**Noise Characterization and Removal**

Speckle in IVOCT is a multiplicative noise and is a major challenge in analysis of optical properties [75, 110, 111]. To reduce speckle, we used the so-called enhanced Lee filter [108] , which assumes multiplicative noise.

We first determine if noise in IVOCT data is multiplicative in nature [112]. An observed pixel value $z_i$ is related to the noise-free pixel, $x_{i,j}$,

$$z_{i,j} = x_{i,j} v_{i,j} \tag{2.1}$$

where $v_{i,j}$ is a multiplicative noise with mean 1 and variance σv. We will analyze this relationship using methods described in [112]. Briefly, assume that the signal process x and the noise v are not correlated, the mean of z is $\bar{z} = \overline{xv} = \bar{x}$ . And the variance of *z* is:

$$\mathrm{var}(z) = E\left[(xv - \overline{xv})^2\right] = E\left[x^2\right]E\left[v^2\right] - \bar{x}^2\bar{v}^2$$

If we examine an ensemble of pixel data or a flat region with fixed $x$ value, $E[x^2] = \bar{x}^2$ and the variance reduces to:

$$\text{var}(z) = x^2\left(E\left[v^2\right] - \bar{v}^2\right) = \bar{x}^2\sigma_v^2$$

from which we get:

$$\sigma_v = \frac{\sqrt{\text{var}(z)}}{\bar{x}} = \frac{\sqrt{\text{var}(z)}}{\bar{z}} \tag{2.2}$$

In other words if the model described in (2.1) fits the IVOCT data, then the standard deviation, $\sigma_v$ should equal the ratio of the standard deviation of $z$ and the mean of $z$.

**Speckle Noise Distribution**: In order to get the speckle noise distribution we computed a histogram from an average r-θ frame of an intralipid pullback (obtained by averaging across frames of the pullback) truncated to only include pixels to the right of the catheter line. Statistical analysis revealed that the distribution from water pullback. Then three additional VOIs were selected from different water pullbacks in order to confirm the initial findings. Since the data does not fit a normal distribution, a classical Lee filter [113] would introduce bias in our measurement. Therefore, we implemented the enhanced Lee described in [108] that is more appropriate for data from a Rayleigh distribution.

**Enhanced Lee Filter (ELEE)**: The ELEE as described in [108] reduces speckle while preserving texture information. It is an adaptation of the Lee filter and similarly uses local statistics (coefficient of variation) within individual filter windows. Each pixel is put into one of three classes, which are treated as follows:

- Homogeneous region: The pixel value is replaced by the average of the filter window.
- Heterogeneous region: The pixel value is replaced by a weighted average of the neiberhood pixels.
- Point "pixel": The pixel value is not changed.

**Baseline Analysis**

We analyzed the baseline, which we define as the noise floor of the intensity level. To do that we used two approaches. In both, we employed the model described in [75]:

$$I_d(r) = I_0 T(r) S(r) \exp(-\mu_t r) + I_{offset} \tag{2.3}$$

Taking the natural log of both sides of equation (2.3) yields:

$$\ln\left[\frac{(I_d(r) - I_{offset}(r))}{(T(r; z_0, z_R) S(r))}\right] = \ln(I_0) - \mu_t r \tag{2.4}$$

For the stationary phantom images, we applied the speckle removal algorithm described above to all 121 frames and averaged them. From the average r-θ frame, we computed a horizontal profile (i.e. along r) and identified a region within the vessel wall where the signal fell off to a minimum level, giving us the required offset to use in the model. For the pullback, however, we used pullback dataset, where, rather than measure the noise along *r*, we selected an angle of an A-line. Then we created an image across the pullback direction composed of all of the A-lines having the same angle in each of the pullback r-θ frame. The average of this image gave us the desired baseline.

**Pixel shift Correction**

In an ideal pullback, the catheter would be fixed at the center of the lumen and would, therefore, appear as a straight line in r-θ view (assuming that the vessel is perfectly circular). In addition, the A-line's shape would look ideal as described by equation (2.3). However, typically, the catheter moves during a pullback and therefore its distance from the vessel wall is continuously changing. If an image is "corrected" by "sliding" the A-lines such that the lumen border is a straight line in an r-θ frame, it would weight equally any two points that are at the same depth within the vessel. Also, all of the A-lines within an expert-marked VOI would be at the same distance from the catheter. We call this process "pixel shift correction".

The steps in pixel shift correction are: (i) compute lumen border (using dynamic programming), and (ii) shift pixels of each A-line in an r-θ frame such that the vessel wall becomes a straight line. The red peaks in Figure 6 represent the reference point from which the exponential attenuation occurs for each A-line (i.e. where the intensity is $I_o$) and the blue illustrates the lowest point. The flat blue is the baseline level after baseline offset correction as described above.

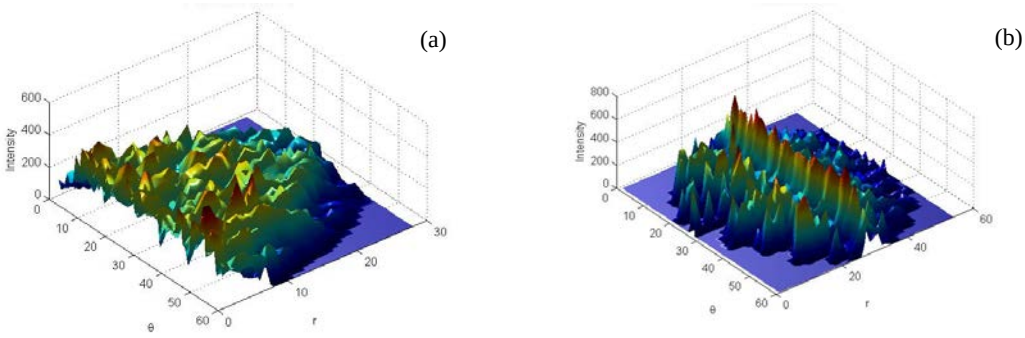


Figure 6: A VOI before (a) pixel shift and after (b). Indices along the axes are index numbers

## 2.4 Results

Results of the baseline analysis for stationary acquisition were such that an intensity level of approximately 6.7 (mean) was considered as baseline so that images were corrected by subtracting the baseline, dividing each A-line by the imaging system model and any negative values were truncated to zero. For the pullback, we received roughly the same values; however, we expect that in a clinical pullback, results will be different since there the fluids will contain a lot more scatterers than in water (blood/saline mixture).

Next, we analyzed the noise characteristics. The noise distribution is found to be a Rayleigh distribution with noise variance $\sigma_v$ being constant and it is equal to 0.14994. An example of what an image looks like before and after speckle noise removal is shown in Figure 7.

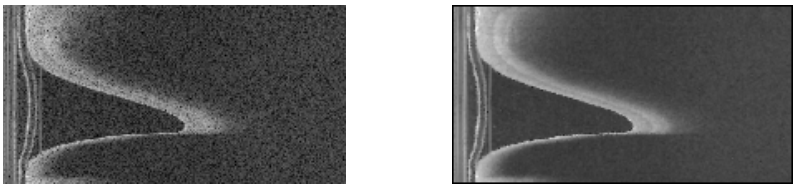

Figure 7: Illustration of an r-θ frames before (left) and after (right) speckle removal.

In Table 3 below we show a comparison of results of parameter estimation on 15 stationary phantom data sets of all three plaque types as a function of the processing steps in the pipeline. Approximatelly 20 VOIs were used for each plaque type. We first analyze calcium plaques. Without any processing, μt for calcium has a large uncertainty (expressed as larger standard deviation). After enhanced Lee filtering application, the uncertainty of $\mu_t$ is greatly reduced with insignificant bias. When we pixel-shifted and averaged the A-lines, we observed that no additional bias was introduced, and uncertainty

is significantly reduced (i.e. lower standard deviation, lower *cv*). Next, we studied lipid plaques. With no processing, we see a large uncertainty in μt but with a much lower *cv*. When we processed the frame using the same steps as before, we observe a progressively reducing *cv*. In fact, *cv* is much lower than that for calcium, indicating very high precision of $\mu_t$. Last, we analyze fibrous plaques, where we see that due to noise removal and other steps, *cv* is significantly lowered indicating very high precision of $\mu_t$. The data of Table 3 is shown graphically in Figure 8 for all plaque types.

| | Raw | | | Extended Lee Filter | | | Pixel-shift & Averaging | | |
|---|---|---|---|---|---|---|---|---|---|
| | $\mu_t$ | σ | cv | $\mu_t$ | σ | cv | $\mu_t$ | σ | cv |
| Calcium | 3.882 | 2.022 | 0.521 | 3.805 | 1.570 | 0.413 | 3.800 | 1.094 | 0.288 |
| Lipid | 10.842 | 0.515 | 0.048 | 11.218 | 0.507 | 0.045 | 11.025 | 0.417 | 0.038 |
| Fibrous | 7.083 | 2.199 | 0.310 | 5.980 | 1.818 | 0.304 | 6.080 | 1.337 | 0.220 |

Table 3: Attenuation coefficient ($\mu_t$) results of stationary dataset numerical analysis in the different pipeline stages (σ is the standard deviation and *cv*=σ/mean is the coefficient of variation)

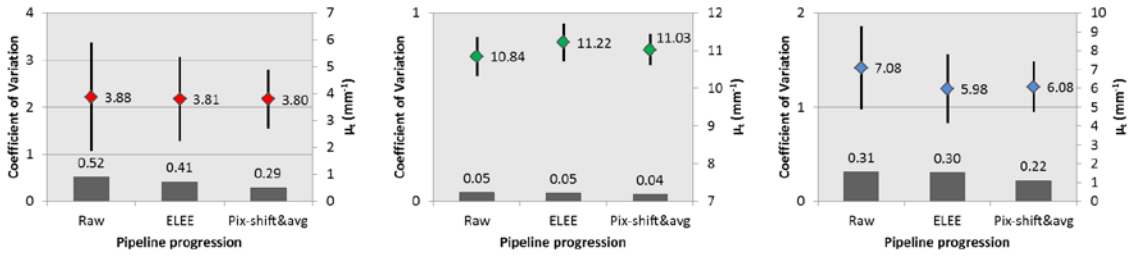


Figure 8: $\mu_t$ estimates as a function of processing steps in the processing pipeline for different tissue types using stationary acquisition. Going from left to right we see calcium, lipid and fibrous.

We now compare our results so far with phantom pullbacks. Looking at Figure 9 we observed that the average $\mu_t$'s were very similar to those for the stationary, however the uncertainty was higher. Pullbacks introduce other sources of noise such as motion, speed variations and other machine related disturbances during measurements. However, the nice thing is that the average value of the $\mu_t$ for each of the tissue types remain relatively constant, thus confirming that the robust estimation method used to calculate

the optical values for the pullback, yielded the same results as the stationary acquisition where the more traditional method (averaging across the pullback and then across θ) was used.

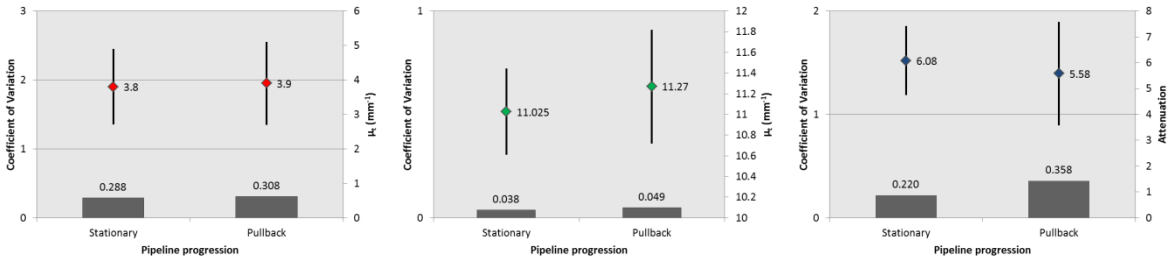


Figure 9: Stationary vs. pullback: $\mu_t$ uncertainty (right y-axis) and coefficient of variation (left y-axis). Calcium is

## 2.5 Discussion

Characterization of atherosclerotic plaques is extremely important for determining the risk of a cardiovascular event. However, manually analyzing 100's of frames of IVOCT image data and accurately making clinical decisions needs a high level of expertise and an inordinate amount of time. An automated approach will be a great step in the right direction; however, discrimination of atherosclerotic plaques using a computer algorithm is still not accurate enough for use in a clinical setting as a support system for decision making. Our results indicate an improved accuracy and precision as compared to previously reported approaches for optical parameter estimation. Furthermore, this study may enable us to determine morphological features of coronary plaques that are at risk of rupture. In this study, phantoms were employed to obtain a "gold standard" against which to compare clinical results. Phantoms have also proved useful for establishing the best set of processing steps needed for a fully automated IVOCT data analysis. We applied the widely used sigma (Lee) filter to be useful for IVOCT image analysis. No

consistent bias was observed in any of the pipeline stages, which is encouraging. Our results have indicated an improvement in image quality, robustness in estimation, improved visualization of hard-to-analyze data, and an improved feature space clustering that would aid in unsupervised learning. For stationary phantom data, calcified and lipid plaques exhibit roughly the same average intensity (signal poor regions), however, the high attenuation of the lipid and the low attenuation of the calcium help us to distinguish between the two. The homogeneity of fibrous plaque is expressed by a low attenuation coefficient, while a high value of the average intensity indicates that it is signal rich. When we compared stationary phantoms with pullback phantoms, we observed that estimates were numerically comparable however the spread (standard deviation) for pullbacks was slightly higher due to motion artifacts during pullback.

Next, we acknowledge some of the limitations in our approach. The results highly depend on the quality of the expert marking. In fact, Kume et al. [61] show that when using IVOCT, evaluation of the different types of plaques could be possible *in vivo*, however, they also argue that interpretation of OCT images based on qualitative criteria alone might be prone to errors and ambiguities. In this study, computation efficiency was not considered. Using parallel processing and GPU might make a significant difference in compute times; this is reserved for a future study. Fibrous plaques thinner than 25μm were not marked. Many artifacts such as catheter uniformity, polarization effect, and blood clearance may influence the reproducibility of optical parameters estimation. In addition, we would also like to note that that although we performed the noise analysis in an intralipid bath, this will not be representative of a clinical pullback noise since when performing a clinical pullback, the characteristics of the contrast agent (or the saline)

which may be mixed with blood, might be different. Therefore, the same analysis must be performed on a clinical data as well.

We developed a framework for plaque characterization using three distinctive features, the attenuation coefficient, the average intensity and the incident intensity of VOI. We used expert-marked VOIs from stationary phantom data, estimated optical parameters, and compared with pullback data. We introduced the concept of IVOCT image pipeline analysis and applied an enhanced Lee filter to remove speckle noise. Results suggest that the aforementioned features are suitable for highly accurate plaque type discrimination, enabling automatic classification. Machine learning algorithms can further exploit regional image features from IVOCT images such as texture and shape-based features.

# Chapter 3 Processing to determine optical parameters of atherosclerotic disease from phantom and clinical intravascular OCT 3D pullbacks

## 3.1 Introduction

Intravascular optical coherence tomography (IVOCT) is a catheter-based, high-resolution imaging method that has demonstrated considerable application for assessments of vascular disease due to its high resolution and contrasts. IVOCT is able to distinguish between lipid, calcium, and fibrous plaque [32, 43, 102, 114], and aid in assessment of new coronary artery stent designs [83, 101, 114, 115]. Newer IVOCT systems can acquire more than 500 image frames in a single 2.5 second pullback scan, making it possible to image a complete artery volume in a few seconds [39, 116]. Although experts can classify tissue types using consensus rules [32, 89], there are sometimes regions in vessels which can confound the experts, especially if only a single frame is viewed. Moreover, it takes considerable training to become an expert reader, and there is significant potential for inter-reader variability, especially across sites and time. As a result of the volume of IVOCT data and difficulty in interpretation, it can be very difficult to interpret live-time in the catheterization suite or to analyze manually offline for research applications. We are developing computational methods for automatically classifying tissue. Our methods employ both the physics of image formation and image analysis to compute tissue optical features from 3D regions within the IVOCT pullback volume, which can then be employed for automated tissue classification.

There have been previous studies relating to tissue identification and classification in OCT images [32, 61, 75, 102]. Yabushita et al. [32] published a qualitative plaque classification scheme where fibrous plaques are characterized by homogeneous, signal-rich regions; calcium plaque by well-delineated, signal-poor regions with sharp borders; and lipid-rich plaques by signal-poor regions with diffuse borders. These descriptions later were accepted as the consensus [71] and are used as such in this research. Kume et al. [61] have demonstrated *in vivo* evaluation of the different types of plaques with IVOCT but argues that interpretation of OCT images based on qualitative criteria alone might be ambiguous. Xu et al. [102] used transverse imaging of *ex vivo* arteries using a high-resolution OCT microscopic system. They imaged fixed tissue sections of coronary arteries and calculated attenuation and backscattering coefficients based on average of 400 lines (over time). Using single scattering light model, they performed least squares fitting of log compressed data. They were able to discriminate numerically between the different plaque types. Using a catheter based system and a stationary acquisition, Van Soest et al [75] measured $\mu_t$ in both *in vivo* and *ex vivo* specimens. They corrected for the non-ideal imaging system, used a linear equation model on *log* compressed data and applied an elegant algorithm to determine regions in one dimension corresponding to a single, homogenous tissue type. They argued in favor of $\mu_t$ values as a function of depth within tissue. These reports are encouraging, and results should be improved with robust, 3D estimation of optical properties and with full accounting of tissue structural characteristics. In a preliminary study, we used 3D spiral pullback acquisitions (rather than stationary acquisitions) obtained during a single blood clearing operation to estimate optical properties of atherosclerotic plaques within 3D volumes of interest (VOIs) [106].

In this chapter, we propose an improved processing pipeline for estimating optical properties from 3D intravascular OCT (IVOCT) pullbacks. We introduce multiple enhancements as compared to previous reports from others [28, 75, 102, 117, 118] and our own report [106]. Improvements include, speckle noise reduction, baseline signal computation, and catheter eccentricity correction. Due to noise in a single A-line from a pullback, we estimate parameters from a collection of A-lines nearby in space, both within a polar ($r$-$\theta$) image and across image frames in $z$. We evaluate the methodology using both a silicon-matrix vascular phantom and clinical pullback data. In experiments on homogenous phantoms, we compared results from stationary and pullback acquisitions, evaluated precision and accuracy of measurements, and investigated potential effects of oblique sensor orientation and distance from the lumen on parameter estimates.

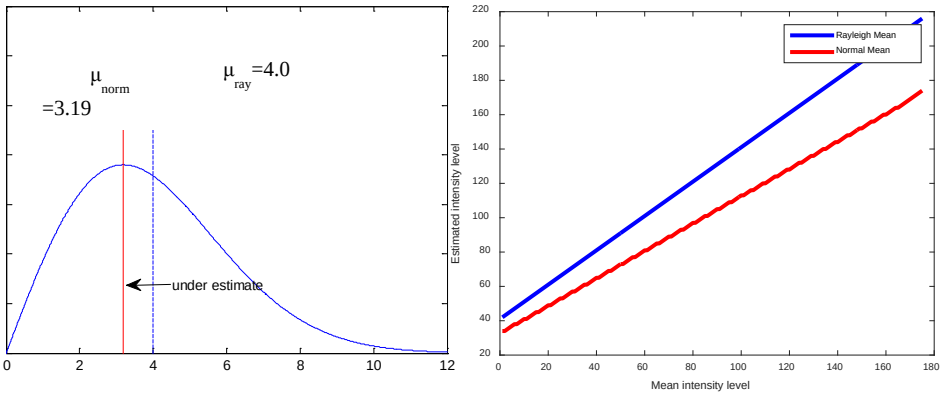


(a) (b)

Figure 10: Bias of Lee filter that is fixed with the enhanced version. (a) Probability density function (pdf) of image data from an IVOCT acquisition with Rayleigh distribution mean, $\mu_{ray}$ =4.0. Assumption of a normal distribution ignores values in the Rayleigh tail and gives a $\mu_{norm}$= 3.2. (b) Variation in normal and Raleigh means as a function of intensity.

## 3.2 Algorithms and Data Analysis

We describe our processing pipeline and algorithms for estimating optical properties in 3D IVOCT pullbacks. Starting with raw (linear) data in the ($r$-$\theta$) view, the processing pipeline consisted of the following steps.

1. Reduce speckle noise using the enhanced Lee (ELEE) filter that accounts for the statistical distribution of noise.
2. Estimate and subtract the intensity baseline.
3. Correct for non-ideal imaging system response.
4. Segment lumen border using dynamic programming as described in [119].
5. Spatially adjust pixels to account for catheter eccentricity.
6. Apply natural logarithm of intensities to linearize exponential attenuation.
7. Estimate optical parameters using 3D robust least square fitting technique.

Some are described in more detail below.

### *3.2.1 Speckle noise characterization and reduction*

We filtered IVOCT images to reduce speckle, multiplicative noise [112, 120], a major challenge in the analysis of optical properties [110, 111]. We used the enhanced Lee (ELEE) filter on IVOCT images, which accounts for the multiplicative nature of speckle noise [109, 121]. The ELEE filter is an adaptation of the Lee filter and uses local statistics within a processing window to adaptively filter. We used a rectangular window in (r-θ) with the width along $\theta \geq 2$ times the width in r. We compared results to those from the traditional Lee filter used by us previously [106]. The traditional LEE assumes normally distributed multiplicative noise [108]. It replaces the center pixel of the kernel

with the average of the pixel values within 2σ of the center pixel value. For the IVOCT application, LEE suffers from two drawbacks: that (for a case with mean = 4) the original 2σ range would shift the original mean value to $\mu_{norm}$, a value smaller than the true mean, causing an intensity under-estimation. Thus, if one realizes that as the intensity level is higher, then the under estimation is higher (Figure 10b), it is clear that it has direct impact on the attenuation values: It is especially apparent with lipid since lipid-rich plaques start with very high intensity rapidly decreasing to signal poor region. To illustrate, if the start of a 0.14 mm long A-line within a lipid VOI has intensity value of, say 4095 and at the end of the A-line the intensity value is 1000, then using Eq. (3.2), we compute the attenuation to be 10.7 $mm^{-1}$. However, if the under-estimation at the start of the VOI causes us to estimate it at, say, 3500 and at the end of the VOI we still estimate it at 1000, then the attenuation would be computed as 8.94 $mm^{-1}$. The second major drawback of the traditional Lee filter is that regions with very small variation in intensity (small sigma) are not filtered. In the extreme case, of zero intensity, the sigma range is zero, and the pixel would remain unfiltered. These two problems are addressed by ELEE. Within the window, each pixel is put into one of three classes, which are treated as follows:

- Homogeneous: The pixel value is replaced by the average of the filter window.
- Heterogeneous: The pixel value is replaced by a weighted average.
- Point pixel: The pixel value is not changed.

For a more detailed description of the filter please see [108].

We numerically analyzed the effect of ELEE as compared to LEE (see Results). The ELEE filter performance was evaluated using signal-to-noise ratio (SNR), an established speckle-reduction performance metric [110, 122, 123] as defined by Gonzalez

[123]: $SNR = 10\log_{10}\left(\max\left\{I^2\right\}/\sigma^2\right)$, where $I$ is the linear magnitude image and σ is the variance of $I$ in a background noise region. To exemplify the improvement in the SNR we created several background images (taken from the region beyond beam penetration) to compute the noise standard deviation. We then created the same number of images from regions which included meaningful information to get average intensity values (I).

### *3.2.2 Baseline*

To find the value of the baseline intensity value, we arbitrarily selected a $\theta$ value and averaged all A-lines along the pullback direction ($z$) corresponding to this $\theta$ in a pullback. Using lumen segmentation as described later, we selected a segment beyond the beam penetration depth (> 2mm) in tissue. Any segment that was too short was ignored. The average intensity value within this ($r$-$z$) plane gave us the baseline. We expected some variation in the computed baseline value for different $\theta$'s, therefore, in order to account for this variation; we repeated the above steps for several randomly selected θ values and picked the median value. The baseline value determined was subtracted from the OCT signal (see Eq. (2.5)), where any negative values were set to zero.

### *3.2.3 IVOCT signal model and catheter correction*

We used a commonly used model below to describe the OCT measurement [106]. In the equation below, the OCT signal is attenuated in an exponential fashion with the total attenuation constant, $\mu_t$. Remaining components describe the non-ideal imaging system response. The equation is:

$$I_d(r) = I_0 T(r) S(r) \exp(-\mu_t r) + I_b \tag{3.1}$$

where *T(r)* is the confocal function and *S(r)* is the Gaussian Coherence function [75], accounting for the spectral coherence of the source in Fourier domain OCT with parameters $Z_w$ and $Z_c$ as given below.

$$T(r) = \left[ \left( \frac{r - Z_0}{Z_R} \right)^2 + 1 \right]^{-1/2}, \text{and } S(r) = \exp\left[ -\left( \frac{r - Z_c}{Z_w} \right)^2 \right]$$

where $Z_0$ is the position of the beam waist and $Z_R$ is the Rayleigh length. We estimated parameters from model fits to IVOCT imaging data obtained in a low lipid concentration solution where attenuation is negligible, as described in [106]. Parameters used where: $Z_C$ and $Z_W$ were obtained from the specifications of the light source and their values were $Z_C$ = 0mm and $Z_W$ = 12mm. The parameters $I_0$, $Z_0$, and $Z_R$ for the typical catheter were calculated to be: $I_0$ = 154.93, $Z_0$ = 10.57 mm and $Z_R$ = 0.59 mm. Following division of the imaging system response, we are left with the equation below.

$$I_d(r) = I_0 \exp(-\mu_t r) + I_b \tag{3.2}$$

### *3.2.4 Pixel shift correction for oblique incident beam*

In an IVOCT pullback, the catheter is often not at the geometric center of the lumen. This eccentricity gives rise to variations in the distance to the lumen boundary in the ($r$-$\theta$) view. Since we do 3D processing rather than A-line processing, it is important to correct these variations to better align tissue structures. We segment the lumen border as suggested by Zhao et al. [119] with a slight modification where we make it a two-pass process: First pass, we implement the cost function as suggested by Zhao et al. along an A-line. In the second pass we fine tune the lumen segmentation by computing the same cost function along the line perpendicular to any lumen segment (found in the first pass)

that is close to being a horizontal line (±5$^o$). This process has shown improvements mainly where the lumen appears as a close-to-horizontal line in the *r-θ* view. For each A-line, we record the distance from the catheter to the lumen border and then shift the A-line along r by an integer number of pixels to place the lumen border at r=50. We use integer pixel shifting to avoid interpolation and record the distance so that we can recreate the actual distance from the catheter to any pixel in the IVOCT data set. The result of this process is a new image with a lumen border consisting of a straight vertical line.

### *3.2.5 Estimation of optical properties*

Following all processing above, we took the natural log of both sides of Eq. (3.2):

$$\ln\left[I_d(r)\right] = \ln(I_0) - \mu_t r$$

This gave a linear equation with unknowns $ln(I_o)$ and $\mu_t$. We applied a linear least squares fit to each separate A-line within a VOI. We computed medians and recorded this as our $I_0$ and $\mu_t$ estimates for the VOI. We termed this algorithm LSQM.

### *3.2.6 Plaque Classification*

We performed an exploratory classification study. We applied a two-class support vector machine (SVM) classifier and for similarity function we used the Gaussian radial basis function kernel (RBF) which assigns a label, $y \in (positive, negative)$. We used a one-versus-all approach for multi-class classification of the three plaque types (calcium, lipid and fibrous).

We optimized SVM parameters, C and γ. The Gaussian kernel variance, γ, defines how far the influence of a single training example reaches, with low values meaning "far" and high values meaning "close." The regularization parameter, *C*, trades off misclassification of training examples against simplicity of the decision surface. A low C makes the decision surface smooth, while a high C aims to classify all training examples correctly. We optimized these parameter using grid search and cross validation. We tried different pairs of (C, γ) values and the one with the best cross-validation accuracy was selected. We found that exponentially growing sequences of C and γ gave a good, practical search, i.e., $C = 2^{-5}, 2^{-3}, \ldots, 2^{15}$, $\gamma = 2^{-15}, 2^{-13}, \ldots, 2^{3}$.

Following standard nomenclature, we use TP (true positives), FN, FP, and TN to make assessments of precision, P=TP/(TP+FP), recall, R=TP/(TP+FN), and $F_1$=2PR/(P+R). $F_1$ is the harmonic mean of precision and recall and ranges between zero and one. That is, if *R* or *P* is zero, $F_1$ will be zero, and if both are one, $F_1$ will be one, the ideal value.

## 3.3 Experimental Methods

### *3.3.1 Image Acquisition*

Clinical images were selected from the database available at the Cardiovascular Core Lab of University Hospitals Case Medical Center (Cleveland OH), working with our institution. The images consist of 35 IVOCT pullbacks of the Left Anterior Descending (LAD) and the Left Circumflex (LCX) coronary arteries of patients acquired prior to stent implantation. All OCT images used in this study were acquired by commercial Fourier Domain OCT systems (C7-XRTM OCT Intravascular Imaging System, St. Jude

Medical Inc., St. Paul, Minnesota). It has axial resolution of about 15μm. The scan characteristics of the system are: 50,000 lines/s, 504 lines/frame, yielding 100 fps and 20 mm/s pullback speed yielding a 200 μm frame interval. The pullback length was 54 mm.

The optical tissue phantoms used in this experiment are described in detail in [104, 105]. These phantoms were carefully fabricated with tightly controlled optical parameters allowing us to use them as "gold standard" while assessing clinically pullback datasets. Three phantoms were used in this experiment. Each phantom simulated one type of plaque (lipid, fibrous, and calcium) emphasizing their homogeneity across the simulated plaque as described in [104]. For stationary imaging, the phantom was placed in a water bath and immobilized. The imaging catheter was moved along the lumen until the site of interest (containing phantom plaque) was identified. Then, the catheter sheath was held firmly on both sides to avoid any motion artifacts and five stationary acquisitions were obtained for each phantom. For pullback acquisitions, the same process as done with in-vivo acquisition as performed along the segment of phantom tissue.

### *3.3.2 VOI Selection*

After acquiring both phantom and clinical images, we asked an expert (a cardiologist at our partner hospital) to label volumes of interest (VOIs) as belonging to one of the three plaque types in the images. The expert marked the VOIs of a particular plaque type using freehand brush strokes. On the clinical images the expert annotated 311 VOIs (roughly equal number from each plaque type) on a total of 287 clinical images and 75 phantom images. On the phantom images he marked 20 VOIs of each type taken from 15 phantom pullbacks. VOIs were of various sizes and shapes. Most consisted of 2-5 image frames, 50-200 A-lines, and 20-50 sample points in each A-line.

## 3.4 Results

Processing pipeline parameters were chosen in exploratory experiments. Dynamic programming parameter was the connectivity window = 25. With this connectivity value, phantom data were always segmented correctly and clinical data were correct in over probably 98% of frames, and any small errors due to connectivity did not negatively affect results. ELEE parameters were scanning window size=11x7 pixels in the θ and r detections, respectively, (θ, x, *r*) and damping factor, D=1.0 (damping factor controls the smoothing of the algorithm). This window size aspect ratio embodies the idea that the data along the θ direction contains more information than that in the *r* direction.

Example phantom and clinical IVOCT images are shown in Figure 11. Clinical images show the classic characteristics of tissue types where calcium shows sharp edges, low reflectivity and low attenuation, lipid shows diffuse edges, high reflectivity and high attenuation and fibrous shows high reflectivity and low attenuation. Phantom images have features similar to the clinical images. However, they are less noisy with reduced speckle noise owing to homogeneity of the phantoms.

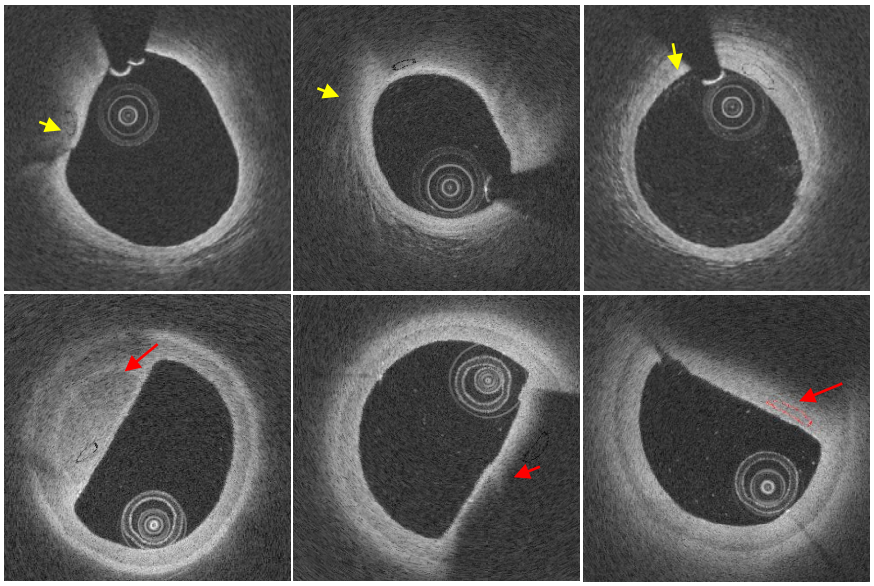

Figure 11: Appearance of atherosclerotic tissue types. Top row are clinical images where A is calcium, B is lipid and C is fibrous. On the bottom row, phantom images are shown where D is calcium E is lipid and F is fibrous.

The baseline intensity level, $I_{b,}$ was quite consistent. It was determined to be 6.7±3.8 over 15 pullbacks on the same number of different catheters. We modeled the OCT signal as Lambert-Beer exponential decay function, with the addition of baseline $I_b$ to account for noise and other sources that elevate the expected signal value (Eq. (3.2)). The justification for using this model is exemplified in Figure 12.

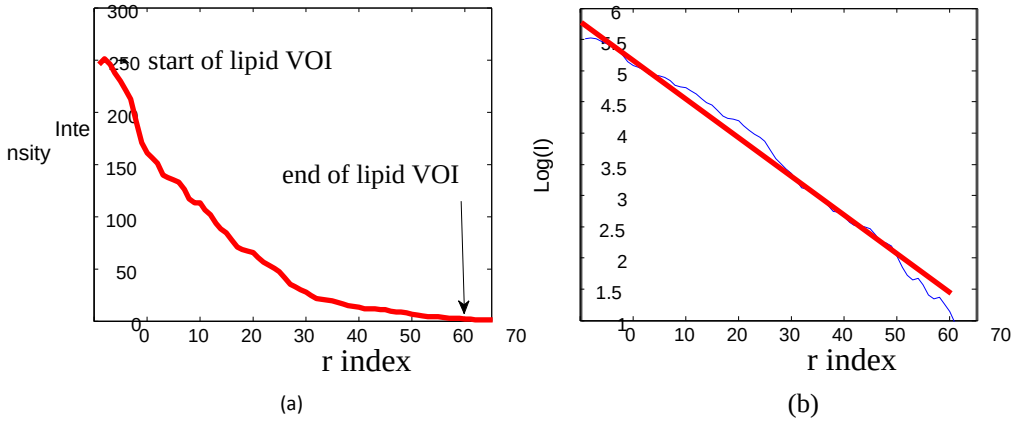


Figure 12: Linearity of A-line averaged over 100 frames in a stationary acquisition from a phantom. Linear data in (a) is processed with all the steps including catheter correction, baseline subtraction, and log, giving the result in (b). Data in (b) is well fit by the linear model used in our analysis (red line) with $\mu_t$=12.24mm$^{-1}$. Data were obtained from a homogeneous "lipid" region in the phantom image.

Visual inspection of the images before and after filtering (Figure 13) shows clear impact. The SNR for the filtered image was calculated to be 15.604 db and that of the image prior to filtering was calculated to be 12.03db. To evaluate the model assumptions for clinical IVOCT data, we created a histogram of intensity values in an ($r,\theta$) frame of a clinically obtained pullback. Statistical analysis confirmed that the distribution from the pullback was negative exponential distribution [112, 120, 124].

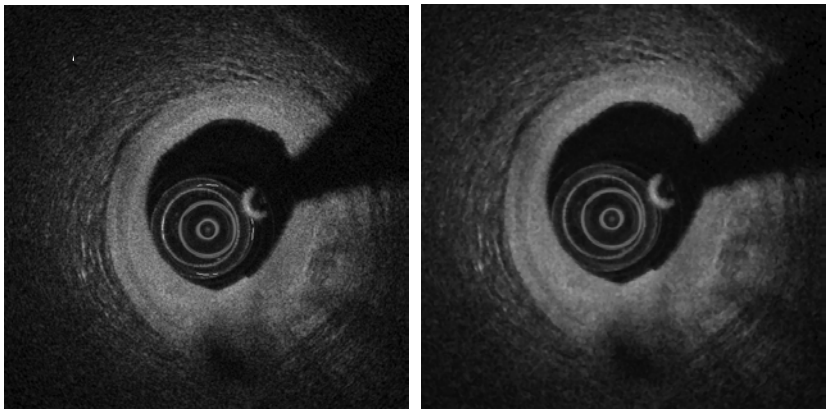

Figure 13: Clinical image (A) before filtering (SNR=12.03 db) (B) after filtering (SNR=15.604 db). A significant visual improvement after speckle reduction using the enhanced Lee filter.

We first measured IVOCT optical parameters using the same approach (to enable comparison) where an expert annotated VOIs on individual sequential frames of both phantom stationary acquisition frames and phantom pullback frames. After going through the pre-processing steps as described above, parameters estimated from different VOIs and data acquisitions were quite consistent (Figure 14 and Table 4). In this controlled setting, we also assessed potential effects of the angle of the beam incidence, $\theta_i$, and depth in tissue, as measured by the distance to the lumen, on $\mu_t$ estimates (Figure 15). Plots show little effect and statistical tests indicated no significant effect of angle or tissue depth. In Figure 14, histograms of pullback measurements show that the spread of $\mu_t$ estimates is greater than that for stationary data. Since the parameter estimation was done in a similar fashion we can assume that the small difference between the two types of acquisition is probably due to the pullback.

As an additional validation paradigm, we compared our $\mu_t$ results to estimates obtained in the standard way from stationary acquisitions. In the standard approach we acquired five data sets from each of the three phantoms and averaged over 100 frames in each instance. We marked 5 VOIs in the piecewise homogeneous phantoms, and

estimated parameters from the low noise VOIs. Means across different VOIs were very similar, indicating no bias, and a student t-test has indicated insignificant differences between the new and standard method.

We then, compared the phantom pullback estimates with clinical pullback estimates (Table 5). We observed that estimates from clinical dataset were consistent with phantoms, but with a larger spread.

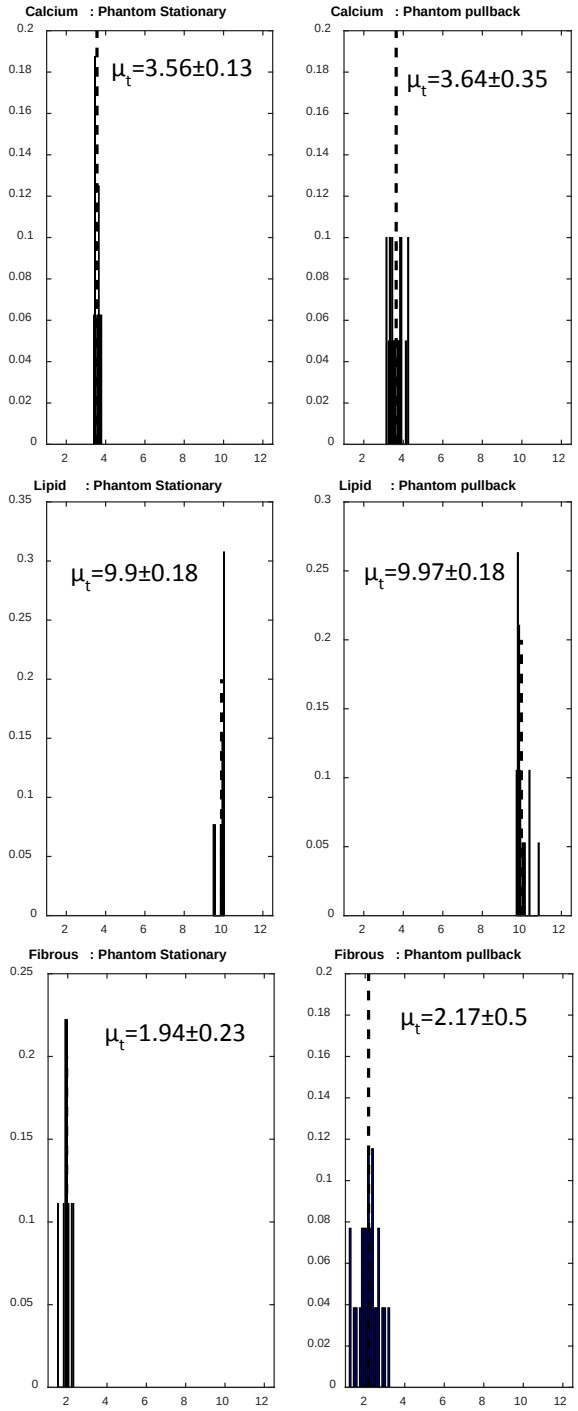


Figure 14: Comparison of μt estimates of the phantom as estimated using stationary and pullback acquisitions. Mean values for simulated calcium, lipid, and fibrous tissues are similar. The stationary acquisition gives a tighter distribution of values and smaller standard deviation than pullback acquisitions. The values are shown to belong to the same distribution (using t-test, p-values are shown in Table 4). Vertical axis is the fraction of A-lines with attenuation value given on the x axis)

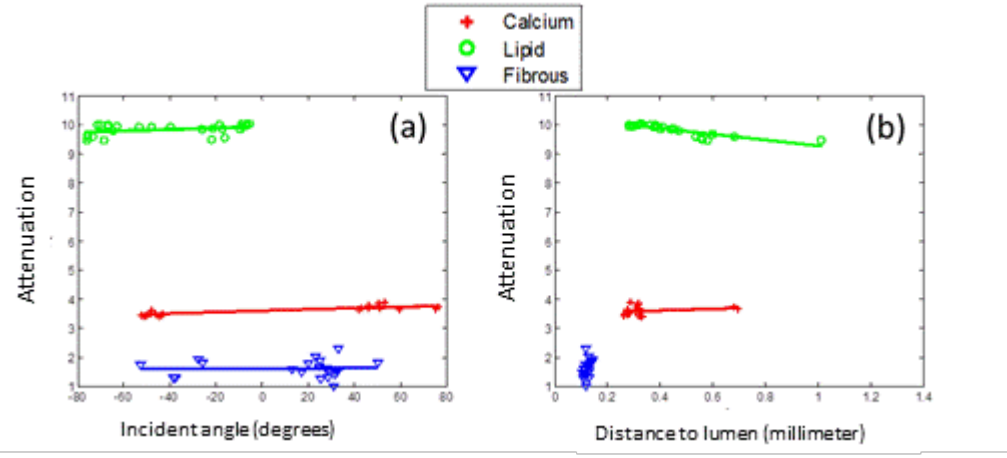


Figure 15: Independence of $\mu_t$ estimates on angle of incidence, $\theta_i$ (a) and depth, measured from the lumen (b) for a stationary acquisition dataset. The (approximately) horizontal lines indicate that regardless of the independent variable's value (i.e. distance or angle), the $\mu_t$ remains constant. In the case of fibrous tissue, due to the plaque's narrow width it was not possible to select VOIs at varying distances from the lumen, thus it appears as highly aggregates cluster. Furthermore, in (a) there appear to be two clusters. This is due to the fact that incident angles (positive and negative) were always in the indicated range.

Table 4: Results of attenuation coefficient estimates (mean of the median estimates) along with uncertainty estimates (standard deviation) computed for phantom stationary acquisition and phantom pullback. The p-values of a t-test indicate insignificant difference.

| | Stationary | Pullback | t-test |
|---|---|---|---|
| | $\mu_t \pm \sigma$ | $\mu_t \pm \sigma$ | *p-value* |
| Calcium | 3.56±0.13 | 3.64±0.35 | 0.64 |
| Lipid | 9.9±0.18 | 9.97±0.18 | 0.53 |
| Fibrous | 1.94±0.23 | 2.17±0.50 | 0.76 |

Table 5: Estimates on a clinical dataset of 311 VOI's from 35 pullbacks. Values compared are the average values of the attenuation coefficient.

| | Estimated values | | |
|---|---|---|---|
| | $\mu_t \pm \sigma$ | $\langle I \rangle$ | $I_o$ |
| Calcium | 3.58±1.74 | 37.81 | 38.46 |
| Lipid | 9.93±2.44 | 82.79 | 139.39 |
| Fibrous | 1.96±1.11 | 162.23 | 195.83 |

We plotted a feature space of optical properties ($\mu_t$, $I_0$, $\langle I \rangle$) obtained by running our proposed processing pipeline on a set of 311 VOIs from 35 clinical pullbacks (Figure 16). In the feature space plot, we observe good separation of the three plaque types identified with the three colors. In order to quantify this visual separation we trained and

tested an SVM classifier as described in Methods. We ran 5-fold cross validation on the 311 VOIs and calculated the accuracy measures as described in Methods. These results are shown in Table 6, showing that the $F_1$-Score is very close to 1 for all plaque types. This indicates that VOI-based classification is very close to perfect, indicating that our approach for volume classification will achieve very accurate results. These results are very promising given that current published results (i.e. [103, 125]) based on more than the above 3 features is well below 90%.

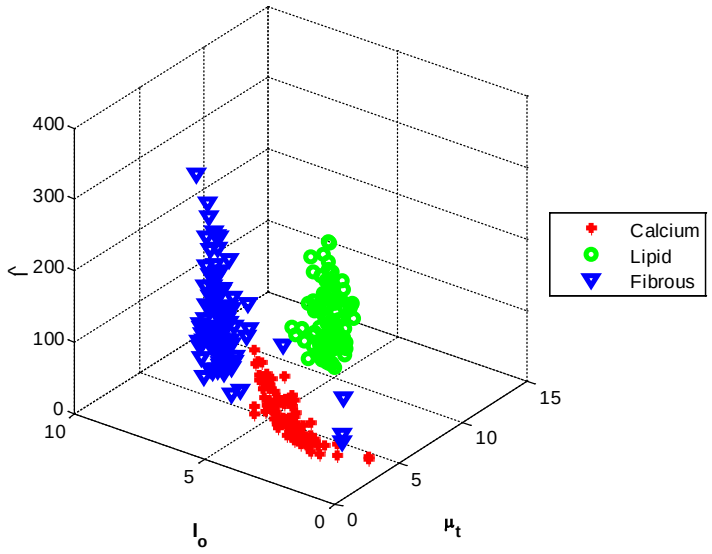


Figure 16: Feature space of ($\mu_t$, $\bar{I}$, $I_0$) created by applying the proposed LSQM method on 311 VOI's of all atherosclerotic tissue types after pre-processing pipeline. VOI's were derived from 35 clinical IVOCT pullbacks. We observe a good separation of plaque types even though only the three features ($\mu t$, $\bar{I}$, $I_0$) were used.

Table 6: SVM classification results: The overall classification accuracy was 92.5%, however, since we could not ensure that the data is not skewed, the $F_1$ score is also given ($F_1$ score = 2PR/(P+R)).

| | Precision (P) | Recall (R) | $F_1$-Score |
|---|---|---|---|
| Calcium | 94.3% | 86.8% | 0.904 |
| Lipid | 89.3% | 96.2% | 0.926 |
| Fibrous | 93.3% | 96.6% | 0.949 |

## 3.5 Discussion

We have created a computational pipeline for estimating optical parameters from 3D IVOCT pullback data and first evaluated it on realistic OCT vascular phantoms [104] . Because the phantom is locally homogeneous, it presents a unique opportunity for testing consistency of IVOCT measurements. We obtained $\mu_t$ estimates ($3.58\pm1.74 mm^{-1}$, $9.93\pm2.44 mm^{-1}$, $1.96\pm1.11 mm^{-1}$ for calcium, lipid, and fibrous respectively), which were within the ranges specified for the phantom. We carefully compared our pullback analysis method to a more conventional stationary analysis where the catheter was not moving along the length of an artery. Means were insignificantly different for all three phantom types, indicating no bias of measurements, even though in a pullback data comes from a catheter rapidly spiraling along the vessel at a linear rate of 20 mm/sec. To assess precision, we compared data spread, as measured by standard deviation, of measurements over at least 600 (5 stationary acquisitions for each type) samples for each plaque type. Pullback data had only slightly higher standard deviations for calcium and fibrous the same for lipid (Figure 15). The barely statistically significant (Table 4) differences might have been due to mechanical instabilities between A-lines. Finally, we also determined that the angle of incidence insignificantly affected $\mu_t$ estimates. This reassures us that the pullback does not introduce an additional confound even though each angle of incidence will be somewhat different for each A-line under consideration in the pullback. Similarly, when we analyzed volumes of interest at different depths in tissue, we found no significant difference in $\mu_t$ estimates for calcium and fibrous. (There was insufficient depth of signal to do this in the case of lipid.). Results of calcium and fibrous are consistent with good single exponential fits (Figure 16). Together, these

experiments suggest that our clinically practical, 3D pullback method yields accurate, precise results, as good as stationary analysis.

Analyses on clinical pullback data were equally encouraging. When comparing phantom pullback estimates to clinical pullback results, (Table 5) we observed that estimates were consistent with phantoms, but with a larger spread. Another thing to note is that the calcified and lipid plaques (in both, clinical and phantom) exhibited a much lower average intensity (signal poor regions) than that of the fibrous; however, the high attenuation of the lipid and the low attenuation of the calcium helped us to distinguish between the two easily. The high value of the average intensity of the fibrous indicates that it is signal rich region. The classification metric shows that the $F_1$ score approaches 1 as desirable for an accurate and efficient classification method.

The pipeline has some novel aspects which can be compared to previous reports in the literature. It was applied to clinical 3-dimensional (3D) data, which is aimed at improving the robustness of optical parameter estimation. In this study, we better account for noise in the acquired images. We also note that each 3D VOI consists of 50-400 A-lines with different angles of rotation ($\theta$) and different axial positions along the artery, posing many challenges including eccentricity of the catheter relative to the lumen surface, catheter motion, etc. We meet these challenges by applying the processing pipeline steps including pixel shifting, noise reduction, lumen segmentation using dynamic programming as described in [119], and better statistics for robust and resource-efficient estimation. Furthermore, our method of analyzing the results of phantom stationary acquisition, phantom pullback and clinical pullback is a good framework

enabling efficiency of processing and classification. Our results have indicated an improved feature space clustering that will aid in automated learning.

In conclusion, the proposed computational pipeline appears to work as well as a more standard “stationary” approach. This is important as it will be difficult to justify stationary acquisitions for routine clinical work. We believe that when optical parameters are combined with other features, it would further improve these results.

# Chapter 4 Machine Learning Plaque Classification from Intravascular OCT Image Pullbacks

## 4.1 Introduction

Heart attack is a major cause of death worldwide. Almost twice as many people die from cardiovascular disease than from all forms of cancer combined [126]. The underlying disease process in the blood vessels that results in coronary heart disease (heart attack) and cerebrovascular disease (stroke) is known as *atherosclerosis.*

There are various methods for imaging coronary artery disease where X-ray coronary angiography and intravascular ultrasound (IVUS) represent the most commonly used. Invasive angiography uses contrast agent to image the lumen by providing projection X-ray images of contrast-filled coronary vessels. While it provides detailed images of vessel lumen, it offers no information about the coronary wall. IVUS, on the other hand, provides microscopic images of the vessel wall, however, the resolution of IVUS is on the order of 100μm and it has the limitation of not being able to "see" through calcium plaque (sound waves do not penetrate the calcium plaque). Further, due to its limited resolution, IVUS cannot quantify the thickness of a thin fibrous cap in an inflamed thin-capped fibroatheroma (TCFA), which according to [127], is responsible for most acute coronary events.

Intravascular optical coherence tomography (IVOCT) is an emerging technology showing great promise for studying pathobiology of coronary artery lesions as well as for clinical diagnosis and treatment planning. *In-vivo* IVOCT generates high speed, high contrast, low noise, micron-scale resolution images with the capability of imaging plaque

components. It has been shown that IVOCT is able to distinguish between key types of plaque [32] [89], and aid in assessment of new coronary artery stent designs [83]. As compared to IVUS, IVOCT has low noise, better discrimination of lumen boundary, better resolution, and better delineation of plaque boundaries [71]. IVOCT has the resolution and contrast necessary to identify the thickness of a thin fibrous cap in a TCFA (*a cap* thickness <65 μm has been associated with risk of rupture in necropsy studies [7]). In addition to potential live-time clinical application of IVOCT for intervention planning, IVOCT can be used offline in pathobiology and drug treatment studies [29, 128-130]. The University Hospitals of Cleveland core lab, hereafter called Core Lab, is engaged in such studies and has manually analyzed over 2,500 IVOCT studies to date.

IVOCT generates a tremendous amount of image data, suggesting a need for automated analysis and improved 3D visualization. To acquire image data on one commercial IVOCT imaging system (C7-XR system from St. Jude using Dragonfly Due catheter) a catheter is pulled back along the artery acquiring over 540 image frames. This large amount of data can overwhelm manual analysis, especially in the case of live-time intervention. In addition, when analysts in the Core Lab have characterized plaque in 2D image sectors, they have found the task difficult and quite tedious, giving rise to variability and reduced accuracy [131]. Our goal is automated plaque characterization and 3D visualization allowing one to quickly review an entire pullback.

Several reports have shown that IVOCT can be used to evaluate plaque types. Tearney et al. [132] has shown that different atherosclerotic plaque types may be distinguished by analyzing temporal and spatial speckle pattern fluctuations. Van der Meer et al. [28] demonstrated the principle that quantitative analysis of the IVOCT signal

allows the determination of the attenuation coefficient (they used 800 nm IVOCT light) in a layered phantom as well as in layered arterial tissues. Xu et al. [102] relied on the analysis of the reflected light and attempted to correlate the backscatter and attenuation coefficients with various plaque formations. They focused on the separate processing of each A-line and did not include 3D data into their calculations. Ughi et al. [125] used μt estimates from a layer model applied to single A-lines and 2D texture and geometric measures as features for classification with the added requirement of manual ROI selection for analysis. In order to reduce speckle noise, Ughi et al. used low pass Gaussian filter, thus introducing under estimation of μt values as discussed in [133]. A more recent report was proposed by Lambros et al. [103]. Lambros et al. used 2D texture and intensity features alone and assumed "islands" of calcified tissue surrounded by other tissue types, which is not necessarily true in many image frames [71]. Another approach is proposed by Wang et al. [134]. In this approach the problem is broken into two parts: Starting and ending frames of the image stack containing calcified plaque are manually preselected as the input to the algorithm and segmentation within that range. In the segmentation step Wang et al. adopted a level set method to find the calcified region's borders. Then, this is followed by post analysis where false positive are manually corrected by the user. More recently, Roy et al. [135] report good results on accessing vulnerable plaque areas which is quantified by modeling energy tissue interaction and extracting 4 features within a variable sized 2D neighborhood kernel combined with attenuation coefficient to model the speckle statistics, and signal confidence maps.

In this chapter, we propose an algorithm for an automated characterization of three main plaque components: fibrotic, calcified and lipid-rich tissue. Our goal is to

create an *automatic* (no user interaction) procedure for plaque classification. Our algorithm can be used to quantify parameters of interest (such as calcified region's coverage and thickness) and its output will facilitate the ability to visually identify the morphology of atherosclerotic plaque. Our access to a database of over 2500 clinical IVOCT pullbacks from our partners at the Core Lab gives us a unique opportunity to test and validate our algorithm. Qualitative characteristics of atherosclerotic plaques described by former studies [32, 71] are quantified by employing both the physics of IVOCT image formation and image analysis to compute features from 3D regions within the IVOCT pullback volume.

In a previous report by our group [136] it is shown that optical properties can be used as reliable features discriminating the three main plaque types. We base our approach on machine learning methods where all of the extracted features are combined in a supervised classification algorithm resulting in a fully automated characterization of atherosclerotic plaque. The classification algorithm is trained by a set of data from 35 pullbacks with a range of plaque morphology, manually annotated by an expert. The performance of the algorithm is subsequently evaluated against an independent testing set extracted from IVOCT pullbacks annotated against cryo-images (gold standard), thereby ensuring very accurate annotation. Measured optical properties are compared to previous results reported in literature.

## 4.2 Algorithms

We created algorithms for voxel-based classification of IVOCT image data. Steps are pre-processing, moving box processing for feature extraction at each voxel, and supervised machine learning classification.

### *4.2.1 Preprocessing*

We perform various preprocessing steps, starting with IVOCT A-lines in ($r$,$\theta$) images. The first step is noise reduction using enhanced Lee filter optimized for speckle noise, as we have described previously [108]. This is followed by baseline intensity subtraction, and optical imaging system correction, as described previously [133, 136]. We use a modified version of our previously described dynamic programming approach [88] to accurately segment the lumen and the back-borders of the tissue signal (The back border is the depth in tissue where one obtains IVOCT image data higher than background noise)[133]. Next, we pixel shift A-lines along $r$ to correct for catheter eccentricity with respect to the vessel wall, making a vertical lumen border. Since the guide wire shadow obscures the view of the vessel wall, we exclude this region using a dynamic programming solution previously described [119]. Accounting for the lumen border, back border, and guide wire shadow, we create a mask for processing. Following these steps, natural logarithms are taken, linearizing the exponential attenuation of the IVOCT signal, $I_d(r) = I_0 \exp(-\mu_t r)$ to be:

$$\ln(I_d(r)) = \ln(I_0) - \mu_t r \tag{4.1}$$

where $r$ is the distance from the catheter lens, $I_d$ is the detected signal, $I_o$ is the incident intensity of the beam, and $\mu_t$ is the attenuation coefficient of the beam (both are the optical properties described below).

### *4.2.2 Moving Box (mBox) Processing*

We compute features for each voxel within the blood vessel mask by processing within a local 3D neighborhood referred to as a moving box, or *mBox*. Calculation at each *mBox* location provides a vector of features, which gives a point in feature space. The $mBox(i,j,k)$ is defined as a 3D volume of interest centered at $(i,j,k)$ in the $(r,\theta,z)$ view. We varied the dimensions of *mBox*, but settled on (11,7,3). Optionally, one can reduce processing time by skipping voxels, called the stride of the *mBox* in our implementation. The scanning range of *mBox* is determined by the 3D vessel mask and processing begins and ends when *mBox* fits just inside the mask. To save processing time, some processing steps such as filtering and co-occurrence matrix computations (see below) are done on the entire image, prior to running *mBox*.

### *4.2.3 Feature Extraction*

We calculate various local features within *mBox*. Some features are crafted to assess criteria described in a consensus document for manual assessment [89]. Those criteria are:

**Fibrous plaque:** "A fibrous plaque has high backscattering and a relatively homogeneous IVOCT signal." High backscattering is captured by a high average intensity. A homogeneous signal is indicative of low attenuation (a low value of $\mu_t$).

**Lipid plaque:** "… a signal-poor region within an atherosclerotic plaque, with poorly delineated borders, a fast IVOCT signal drop-off, and little or no OCT signal

backscattering, within a lesion that is covered by a fibrous cap." We capture these properties with texture, signal attenuation, geometric, and intensity features.

**Calcified plaque:** "appears as a signal-poor or heterogeneous region with a sharply delineated border (leading, trailing, and/or lateral edges)." Calcium is darker than fibrous plaque with greater variation in intensity level inside the region. Also, sharp borders characterize this region. These attributes are collected by our feature set.

We determine real-valued features using a base of support the size of *mBox*. Features include:

**Attenuation coefficient, $\mu_t$** – We fit logarithmically transformed data in Eq. (4.1), within an *mBox*, and we perform a least squares fit on each A-line segment to estimate $\mu_t$ and $I_0$. To get a robust estimate of $\mu_t$, we take the median across all values within the *mBox*, We previously showed that this method gave good estimates on pullbacks even in the presence of IVOCT noise [133].

**Reflected intensity, $I_0$** – We use $I_0$ from the A-line segment fit corresponding to the median $\mu_t$ reported above.

**Distance to lumen, $D_l$** – This is the distance from the voxel of interest along the A-line to the segmented lumen border. $D_l$ helps distinguish lipid because the average intensity rapidly falls off in lipid.

**Beam penetration depth, $D_d$** – This is the distance over which the beam penetrates the tissue. It is the distance from the front border to the back-border and is a characteristic of the whole A-line.

**Beam incident angle, $\theta_i$ –** This is the angle between the A-line and the normal to the tangent of the front border in the *(r, θ)* view. When the optical beam is not at a 90° angle with respect to the artery wall, light can be reflected away affecting intensities along the A-line.

**Mean Intensity,** $\bar{I}$ – This is the average signal intensity within the *mBox*.

In addition to the above optical features, we use several commonly used intensity variation features [137].

**Homogeneity, *H*** – This is a local coefficient of variation, $(\sigma/\bar{I})$, where $\sigma$ represents the standard deviation of the intensity values within the *mBox*. This feature helps distinguish heterogeneous intensity regions and homogeneous intensity regions.

**Relative Smoothness of intensity, *S*** – Defined as: $S = 1-(1/(1+\sigma^2))$ following normalization of the maximum intensity to 1.0. It measures the relative smoothness of the intensity in the region. It is 0 for constant intensity regions and it approaches 1 for large deviations in intensity values ($\sigma^2$ is the variance of the intensity values within the mBox).

**Entropy, *E*** – We construct a histogram of intensities within an *mBox*, normalize it to give probabilities of intensity, $p(z_i)$ where $z_i$ is the gray scale value after pre-processing. Then, entropy is computed from

$$E = -\sum_{i=0}^{L-1} p(z_i)\log_2 p(z_i)$$

where $p(z_i)$ is the probability of the intensity level, $z_i$, $i$=1,…,L for L bins in the histogram of intensity levels. Within homogeneous regions the entropy will be low and within heterogeneous regions it will be high.

We also include four spatial texture features by sampling the way certain grey-levels occur in relation to other grey-levels (co-occurrence matrix). Briefly, let *O* be an operator that defines the position of two pixels relative to each other and consider an image $I(r,\theta)$, with L possible intensity levels. Let G (co-occurrence matrix) be a matrix whose element $g_{ij}$ is the number of times that pixel pairs with raw intensities $z_i$ and $z_j$ occur in *I* at the position specified by *O*, where $1 \le i, j \le L$. The total number, *n*, of pixel pairs that satisfy *O* is equal to the sum of the elements of G. Then the quantity $p_{ij}=g_{ij}/n$ is an estimate of the probability that a pair of points satisfying *O* will have values ($z_i$, $z_j$) (see [138] for a detailed discussion of co-occurrence matrices). A normalized co-occurrence matrix is formed by dividing each of its terms by *n*.

Co-occurrence values have been used successfully in previous IVOCT plaque classification papers [139-141]. In our experiments, we use four out of the 22 possible [142] features that can be extracted from the co-occurrence matrix. The probability $p_{ij}$ is the ij-th element of G/*n*, $m_r$ is mean computed over the rows and $m_c$ is the mean computed over the columns of the *mBox*. K is the row (or column) dimension of G.

**Contrast, *C* –** Defined as:

$$C = \sum_{i=1}^{K} \sum_{j=1}^{K} (i-j)^2 p_{ij}$$

where *K* is the dimension of G. *C* measures the intensity contrast between a pixel and its neighbor over the *mBox* (C is zero for a constant *mBox*).

**Correlation, *Cor*** – Defined as:

$$Cor = \sum_{i=1}^{K} \sum_{j=1}^{K} \frac{(i-m_r)(j-m_c)p_{ij}}{\sigma_r \sigma_c}$$

It measures how correlated a pixel is to its neighbor in the *mBox* and its value is in the range -1 and 1. Here, $\sigma_r \neq 0$, is the standard deviation measured along the rows of the *mBox* and $\sigma_c \neq 0$ is the standard deviation measured along the columns. *Cor* is 1 or -1 for perfectly positively or negatively correlated *mBox* and not defined for constant *mBox (*since the denominator is zero).

**Energy, E** – is the sum of the squared elements in G with a range of [0 1] (the energy is 1 for a constant *mBox)*.

**Co-occurrence Homogeneity, *Hc*** – It is the value of the closeness of the distribution of elements in the G to the diagonal of G and is computed as:

$$H_c = \sum_{i=1}^{K} \sum_{j=1}^{K} \frac{p_{ij}}{1+|i-j|}$$

### *4.2.4 Classifier*

We use a Support Vector Machine (SVM) classifier. Each voxel gets a vector of features from the *mBox* calculations described above (each feature is normalized by subtracting its mean and divided by its standard deviation). SVM is widely used due to its high accuracy, ability to deal with high-dimensional data, and flexibility in modeling diverse sources of data [143, 144]. It is a maximum-margin linear classifier [145] that also has provably good generalization bounds [146]. Traditional SVM training is formulated in terms of a quadratic program (QP) which is typically optimized by a numerical solver. The SVM uses a linear discriminant function of the form: $f(x) = w^T + b$ where the vector *w* is the weight vector and *b* is the offset and *x* is the point in feature space. Its objective function trades off two quantities: the margin, which is the distance from the separating plan and

which is inversely proportional to $||w||$, and the loss arising from misclassifying training instances. Constraints in the quadratic program reflect the fact that the training data should be classified correctly. Therefore, the cost function optimized by the linear SVM is [91]:

$$\begin{aligned} &\arg\min_{w,\xi_i} \frac{1}{2}||w||^2 + C\sum_{i=1}^{N}\xi_i, \\ &\text{s.t.} \quad y_i(w^T x_i + b) \geq 1 - \xi_i, \\ &\xi_i \geq 0 \end{aligned} \tag{4.2}$$

where $C$ is a positive parameter that sets the relative importance of maximizing the margin and maximizing the amount of slack, $y_i$ is the true label, $x_i$ is the feature vector, and $\xi_i$ is the slack associated with training example $i$.

Decision boundaries that are nonlinear in $x$ can be constructed through the use of a nonlinear feature map, $\varphi(x)$. When the quadratic program above is rewritten with $\varphi(x)$ and converted into dual form, the solution appears in the form of the dot product, $\varphi(x)\varphi(y)$, which is defined to be the *kernel* function, $k(x,y)$. The kernel matrix can be constructed efficiently even when the feature maps $\varphi(x)$ are very complex or even infinite-dimensional. This is known as the "kernel trick" and allows the SVM to efficiently produce classifiers that are high dimensional and nonlinear with respect to the original data.

Various kernel functions are possible. In our work, we use *Radial Basis Function* (RBF) kernels, which are a common choice because of their expressiveness. The RBF is defined as:

$$k(x_i, x_j, \gamma) = \exp\left(\frac{\| x_i - x_j \|}{2\gamma^2}\right) \tag{4.3}$$

where $x_i$ and $x_j$ are the feature vectors, $\gamma$ controls the width of the kernel (it controls how far the influence of a single training example reaches).

We use the one-versus-rest (OVR) approach for multi-class classification, giving a binary classifier for each class. Because we are interested in three plaque types, we created three OVR classifiers (OVR-C, OVR-L, OVR-F for calcium lipid and fibrous respectively). An advantage of the OVR approach is interpretability. Since each class is represented by only one classifier, it is possible to gain knowledge about the class by inspecting its corresponding classifier.

Because the majority of voxels did not belong to one of the main three plaque types, we experiment with two approaches for classifying these voxels as "other" plaque type. First, we considered another class, "other" and created a fourth OVR classifier, OVR-O. Second, since many voxels do not clearly belong to any of the three classes, we introduce the "other" class. We developed a threshold logic (OVR-P) on the OVR models that appropriately left many voxels in the "other" class without having a trained model for it (Algorithm 1). The idea behind this prediction rule is to classify any given voxel as one of the main plaque types only if we are highly confident that it belongs to that plaque type, otherwise, classify it as "other". One of the key things to identify in this algorithm is the need to determine the probability threshold, $p_{thresh}$ which defines what "absolutely sure" means and is described in the next section. The complete multi-class plaque classifier, which combines all binary classifiers (OVR-C, OVR-L, OVR-F, and OVR-P) is referred to as MCC.

```
1:   Init:
2:     1. Use training set to train a binary SVM to get the
3:          three models, OVR-j,            j='C', 'L', 'F'
4:     2. m_j = Compute the margins of each model.
5:   For each unknown point, x_i {    i = 1…(num of points)
6:     1. [c_j, p_j] = Predict using OVR-j,   c_j∈(0,1); p_j ∈(0-1);
7:     2. if <all c_j = 0>
8:              x_i = "other"
9:          elseif <more than one c is 1>
10:             x_i = plaque type of the larger m_j.
11:         elseif <only a single c_j =1>
12:             if p_j>p_thresh,j
13:                x_i = j
14:             else
15:                x_i = "other"
     }
```

Algorithm 1: OVR-P prediction rule of "other" plaque type. $c_j$ is the binary class assignment (0,1) where 1 means that the point is assigned the class of the classifier and 0 means it's not. $p_j$ is the probability of the assignment. $P_{thresh,j}$ is the probability threshold of the plaque j (j='C', 'L', 'F') determined as described in the text.

The probability threshold, $p_{thresh}$, is the decision threshold (cut-off value) used to define positive or negative outcome as described on the ROC curve. Thresholds were determined using two common approaches for choosing an optimal operating point [147]. First, the minimal square distance, MSD, computes the square of distance from any point on the ROC to the theoretically optimum point, (0, 1), the upper left hand corner of the ROC space. The distance squared, $d^2$, is given by

$$d^2 = (1\text{-}TPR)^2 + FPR^2 = (1\text{-} Sn)^2 + (1\text{-}Sp)^2$$

where TPR is the true positive rate, or sensitivity (Sn), and FPR is the false positive rate, or (1 – specificity(Sp)). The squared distance is tested at all points along the ROC and the minimum distance is chosen as the operating point for our threshold. We call this optimum point MSD-OP. Second, we use the Youden index [148] to determine an operating point, the Youden-OP. The Youden index is the vertical distance between an ROC data point and the point (x, y) on the diagonal, chance line). This leads to the definition of the index as J = sensitivity + specificity - 1 = TPR - FPR. To choose the

operating point, Youden-OP, we maximize J above. It should be noted that by maximizing J, we, in fact, maximize the difference between TPR and FPR and by doing so we maximize (Sn + Sp) across various cut-off points. The Youden index's value may range from 0 up to 1, and has a zero value on the chance line. A value of 1 indicates that there are no false positives or false negatives, i.e. the test is perfect. The index gives equal weight to false positive and false negative values, so all tests with the same value of the index give the same proportion of total misclassified results. The operating point used in the Youden approach is named Youden-OP.

There are two SVM parameters: C, the regularization parameter that trades off margin size and training error, and $\gamma$, the Radial Basis Function (RBF) Gaussian kernel's bandwidth. These parameters were optimized as described below.

## 4.3 Experimental Methods

### *4.3.1 IVOCT Image Acquisition and VOI Selection*

Images were collected on the C7-XR system from St. Jude Medical Inc., Westford, MA. It has an OCT Swept Source having a 1310nm center wavelength, 110nm wavelength range, 50 kHz sweep rate, 20 mW output power, and ~12mm coherence length. The pullback speed was 20 mm/s and the pullback length was 54 mm. A typical pullback consisted of 271 image frames spaced ~200 $\mu m$ apart. Images used in this study were selected from the database available at the Cardiovascular Core Lab of University Hospitals Case Medical Center (Cleveland OH). They consisted of 35 IVOCT pullbacks of the Left Anterior Descending (LAD) and the Left Circumflex (LCX) coronary arteries of patients acquired prior to stent implantation.

### *4.3.2 Clinical Training Dataset*

The training dataset was created from de-identified clinical images in the Core Lab acquired for other purposes. An expert reviewed pullbacks and identified homogenous volumes of interest (VOIs) for each plaque type (fibrous, lipid, or calcified) utilizing consensus criteria descried earlier. VOIs were marked with freehand brush strokes on images in the $(r,\theta)$ view. We used over 300 VOIs from 35 pullbacks. VOIs were of various sizes and shapes. Most consisted of 2-5 image frames, 50-200 A-lines, and 20-50 sample points in each A-line.

### *4.3.3 Independent Validation Dataset*

For validation testing, we created an independent (not used in training) image dataset with each voxel accurately labeled and validated by 3D cryo-imaging. To create this dataset, we obtained coronary arteries (LADs) of human cadavers within 72 hours of death and stored at 4 °C. Arteries were treated and stored in accordance with federal, state, and local laws by the Case Institutional Review Board. To prepare for IVOCT imaging, arteries were trimmed to approximately 10 cm in length. A luer was then sutured to the proximal end of each vessel which was flushed with saline to remove blood from the lumen. Major side branches and the distal end of each artery were sutured shut. Using super glue, the artery was adhered to the sides and bottom of a rig that was used to minimize motion between cryo and IVOCT imaging procedures. IVOCT imaging conditions mimicked the *in-vivo* acquisitions described above. Sutures were placed on the vessel to identify ROIs (1.5–2cm in length) that would later be analyzed using cryo-imaging. Following IVOCT imaging, the entire imaging rig containing the artery was

flash frozen in liquid nitrogen, and stored at -80 °C until cryo-imaging was performed. Prior to cryo-imaging, arteries were cut into blocks corresponding to the ROIs determined during IVOCT imaging. Blocks were placed in the cryo-imaging system and allowed to equilibrate to the -20 °C cutting temperature. The ROIs were then alternately sectioned and imaged at 20 μm cutting intervals, and color and fluorescent cryo-images were acquired at each slice. The process was repeated until the whole specimen was imaged.

Cryo-imaging [149] is a novel validation tool that fills the gap between 3D IVOCT pullbacks and 2D histology. Briefly, the system consists of a modified cryo-microtome with an integrated microscopic imaging system. The system serially sections and acquires micron-scale episcopic color and auto-fluorescence microscopy images along the vessel. Visualization software is then used on the cryo-images to generate microscopic resolution color/fluorescence volume renderings of vessels, in which plaque architecture and components are fully preserved [149]. This provides an accurate depiction of the vessel without the limitations of standard histological fixation and processing (shrinkage, spatial distortion, missing calcifications, missing lipid pools, tears, etc.). Most importantly, this provides 3D validation for volumetric IVOCT pullback. Furthermore, in cases where plaque type may be ambiguous, the system enables acquisition of standard cryo-histology.

We created an accurately labeled, independent data set for validation. An expert annotated every pixel in IVOCT images using registered cryo-images as a gold standard guide. This manual method provided accurate labeling even if there were small registration errors between cryo- and IVOCT image volumes. To simulate the clinical

application, *ex-vivo* IVOCT images were acquired with different catheters and with different eccentricities with respect to the vessel wall. A range of plaque morphologies were included.

### *4.3.4 Optimization and Evaluation of the Plaque Classifier*

To find the best Radial Basis Function's parameters (C and $\gamma$), we implemented grid search using 5-fold stratified cross validation on the approximately 11,000 data points (roughly 33% for each plaque type) extracted from the clinical training dataset described above. That is, we trained the classifier on 80% of randomly selected voxels using a pair (C, $\gamma$), and we tested the performance on the held-out 20%. The goal was to identify parameters that maximized performance on the held out set. Different pairs (C, $\gamma$) were evaluated in a grid search using exponential sequences of C and $\gamma$, i.e., $C = 2^{-5}, 2^{-3}, \ldots, 2^{15}$, $\gamma = 2^{-15}, 2^{-13}, \ldots, 2^{3}$, as suggested previously [150]. Optimum values (C = 8.5742 and $\gamma$ = 0.1015) were used in subsequent experiments.

In addition, we performed an experiment to verify that the amount of training data was appropriate using a "learning curve" analysis [90]. Briefly, we split the clinical training dataset into two parts: 20% which was used as a test set, $D_{test}$, and 80%, $D_{train}$, from which random examples were drawn. We selected *n* samples (*n*=1,2,3,…,size($D_{train}$)) from $D_{train}$, and perform on it a 5-fold cross validation getting a model (in each fold, the model with the highest performance accuracy measure is chosen). Then, the model's performance is tested on the same *n* samples, yielding the training error, $J_t$ and on $D_{test}$, yielding the testing error, $J_{test}$. Normally, as one increases *n*, $J_{train}$ and $J_{test}$ should asymtote. We used stratified 5-fold cross validation when randomly dividing up the examples into

training and cross validation in each fold. *Stratified* 5-fold cross validation means that each fold contained roughly the same proportions of the class labels.

We assessed classifier performance by generating a Receiver Operating Characteristic curves (ROC) for each OVR classifier using a stratified 5-fold cross validation experiment on the clinical training dataset. By plotting the ROC curve for each of the classifiers, we can calculate the threshold level of the probability. In addition, we computed the area under ROC curves, AUCs, giving us a summary statistics for each of the classifiers. To furthermore assess generalizability, we performed a *leave-one-pullback-out* (LOPO) experiment, for each of 35 different pullbacks. The training set was the 34 other pullbacks. Previously, we have argued that this is a more stringent, realistic test as opposed to random partitions [83]. We computed the quality of classification using standard metrics. That is, we used TP (true positive), FN (false negative), etc. and we computed specificity, SPC = TN/(FP+TN), and sensitivity (percentage of correctly classified pixels of all of the true, manually annotated pixels) with SEN=TP/(TP+FN). Values were averaged across the *n* test cases (where we computed *n*-fold cross validation). The values presented are computed using the MSD-OP as discussed above.

Having assessed the performance of the MCC as described above, we then trained the MCC on *all* of the clinical training data and tested it on the independent validation data set. We compared automated results against the gold standard, labeled images with cryo-image backup on a voxel-by-voxel basis.

### *4.3.5 Post Processing*

Since voxel-wise classification is noisy and because clinical application does not require voxel resolution, we performed multi-class noise “cleaning.” We performed post-

classification smoothing on the binary images resulted from each of the OVR classifiers using the size-based filter proposed by Jensen et al. [151]. In this approach, each region that has an area less than a user-defined threshold, is defined as noise. If a noise region has the same classification as background, it is called “interior noise”, and otherwise, it is “exterior noise”. Interior noise voxels are relabeled as foreground (i.e. as the label of the majority of its neighbors). Exterior noise voxels are relabeled background (“other”).

## 4.4 Results

The IVOCT generates cross-sectional images of the lumen, plaque, and vessel wall (Figure 17). As described in the legend, images express the qualitative plaque criteria for calcium, lipid and fiber, described previously.

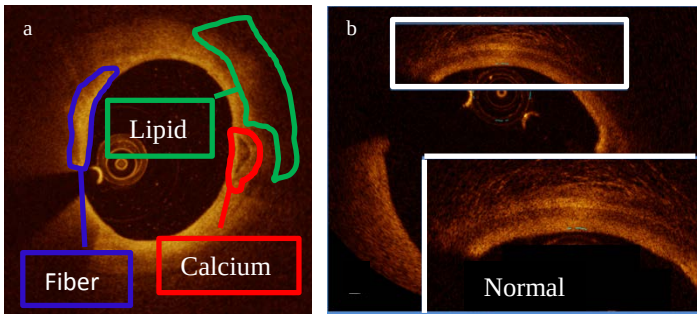


Figure 17: Appearance of atherosclerotic tissue types in clinical images. (a) fibrous (high backscattering and a relatively homogeneous), lipid (signal-poor region with poorly delineated borders, a fast IVOCT signal drop-off, and little or no signal backscattering) and calcium (signal-poor or heterogeneous region with a sharply delineated border) are identified. (b) Normal blood vessel wall showing layered structure. The latter includes a zoomed inset to show the typical layered appearance.

We evaluated the two approaches for classification: 4 OVR classifiers, including OVR-O and MCC. The challenge was that “other” voxels have a very wide range of attributes. When we trained the first method on VOIs and applied it to the independent data set, there were many classification errors and accuracy of the “other” plaque type

was degraded to the range of 50% (not shown). This is probably due to the wide range of attributes of “other” voxels. In general, the second approach, using MCC, worked much better, as detailed below.

### *4.4.1 Training and Model Creation on Clinical Data Set*

The learning curve analysis provides insight of the bias/variance of our plaque classifier. We computed the overall training/test error using the MCC where the error is the overall error rather than of a specific OVR classifier. As shown in Figure 18 the test error (blue line) starts quite high but decreases rapidly and approaches the training error (orange line) as the number of samples increases. The curves plateau around 10,000 samples. We use approximately 11,500 samples which should be sufficient for ensuring optimal performance. The horizontal dotted green line in the figure provides an important observation: It signifies the size of the classification error achievable with the current features set. It indicates the level of bias of the classifier, which means that to achieve a lower error, additional features (as opposed to additional examples) might help.

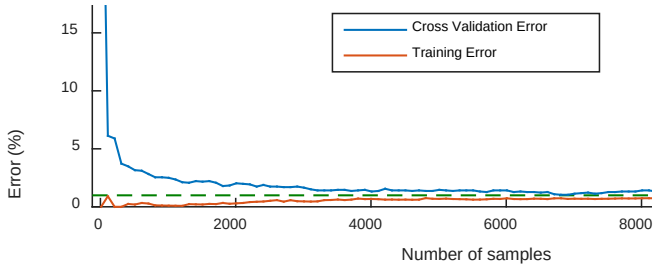


Figure 18: Learning curve analysis. Blue curve represents the test error rate, $J_{test}$ (see text) and the orange curve represents the training error, $J_{train}$. The minimal number of samples should be at the asymptote, giving about 10,000. In experiments, we safely used 11,500 samples. The cross validation error is averaged across the 5 folds. The steady state error (~4%) at the blue arrows corresponds to the classification error where further improvement can be achived by adding more features but not by adding more samples. The horizontal line corresponds to the steady state error magnitude.

| | Calcium | lipid | fibrous |
|---|---|---|---|
| | Using Youden-OP | | |
| Sensitivity | 83.8±4.9% | 94.6±1.7% | 94.5±3.3% |
| Specificity | 94.6±1.4% | 89.3±2.7% | 89.0±2.5% |
| | Using MSD-OP | | |
| Sensitivity | 87.6±4.1% | 93.6±1.9% | 94.5±7.4% |
| Specificity | 94.1±1.8% | 91.1±2.9% | 90.5±4.5% |
| AUC | 0.97 | 0.99 | 0.99 |

Table 7: Statistics at the operating points of the ROC curve

ROC curves with operating points thresholds are shown in Figure 18 and summary statistics are given in Table 7 for a 5-fold cross validation. For the three principal OVR classifiers (OVR-C, OVR-L, OVR-F), AUCs all exceed 0.95. All operating point thresholds values are above 50% as indicated, however, values depend upon plaque type. The two methods tended to give similar probability thresholds, with only a 5% absolute probability variation between methods. At the operating points, mean sensitivities and specificities are unequal but all exceed 0.9. Comparing total error multi-class classification with the clinical training data, we get error variation of about 2.7% and 3.7% for methods MSD and Youden, respectively. In subsequent analyses, we use the MSD to obtain operating points, unless otherwise noted.

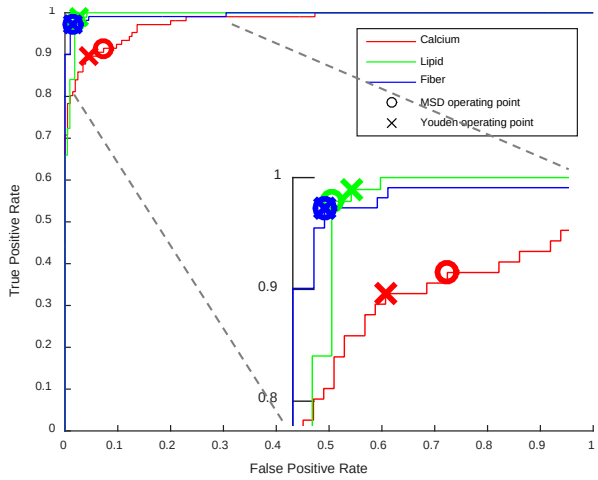


Figure 19: ROC curves for each OVR. 11,500 manually annoated samples were used. The inset is a zoomed area showing the operating points of both methods, MSD and Youden used with OVR-P classification. Probability values at the operating points are: MSD-OP=52.1%, 67.0%, and 57.6%. Youden-OP=58.8%, 63.8%, and 57.6% for calcium, lipid, and fibrous, respectively.

In Figure 20 and Table 8, we give the sensitivity and specificity of the two validation paradigms, 5-fold cross validation and the LOPO. We obtained excellent performance for all plaque types. In fact, in the LOPO experiment we can see that in most cases the classifier is able to discriminate between the plaque types. One might expect that if a certain pullback does not contain, for example, calcium in a data set, there will be no TP or FN for that test, which may cause large variations for some folds across the 35. However, the fact that the results' variation did not increase significantly, indicates that in cases where the missing plaque type (calcium in our example) was claimed by a specific classifier, the confidence of the claim was lower than the $p_{thresh}$ of the MSD-OP and, thus, its ownership claim was modified to "other" by our OVR-P rule.

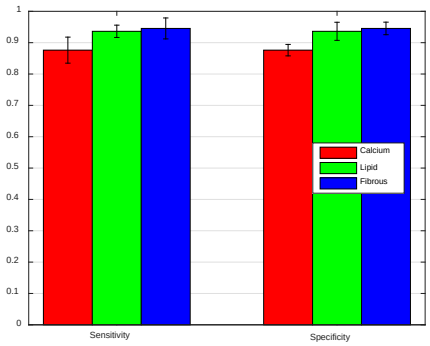


(a)

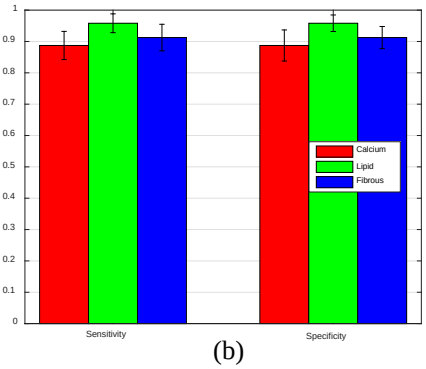


(b)

Figure 20:Training/testing statistics. (a) 5-fold cross validation sensitivity and specificity. (b) Sensitivity and specificity for leave-one-pullback out experiment. The two strategies gave comparable results, within the uncertainty of the assessment, suggesting generalizability. The uncertainty measure shown above is the standard error of the measurements.

| | LEAVE-ONE-PULLBACK-OUT | | |
|---|---|---|---|
| | CALCIUM | LIPID | FIBROUS |
| ACCURACY | 91.58±14.3% | 93.22±16.28% | 95.12±19.26% |
| SPECIFICITY | 89.83±18.85% | 95.05±18.03% | 91.73±10.52% |
| SENSITIVITY | 89.48±6.48% | 95.25±8.6% | 91.57±17.4% |
| | 5-FOLD CROSS VALIDATION | | |
| ACCURACY | 87.75±8.62% | 96.73±4.94% | 97.31±2.45% |
| SPECIFICITY | 87.02±2.74% | 92.66±4.34% | 92.94±4.34% |
| SENSITIVITY | 87.75±8.62% | 92.73±4.94% | 93.31±2.45% |

Table 8: Training/testing statistics from Figure 20.

Since voxel-wise classification is noisy and gives a higher resolution than desired clinically, we analyzed classification within entire VOIs. The preponderance of voxel classifications were correct. In Figure 21, we have plotted percentage of voxels attributed to each class and the corresponding ground truth label for the VOI. In all cases, most

voxels were labeled correctly. In fact, when applied plurality voting within each VOI, we got perfect, 100% accuracy for VOI classification.

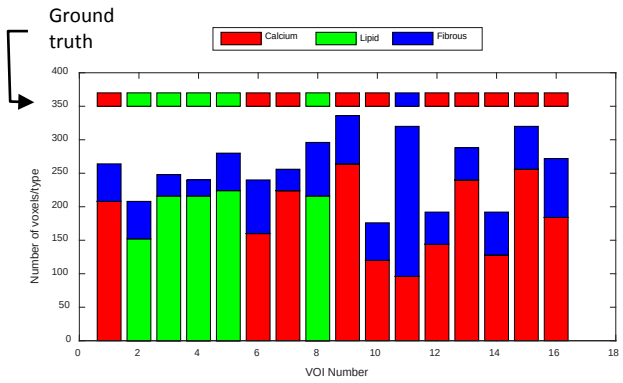


Figure 21: mBox plurality vote within a VOI. The preponderance of voxel classification leads to 100% accuracy in VOI classification.

### *4.4.2 Evaluation on Independent Validation Dataset*

We evaluated the MCC approach on the independent validation dataset confirmed with cryo-imaging. Example image results (Figure 22) show cryo and IVOCT input images, manual gold standard plaque annotations, and classifier results. Noise cleaning using size-based filter greatly improved results. For example, in the image shown on the top row of Figure 22 the overall accuracy of the MCC before cleaning was 87.3% and after cleaning it was improved to 89.7% (7879 voxels' labels were changed). Analysis showed that many of the misclassifications after noise cleaning occurred at the edge of regions, probably because features are obtained over a finite base of support leading to edge effects. Another possible reason is that the cleaning algorithm puts voxels of the same class into the same region only if they are neighbors, which may be a too strict condition. For example, pixels may occupy a big area without neighboring to one another, given they are interleaved. In such case size-based filter would regard all pixels as noise and remove the whole region.

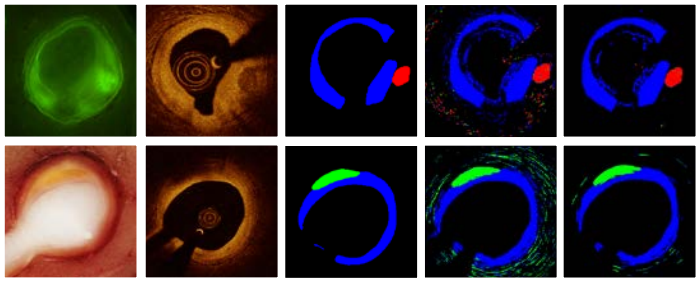

Figure 22: Example of validation analysis. Top row images (from left to right): cryoimage fluoresence, IVOCT, expert annotation of IVOCT guided by regisered cryo-image, results of automated classification, and automated classification after noise cleaning. In the bottom row, image data from a different vessel segment are shown with the exception that the fluoresence image is replaced by the color cryo-image. Calcium, fibrous, and lipid are labeled red, blue, and green respecitively, Note the good correspondence between the third and fifth columns indicating good classifications.

The confusion matrix in Figure 23shows voxel-wise multi-class plaque classification results. Tests are shown for ~4 million voxels following classifier noise cleaning. Large values along the main diagonal of the confusion matrix show that the predominance of voxels (87.1%) were correctly classified. The noise cleaning post-processing had a significant visual impact as shown in Figure 22. In addition, its impact was also evident in the classification results. Comparing the confusion table before noise cleaning (not shown) to the post-cleaning confusion table showed that the overall performance was improved by 3-4% indicating that the cleaning (or more accurately "re-classifying") scheme had positive impact on the overall accuracy and meaningful data is preserved. Furthermore, a few observations are important to note in the table: First, the main confusion between calcium and lipid is where a lipid is being classified as calcium, and vice versa. This points to the fact that adding a lipid-specific feature may reduce the errors further. In addition, the major confusion is shown to be in misclassifying "other". This, however, is inconsequential since "other" is of no interest (in this research). Finally, as shown in Figure 23, we note the overwhelming number of "other" plaque type. This

causes all of the plaques of interest to have relatively small numbers, thus causing the accuracy figure to be less effective (we keep it as a means of comparison throughout the study).

| | | Expert Annotation | | | |
|---|---|---|---|---|---|
| | | Calcium | Lipid | Fiber | Other |
| Predicted label | Calcium | 23,111 | 1,691 | 9,163 | 1,877 |
| | Lipid | 1,768 | 33,414 | 1,271 | 899 |
| | Fiber | 772 | 564 | 645,235 | 505 |
| | Other | 2,420 | 705 | 13,225 | 2,968,707 |

Figure 23: Confusion matrix from the independent validation data set after cleaning operation. Note that the majority of the misclassification occures for “other” plaque type as discussed in the text.

| | CALCIUM | LIPID | FIBROUS | OTHER |
|---|---|---|---|---|
| ACCURACY | 91.3% | 91.4% | 91.4% | 91.4% |
| SENSITIVITY | 82.3% | 91.9% | 96.5% | 90.5% |
| SPECIFICITY | 91.2% | 91.4% | 90.0% | 95.7% |

Table 9: Classification statistics from the independent validation data set (see Figure 23).

### *4.4.3 Visualization of Automatic Classification*

We created visualization methods for conveying plaque classifications in a clinical setting (Figure 24). Out of the multiple approaches available to show the results we found three to be most effective. We show majority plaque type vote (the color of the outer rim in Figure 24a) within a sector (red, green and blue indicate calcium, lipid and fibrous respectively). Second (Figure 24b), we display the automatic classification, allowing a better judgment on what the given sector contains. Finally, possibly more useful in the real time application, is a 3D view of the segment of interest (Figure 24c). This type of visualization may enable the physician to view a complete section, replacing the current need of going back and forth about a frame of interest in order to make a decision as to what is the plaque content within that frame. The 3D reconstruction was obtained using

Amira [152] by combining 65 2D frames into a volume of a 13mm long blood vessel segment which went through automatic classification.

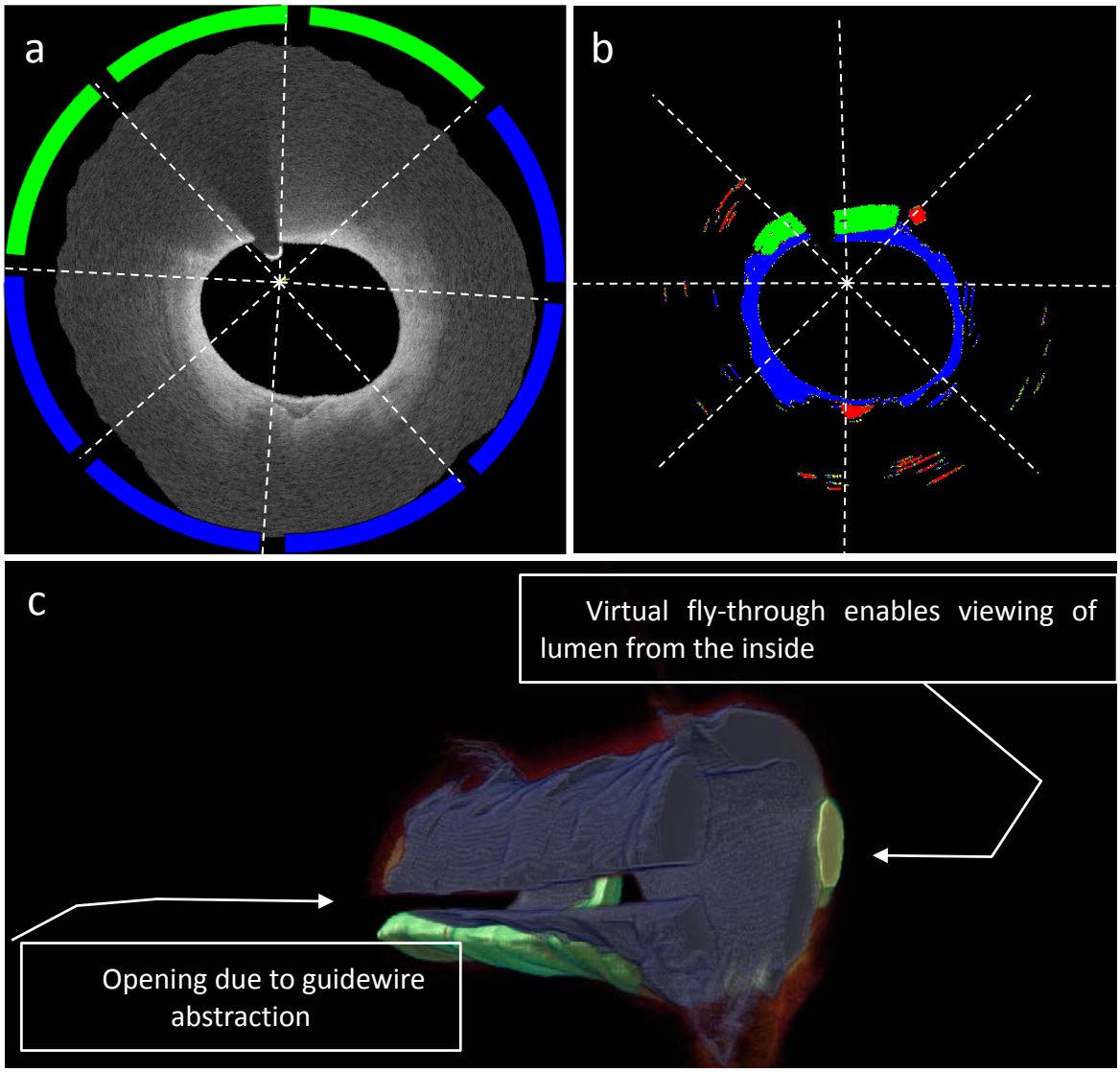


Figure 24: Visualizations describing necessary output for clinical use. Possible application of automatic classification. (a) A frame is masked and divided into sectors (in this example, 8 sectors) showing the plurality vote of the 3 main plaque types in an arc on the frame's edge. (b) The actual classification result is shown aiding to view the actual plaque distribution within the sector. (c) A more advanced 3D volumetric visualization showing a blood vessel segment with the plaque types as overlays. This visualization will be more appropriate in an on-line application where total coverage along a segment is important to see in order to make an informative decision of treatment (3D visualization implemented using Amira). This view also enables the physician to view the blood vessel segment from inside the lumen.

## 4.5 Discussions

Voxel-wise plaque characterization using physics, morphology, and 13 features performed well. Overall accuracy > 90% for all plaque types on the clinical training data were excellent, probably owing to the selectivity of this data. The independent, ex-vivo, cryo-image backed data provided a better test of performance. Voxel-wise accuracy was good (87.1%) but more importantly, regional characteristics were very well matched to a preponderance of classified voxels. Voxel-wise errors are probably due to classification noise and are rather unimportant. For clinical decision making, relatively large regions of calcium or lipid will be of interest, and even for research on therapy assessment, one will use more regional assessments. When machine labeled images following classification noise cleaning were compared to the annotated gold standard, there was very good visual agreement, allowing one to easily determine regional characteristics (Fig 5). When we analyzed clinical image homogeneous sub-volumes, we obtained a remarkable 100% accuracy with a plurality vote. Finally, when we did a sector comparison of machine labeling to annotation on the independent data set, we improved accuracy from ~85% (voxels) to 100% (sectors). Since results were quite promising, we created some visualizations which might be useful for real-time clinical and post-acquisition analysis for therapeutic assessment. We avoid macrophage imaging, mostly because it would probably not affect intervention planning (Our preliminary macrophage analysis method [88] could be used in a semi-automated fashion if required).

Importantly, we evaluated classification with independent data. Not only that, we actually had two different data sources for training and evaluation – expert determined sub-volumes from *in-vivo* datasets and *ex-vivo* IVOCT images labeled from registered

cryo-image data, respectively. Because labeled data were acquired in two different ways, it probably stress-tests classification much more than if we used a single type of labeled data source, probably suggesting that performance on the *ex-vivo* data gives a conservative evaluation of performance. In fact, when we did 5-fold cross validation on the in-vivo sub-volumes performance was much better, as expected.

We used a multi-class one-versus-all with rejection of many voxels, called “other.” We created OVR-C, OVR-L, OVR-F, and OVR-P used a threshold and when combined in a single scheme, are referred to as MCC. The MCC approach worked better than the 4 OVR class solution tested probably because modeling of plaques which do not conform to the expected pattern of the main three plaque types in features space is very challenging since these plaques are not well understood or characterized. Our MCC approach could be expanded upon.

There are mainly two alternatives in the literature [153] for arriving at different thresholds for each class allowing for different operating point probability threshold (AKA cut-off): One, where the specificity and the sensitivity are equally weighted (such as Youden and MSD) and the other puts different weights on the sensitivity and specificity. For the purpose of the current research, we decided to use the equal weight approach. One can introduce different costs to specific types of errors [154-156]. For example, we could add extra cost to misclassifications of lipid and calcium because if one were to perform atherectomy on lipid that could have disastrous effect. As more data is obtained, we will investigate such solutions.

The approach of one-versus-all with rejection (or as we referred to it, the MCC) is an improvement on the general approach in pattern recognition where the conditional

probabilities is computed and the most unreliable objects are rejected, that is, the objects that have the lowest class posterior probabilities (AKA “ambiguity reject” [157]). The improvement is expressed in two ways: First, we select a per-class-threshold, second, we select the probability threshold in a way which is relevant to the problem at hand (i.e. by allowing emphasis on sensitivity/specificity).

In any data analysis task, verification that the data available is comprehensive enough to draw general conclusions is very important. Furthermore, the size of the classification error achievable with the current features set is indicated by the green arrows in Figure 18 (which also indicates the level of bias of the classifier). To achieve a lower error, additional features (as opposed to additional examples) might help.

Features that describe the structures inherent in the data are as important as the quality and quantity of the data. One approach for feature extraction is to create as many features as possible (with less emphasis on their significance on the problem at hand) and let the classifier make the decision. The other approach, as done in this work, is to use domain expertise. We constructed features which were inspired by physics and qualitative features criteria as described by Yabushita et al. [32] and Tearney et al. [89]. These features were incorporated as *a priori* knowledge to create the most effective features to be used in the machine learning algorithm. There are three main reasons for the approach we took: First, better features means flexibility. One can choose “the wrong classifier model” (less than optimal) and still get good results. Most models can pick up on good structure in data. The flexibility of good features allow using less complex models that are faster to run, easier to understand and easier to maintain. Second, with “good” features, we are closer to the underlying problem and a representation of all the

data we have available and could use to best characterize that underlying problem. Finally, the most demanding task in classification is features extraction and design. Spending time on meaningless feature extraction is not the best use of our time.

Three experiments were used to test the quality of the MCC classification approach: 5-fold cross validation and LOPO, both using the clinical training datasets and classification performance using the independent validation dataset. The 5-fold cross validation provided the frame work for feature extraction, parameter selection and overall classifier design. The LOPO experiment had a practical significance. In real usage, we expect the system to see and classify plaque types from entirely new pullbacks. In this experiment, in a few folds, the accuracy is lower. We conjecture that this is because when holding out a certain pullback, it may cause an imbalance of plaque types in the training set and, therefore would cause a classifier with lower accuracy. This issue was addressed in the step of the learning curve analysis, where we made sure that we had enough training examples, thus making sure that the MCC does not suffer from large variance or bias. Finally, performance generalization on an independent dataset was the experiment which was the best representative of clinical setting. Referring to the results of the experiment done on a set of independent validation images as described above (Figure 23 and Table 9) it may appear that the results are on the one hand, surprising as we thought that most errors would arise from confusing lipid and calcium. On the other hand, the results are expected when using the OVR-P rule. We found that when a lipid was confused with calcium, the confidence level was lower than $p_{thresh}$ (using MSD-OP) thus, causing the voxel to be re-assigned as “other”. This is indicated by the large number of “others” being misclassified as calcium. Generally, the majority of the errors on all

plaque types come from misclassification as being of type “other”. Further, we also see that the misclassification rate of “other” is equally good as the other plaque types or better, indicating that the OVR-P is as good as if we were able to train a classifier with features that characterize “other”. Finally, the confusion table in Figure 23 provides another useful piece of information: The main confusion between calcium and lipid is where a lipid is being classified as calcium, but not the other way around. This points to the fact that adding a lipid-specific feature may reduce the errors further.

To further improve results we “clean” the noisy OVR crisp classification results using a size-based filter as discussed above (see “Post Processing”). Our features and classification all relied on the qualitative description of the plaques as described in [32], and [71]. Therefore, when analyzing the automated results, we found that the small patches (what appears as noise in the classification results image) of calcium can/should be filtered out. The approach we took to clean the classification results has the advantage of preserving more details of the field boundary than a simple neighborhood-majority filter. However, it still has two drawbacks. The first drawback is due to the threshold on region size. Some small-size regions may not be noise while some big-size regions may be. The way we solve this problem is by looking at all of our training data and selecting the smallest VOI selected by the expert.

We can compare our results to other studies with the caveats that analyses are done on different, typically small sets of image data and that actual statistical analyses can differ. For example, Ughi et al. [141] showed a relatively high overall 5-fold cross validation accuracy of 81.5%, which is much lower than our per-voxel 5-fold cross validation accuracy of 93.6%. Further, on the practical aspect of sector-based analysis we

show 100% accuracy, which is what is needed in intervention planning. We strengthen the applicability of this approach by using independent validation dataset which is confirmed by the cryo-imaging ground truth.

The application of the proposed automated approach has significant implication in offline analysis studies in various respects. Although the current research focuses on the algorithm's accuracy rather than speed of performance we can definitely see a significant value for off-line analysis. Very large number of pullbacks can be cued for automated analysis via the cloud, putting no limit on physical location of the pullback source. The automated analysis results can be distributed to each location for review in any number of formats. For examples, if a specific range of frames is required, a visual volumetric view can be displayed such that the reviewer can move back-and-forth across frames to analyze plaque characterization.

One of the issues that will require further analysis in our future work is the problem with the one-versus-the-rest approach. In this scenario a well-known drawback is that the training sets are imbalanced. For instance, we have 3 classes each with roughly 3000 training data points, which means that the individual classifiers are trained on data sets comprising 67% negative examples and only 33% positive examples, therefore, the symmetry of the original problem is lost. This issue will be addressed in combination with the investigation of the OVR-P rejection rule since the prevalence of "other" plaque type must also be taken into account.

## 4.6 Conclusion

We have demonstrated a novel method for automated plaque classification using 3D intravascular OCT. Our method combines human expert knowledge and high level information which include geometric, optical and textural *a priori* knowledge. The algorithm has achieved robust performance with an independent validation dataset. The algorithm has the potential to improve manual plaque assessment time needed for both clinical and research purposes.

# Chapter 5 Classification of calcium in intravascular OCT images for the purpose of intervention planning

## 5.1 INTRODUCTION

Vascular disease, which extracts a terrible toll on health in the developed world, is being treated percutaneously using a variety of methods that could be improved with the use of intravascular imaging. Heart attack and stroke are the major causes of human death, and almost twice as many people die from cardiovascular diseases than from all forms of cancer combined. Coronary calcified plaque (CP) is an important marker of atherosclerosis and as such, it is important to gain understanding into CP lesion formation, as it is associated with higher rates of complications and lower success rates after percutaneous coronary intervention (PCI) [158, 159]. The CP lesion can provide an estimate of total coronary plaque burden for a patient [8-12, 160, 161], thus, concise analysis may be used to prevent and treat occlusions, which are caused by CP as soon as it is discovered.

An automatic method to segment and quantify CP in medical images would facilitate our understanding of its role in the clinical cardiovascular disease risk assessment [8]. Furthermore, current concepts in interventional cardiology highlight the need for IVOCT. First, there is a need to guide plaque modification. The presence of calcium is the strongest factor affecting "stent expansion," a well-documented metric for clinical outcome [14, 15]. IVOCT provides the location, circumferential extent, and thickness of calcium. Angiography gives no such details. IVUS detects calcium but gives no information about thickness, as the signal reflects from the front surface. As

interventional cardiologists tackle ever-more complex vascular lesions and use bioresorbable stents, there is a recent growing interest in using atherectomy devices for lesion “preparation.” Since there is a substantial economic cost and risk of complications with atherectomy [16], we should un-blind physicians with IVOCT and provide them with improved assessment of the need for atherectomy and with angular location for “directed” atherectomy. Second, there can be a geographic miss, where the stent either misses the lesion along its length or is improperly expanded, affecting its ability to stabilize the lesion and/or provide appropriate drug dosage. There is well-documented impact on restenosis.[17] Plaque dissections at the edge of a stent clearly visible in IVOCT were detected by angiography in only 16% of cases [18]. Edge dissection happens almost exclusively in areas with eccentric calcium/lipid [18], characteristics only available with intravascular imaging. Under IVOCT guidance, one can use a longer stent or apply a second stent to reduce effects of geographic miss. Third, plaque sealing is the treatment of a remote lesion that is hemodynamically insignificant (<50% stenosis) but that may appear vulnerable under intravascular imaging. Because approximately 50% of coronary events after stenting happen at remote, non-stented sites, plaque sealing is an attractive concept under investigation in trials. IVOCT’s high sensitivity for lipid plaque will be advantageous for guidance of plaque sealing.

To meet this unmet clinical need, we will develop a methodology for automatic detection of calcified plaques. The methodology we propose is a new approach for CP segmentation and is intended to perform robustly with IVOCT images encountered in the clinical environment, in real time, without the need for user interaction. In previous study done in our lab [162] we came to the realization that, in the case of plaque

characterization, due to the complexity of the different plaque compositions, when attempting to discriminate a specific, well defined plaque type (*positive*), all *positive* examples are alike, yet each *negative* example is negative in its own way. This led to our proposed algorithm, where we use a one-plaque classifier that tries to identify CP amongst all other plaques.

A CP region appears as a signal-poor or heterogeneous region with a sharply delineated border (leading, trailing, and/or lateral edges) [163]. Calcium is darker than fibrous plaque with greater variation in intensity level inside the region. A few major contributors to the variance in appearance of the different plaques are also artifacts as discussed in [89] including multiple reflection, saturation, motion etc.

In our approach, a CP image is modeled by the joint distribution of filter responses combined with edge data as derived by using a canny edge detector. This distribution is represented by texton (cluster center) distribution. Classification of a new image proceeds by mapping the image to a texton distribution and comparing this distribution to the learned models. We further enhance this unique approach by increasing robustness by introducing methods novel to plaque analysis. First, we created a dictionary using images containing all possible variations of calcium encountered in a clinical environment. In addition, we introduced an approach that minimizes the reliance on edge orientation and avoids the reliance on visible structures. In the next section, we describe the algorithms in detail. Then, we describe the validation experiments, and analyze results of the comparison with human experts.

## 5.2 Algorithms

Classification algorithms based on distribution of filter responses have been used in the past with various level of success [164, 165]. Our algorithm enhances this concept by adding various features at various stages of the algorithm. Specifically, when extracting features, we add a very plaque-specific feature set we name DGAS (stands for Distance, Gradient, Average and Smoothness) as described below. Our algorithm is divided into four main steps: processing for extraction of image-wide features, dictionary creation, model creation (training) and classification (prediction).

### *5.2.1 Image Processing for extraction of DGAS features*

In the initial step, before the SIs are extracted, all images are passed through canny edge detector [166] preceded by blood vessel mask extraction (the mask includes all pixels between the lumen border and the back border [167] and guidewire artifact removal [119]. This enables each pixel to be assigned a global edge feature vector (features of edges extending over a length in the image) set referred to as DGAS feature set (these are five real-valued features). The DGAS feature set includes distance of the pixel from the lumen, continuous edge gradient magnitude, continuous edge gradient direction (together, they express the acutance of the edge), average edge intensity and edge smoothness computed as the second derivative of the image (i.e. Laplacian) [137]. Notice that these features are assigned based on edge which are found by processing the complete frame, thus, continuity across SIs is preserved. Following this step, SIs are extracted as described below.

### *5.2.2 Calcium Texton Dictionary Creation*

In the dictionary creation step (Algorithm, part 1), we obtain a finite set of local structural features that can be found within a large collection (40 randomly selected from the CA-DS set described below) of calcium SIs from various pullback images. We follow the hypothesis that this finite set, which we call the calcium texton dictionary, closely represents all possible local structures for every possible calcium instance in a pullback.

> **Textons:** We characterize a calcium SI by its responses to a set of linear filters (filter bank, *F*) combined with edge features (DGAS feature set). We seek a set of local structural features (filter responses) which is targeted towards having largest response representing the calcium specifically. This approach leads to our main four-part proposal: First, to use a filter bank containing edge and line filters in different orientations and scales. Second, optionally, select a subset taking into account only the strongest responses across all orientations (thus providing orientation invariance). Third, based on the concept of *textons* and its generalizations introduced by Malik et al. [168] we use the concept of clustering the pixel responses into a small set of prototype response vectors we refer to as *textons*. Note that by adding to each filter response vector the DGAS feature set, we enable the addition of spatial relationships between adjacent SIs in the form of continuous borders within the image.

***Init*** : split CA-DS into 2 ***disjoint*** sets: dictionary, training&testing (for model creation)
***input***: 40 calcium sub-images.
***output***: dictionary of textons ($\in \mathbb{R}^{K \times n}$)
***for each sub-image {***

a. Create filter bank, *F*
b. Convolve with filter bank, F ( $\in \mathbb{R}^{n_f}$ ) and record convolution value.
c. Combine with DGAS feature set - $\mathbb{R}^n$ for each pixel

}
Concatenate all calcium pixel responses
Create *K* clusters for each group via K-means (Identify *K* via "elbow" method).
Output dictionary

Algorithm, part 1: Dictionary creation

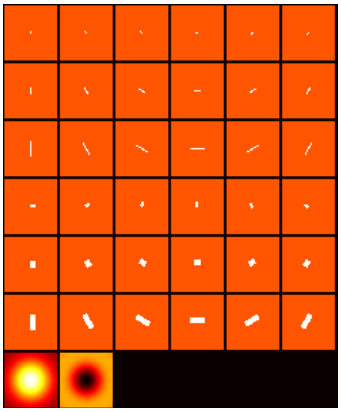

Figure 25: Filter bank designed to capture the calcium characteristics. Each row represents a different scale, where the upper three rows are bar filters in 6 orientations, the three middle rows are edge filters in six orientations and in the last row, Gaussian and Laplacian of Gaussian filters. To generate the MR8 filter responses, only 8 responses are recorded by taking maximal response at each orientation, the Gaussian, and the Laplacian of Gaussian.

**Filter bank, F**: We designed a special filter bank, in an attempt to capture the qualitative description of calcium as signal-poor or heterogeneous region with a sharply delineated border [32, 89]. We then investigate the maximum response filters over the orientation (MR8) versus the entire filter bank. It is shown that by doing that we reduce computation effort significantly with minimal loss in performance. The full filter bank (Figure 25) consists of a Gaussian and a Laplacian of Gaussian filters, an edge filter at three scales and six orientations and a bar filter (a symmetric oriented filter) at the same three scales and orientations, giving a total of 38 filters. When using the maximum response filters, the output dimensionality is reduced by recording only the maximum filter responses across all scales, therefore, yielding one response for each of the upper six rows in Figure 25, where the Gaussian and Laplacian of Gaussian are recorded always,

hence MR8. In the MR8 case, the final vector of filter responses consists of eight numbers.

### *5.2.3 Model Creation*

In the model creation step (Algorithm, part 2), the remaining $m_t$ SIs subset from the CA-DS is used. Each of these training SIs is convolved with $F$, generating a vector of filter responses which is concatenated with the DGAS feature set, thus creating a pixel response vector ($\in \mathbb{R}^n$) for each of the SIs pixels. This vector is compared with the dictionary described above using k-nearest neighbors (k-NN) thus each pixel of the SIs pixels is assigned a label creating a label vector whose length is the number of pixels in the SI. We then quantized this label vector into a histogram (with $L$ bins) of texton frequencies. Finally, the texton frequency histogram is converted into a texton probability distribution, by normalizing the texton frequency histogram to sum to unity. The reason we normalize the histogram is to avoid the need of the various SIs to have the same size or shape. This process is repeated for all $m_t$ training SIs, thus the final outcome of this process is a matrix whose dimension is $m_t \times L$ which is used as the training dataset for one class Support Vector Machine classifier (OC-SVM) as described below.

**Texton probability distribution (normalized histograms):** The histogram of image textons is used to encode the global distribution of the local structural attributes (i.e. the filter bank's responses and the DGAS feature set) over the calcium texture image while ensuring that every shape and size of SI can be part of the experiment. This representation, is a discrete function of the labels $l$ derived from the texton dictionary. Each SI is filtered using the same filter bank, $F$, and its

*DGAS* feature set is computed the same way. Each pixel within the SI is represented by a one-dimensional ($\in \mathbb{R}^n$) feature vector which is labeled (i.e. assigned a texton number) by determining the closest image texton using k-NN algorithm. The spatial distribution of the representative local structural features over the image is approximated by computing the normalized texton histogram.

The dimensionality of the histogram is determined by the size of the texton dictionary, *K*, which should be comprehensive enough to include large range of calcium appearances and the number of bins, *L*, used to create the histogram. Therefore, the histogram space is high dimensional and a compression of this space is suitable since computation time is a factor at the event of on-line processing. This may be an essential requirement, provided that the properties of the histogram are preserved.

***input***: dictionary & training sub-images
***output***: calcium plaque *model*
***For each training sub-image {***
a. Convolve with filter bank, F and record convolution value.
b. Combine with DGAS feature set ($\mathbb{R}^n$ for each pixel)
c. Label each pixel response by comparing to the dictionary (using k-NN)
d. Create histogram of label frequencies
e. Normalize to get distribution (hence, sub-images do not need to be of the same size)
***}***
Assemble all histogram vectors into a single matrix ($\in \mathbb{R}^{m_i \times K}$)
Train a one-class SVM to get the *model*

Algorithm, part 2: Model creation.

***input***: test sub-images, dictionary, *model*.
***output***: label (calcium, non-calcium)
***For each new sub-image {***
a. Convolve with filter bank, *F* and record convolution value.
b. Combine with DGAS feature set ($\mathbb{R}^n$ for each pixel)
c. Label each pixel response by comparing to the dictionary (using k-NN)
d. Create a histogram of label frequencies
e. Normalize to get distribution (hence, sub-images do not need to be the same size)
f. Predict using OC-SVM *model*
***}***

Algorithm, part 3: Classification rule for new data.

## 5.3 Classification Rule: One-class Support Vector Machine (OC-SVM)

For classifying new data, we use a one-class classifier. In this step, (Algorithm, part 3), we do not have stand-alone SIs since the only input to the *automated* algorithm is an IVOCT pullback. We scan the pullback within the blood vessel mask, one frame after the other in ($r$-$\theta$) view, with a window whose size was determined by the size of smallest calcium region required for measurement (100x100 in our experiments) and with a step which is equal to half the window size (ensuring 50% overlap). Each window is treated as an SI. The same procedure as done in the training step is followed to build a histogram corresponding to the new SI. This histogram is the new data point, which is used by the trained OC-SVM classifier for classification, producing the final SIs classification as calcium or non-calcium as described below.

There is a reason for selecting the one-class paradigm: The traditional multi-class classification paradigm aims to classify an unknown data object into one of several pre-defined categories (two in the simplest case of binary classification). A problem arises when the unknown data object does not belong to any of those categories. When analyzing plaque in IVOCT images, it is challenging to decide what the plaque type is, especially because there are many plaques types other than the main three plaque types typically being analyzed (calcium, lipid, fibrous). One-class classification algorithms aim to build classification models when the negative class is absent, either poorly sampled, or not well defined (where the latter describes our case). This unique situation constrains the learning of efficient classifiers by defining class boundary just with the knowledge of *positive* class. In our problem, the calcium plaque type is defined as *positive* and everything else is *negative*. We decided to use one-class-SVM (implemented using

libsvm library [169]) because of the following reasons: First, it is effective in high dimensional spaces even in cases where number of dimensions is greater than the number of samples, second, it is very versatile since different kernel functions can be specified for the decision function including custom kernels.

One-class SVM was suggested by Scholkopf et al.[144] where the approach is to adapt the binary support vector machine classifier (SVM) methodology to one-class classification problem, which only uses examples from one-class, instead of multiple classes, for training. The one-class SVM algorithm first maps input data into a high dimensional feature space via a kernel function, $\Phi(\cdot)$, and treats the origin as the only example from other classes. Then the algorithm learns the decision boundary (a hyperplane) that separates the majority of the data from the origin. Only a small fraction of data points, considered outliers, are allowed to lie on the other side of the decision boundary. The hyperplane is found iteratively such that it best separates the training data from the origin. The kernel that guarantees the existence of such a decision boundary is the Gaussian kernel [144] and, therefore, was selected to be the kernel used in this study.

Considering that our training dataset $x_1, x_2,\ldots,x_l \in X$, $\Phi(\cdot)$ is the feature mapping $X \rightarrow F$ to a high-dimensional space. We can define the kernel function as:

$$k(x, y) = \Phi(x) \bullet \Phi(y)$$

Using kernel functions, the feature vectors need not be computed explicitly, greatly improving computational efficiency since we can directly compute the kernel values and operate on their images. We used the radial basis function (RBF) kernel:

$$k(x, y) = e^{-\|x-y\|^2/2\sigma^2}$$

Solving the one-class SVM problem is equivalent to solving the dual quadratic programming (QP) problem:

$$\min \frac{1}{2}\|w\|^2 + \frac{1}{\nu l}\sum_{i=1}^{i} \xi_i - \rho$$

subject to

$$(w \bullet \Phi(x_i)) > \rho - \xi_i, \; i = 1, 2, ..., l, \; \xi_i > 0$$

where ρ is the bias term and $w$ is the vector perpendicular to the decision boundary. $\xi_i$ is the slack variable for point $i$ that allows it to lie on the other side of the decision boundary. $\nu$ is a parameter that controls the trade-off between maximizing the number data points contained by the hyperplane and the distance from the hyperplane to the origin. It has two main functions: it sets an upper bound on the fraction of outliers (training examples regarded out-of-class) and, it is a lower bound on the number of training examples used as support vectors. Finally, the following function is the decision rule of the OC-SVM: It returns a positive value for normal examples $x_i$ points (i.e. *positive*) and *negative* otherwise.

$$f(x) = sign((w \bullet \Phi(x)) - \rho)$$

## 5.4 Experimental Methods

### *5.4.1 IVOCT Image Acquisition and selection of regions for SI extraction*

Images were collected on the C7-XR system from St. Jude Medical Inc., Westford, MA. It has an OCT Swept Source having a 1310 *nm* center wavelength, 110 *nm* wavelength range, 50 kHz sweep rate, 20 mW output power, and ~12 *mm* coherence length. The pullback speed was 20 mm/s and the pullback length was 54 mm. A typical pullback

consisted of 271 image frames spaced ~200 $\mu m$ apart. Images used in this study were selected from the database available at the Cardiovascular Core Lab of University Hospitals Case Medical Center (Cleveland OH). They consisted of 35 IVOCT pullbacks of the Left Anterior Descending (LAD) and the Left Circumflex (LCX) coronary arteries of patients acquired prior to stent implantation. These images were manually analyzed by an expert from the Core Lab to identify images of calcium, lipid, and fibrous plaques. See Figure 26 for a few examples of the CP appearance as compared to the other plaque types in a typical pullback ($r$-$\theta$) view.

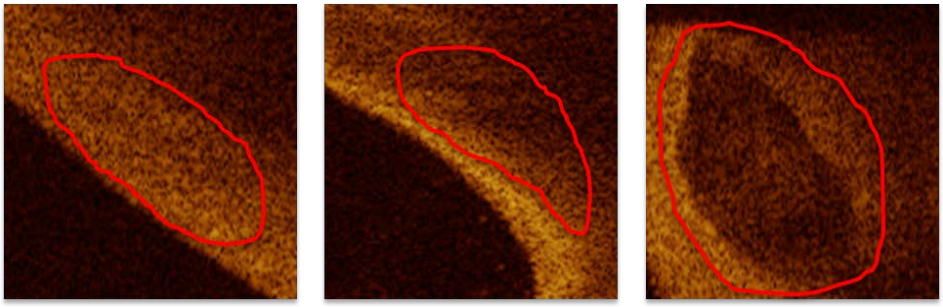

Figure 26: Images in (r-θ) view showing the different appearance of the main three plague types: left, fiber; middle, lipid; right, calcium. It is shown that the calcium has a few distinctive characteristics which are apparent in the images: sharp borders with low average intensity and low attenuation (beam goes from left to right) within the calcified region.

The training dataset was created from de-identified clinical images in the set described above. An expert reviewed pullbacks and identified regions containing plaques (fibrous, lipid, or calcified) utilizing consensus criteria descried [163]. This was followed by identifying sub-images (SIs) which were generated by cropping a region in the image and the rest of the image was regarded as background data which was discarded. All processing is done on these cropped regions we refer to as sub-images (SIs).

For validation testing, we created an independent (not used in training) image dataset with each voxel accurately labeled and validated by 3D cryo-imaging [149]. To

create this dataset, we obtained coronary arteries (LADs) of human cadavers within 72 hours of death and stored at 4 °C. Arteries were treated and stored in accordance with federal, state, and local laws by the Case Institutional Review Board. To prepare for IVOCT imaging, arteries were trimmed to approximately 10 cm in length. A luer was then sutured to the proximal end of each vessel which was flushed with saline to remove blood from the lumen. Major side branches and the distal end of each artery were sutured shut. Using super glue, the artery was adhered to the sides and bottom of a rig that was used to minimize motion between cryo and IVOCT imaging procedures. IVOCT imaging conditions mimicked the *in-vivo* acquisitions described above. Sutures were placed on the vessel to identify ROIs (1.5–2cm in length) that would later be analyzed using cryo-imaging. Following IVOCT imaging, the entire imaging rig containing the artery was flash frozen in liquid nitrogen, and stored at -80 °C until cryo-imaging was performed. Prior to cryo-imaging, arteries were cut into blocks corresponding to the ROIs determined during IVOCT imaging. Blocks were placed in the cryo-imaging system and allowed to equilibrate to the -20 °C cutting temperature. The ROIs were then alternately sectioned and imaged at 20 μm cutting intervals and color and fluorescent cryo-images were acquired at each slice. The process was repeated until the whole specimen was imaged.

## 5.5 Training, Testing and Dictionary Datasets

The following four datasets, which were assembled from the above pool of SIs, were used in the experiments: CA-DS (stands for Calcium Data Set) composed of 316 calcium-only SIs, LI-DS composed of 250 lipid-only SIs, FI-DS composed of 250 fiber-

only SIs and NON-DS, composed of approximately 750 SIs which are neither one of the main plaque types.

In addition, we also created an independent (in the sense that data from it were not part of the training or any other experiment) dataset which is extracted from a cadaver where each pixel is annotated using cryo-based ”ground-truth” images as a confirmation of annotation, thus removing reliance on expert’s interpretation of qualitative plaque description. We name this dataset “validation dataset”.

## 5.6 Experiments

We compare the performance of the method using two filter banks, the full filter bank and the MR8 version of it (see below for a full description). In the following experiments, a *positive* example is an example that came from calcified dataset and a *negative* example is an example that is drawn from any dataset other than calcified dataset.

1. Stratified five-fold cross validation (SFV-CV) experiment: In one-class classifier, class boundary (model) is determined by just using the knowledge of the *positive* class, allowing some outliers (*negatives*) to be present [170]. To create the one-class model, we combine the CA-DS with 15 *negative* examples (2-3 from each type). Then perform stratified 5-fold cross validation.
2. *Leave-one-pullback-out* (LOPO): The idea is to quantify the generalization capability of the classifier to new pullbacks. Although this approach repeats the same logic as the SFV-CV approach described above, there is one important difference: the left out set is not randomly selected from the dataset but is chosen such that all samples belong to the same pullback are held out. This represents a much more realistic

condition in our application, thus is a better indication of the classifier ‘sability to. We use 35-fold (because we have data from 35 different pullbacks) cross validation where we use the CA-DS set combined with a small number (2-3) examples from each of the other sets. For each of the folds, the dataset corresponding to one pullback’s images is held out and constitutes the cross validation set, while the other datasets constitute the training set. Note that this is a much more stringent and realistic condition as opposed to randomly partitioning the dataset as done in the SFV-CV experiment, since in real usage, we expect the system to see and classify plaque types from entirely new pullbacks.

3. Next experiment is intended to measure the confusion between calcium and the other plaque types. We combine the CA-DS with each of the other datasets described above and run a classification experiment. We create two mixed sets (CA-DS and FI-DS when testing against fiber and CA-DS and LI-DS when testing against lipid) and we perform internal stratified 5-fold cross validation. We divide the CA-DS into 5 folds and the mixed set into 5 folds. In each of the folds, we use a fold which is composed of only CA-DS examples for training and then we do the prediction on the rest of the CA-DS folds combined with the FI-DS/LI-DS folds. This gives a better balanced dataset and enables us to create accuracy results (as opposed to $F_1$ score) since the data is minimally skewed. The goal of this experiment is to quantify the amount by which the calcium can be discriminated from the other main plaque types. This also helps focus our attention on the more “problematic” plaque type, thus increase the overall performance of the classifier.

4. Finally, to further increase our confidence we use the validation dataset to classify never-seen-before datasets.

As performance measure, we use $F_1$ score, which can be interpreted as a weighted average of the precision and recall values. We follow standard nomenclature where we use TP (true positives), FN (false negative), FP (false positive), and TN (true negative) to make assessments of (P)recision = TP/(TP+FP), (R)ecall = TP/(TP+FN), $F_1$ = 2PR/(P+R). (ACC)uracy = (TP+TN)/(TP+FN+FP+TN).

## 5.7 Results

Before analyzing the algorithm's performance, it is essential to determine all of its parameters to ensure good performance. We show that using the MR8 as opposed to the full filter bank, does not impact significantly the final outcome, yet the speed is improved.

### *5.7.1 Algorithm Parameters*

We optimized algorithm parameters in multiple steps. First, we determined the two OC-SVM parameters to be used in all subsequent analyses. These parameters are $\sigma$, the RBF kernel's bandwidth and $\nu$, which according to [144] can be viewed as either the upper bound on the fraction of outliers (in our case, we simply set this value to be the number on non-calcium SIs used in the training divided by the total number of training SIs). Or, it can also be viewed as a lower bound on the number of training examples used as support vectors. This good initial value enables us to perform an efficient grid search for best parameters for the OC-SVM. In this grid search we were able to find the best $\sigma$ for the

radial basis function (RBF) and fine-tune the initial ν. The final values were: ν=0.0896 and σ=0.0313.

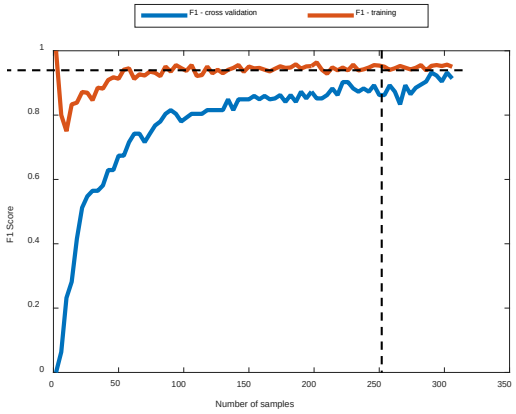


Figure 27: Learning curve analysis for a OC-SVM. Here we use $F_1$ score as performance measure. The vertical dashed line is the minimal number of data points which will enable high enough performance (280). The horizontal dashed line represents the steady state $F_1$ score which is the best possible performance given the current training data.

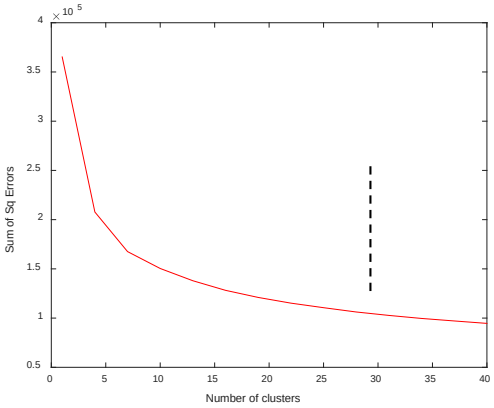


Figure 28: Finding the optimal number of textons by plotting the within-cluster sum of squared distances vs. the number of clusters.

Second, we verified that the number of training examples was sufficient to enable efficient training of the OC-SVM. We performed a learning curve analysis where we varied the number of samples and compared the training and the cross validation $F_1$ score until they converged (Figure 27). This gave us a good starting point to ensure minimal over/under fitting is minimized. We selected to use the $F_1$ score as performance matrix, since, as it is typical with one-class classification, the number of *negative* examples is very small compared to the *positive* examples, causing the overall dataset to be skewed. It is shown that for cross validation $F_1$ score to reach that of training $F_1$ score, approximately 280 examples are sufficient (each point is a point in feature space, meaning, it represents a single SI).

Third, to find the best number of textons to be used in the dictionary, we used the "elbow" approach by plotting the sum of the within-cluster square of Euclidean distances versus increasing number of clusters and observed where the "elbow" occurred. As shown in Figure 28, the optimal number of textons for the calcium dictionary was $K$=29. This value was used in all subsequent processing of SIs.

Fourth, we determined the optimal size of the kernel to be used in the filter bank. To do that, we created a dictionary of 29 calcium clusters and then ran the classification algorithm on CA-DS set using the full kernel and then using the MR8 version of the filter bank's responses. The idea was to be able to derive the best kernel size rather than get the optimal performance measure. We ran 5-fold cross validation of the created datasets for varying values of filter kernel (Figure 29). The optimal kernel size, which was found in this experiment, was 19 x 19 for full filter bank and 15 x 15 for the MR8 filter bank.

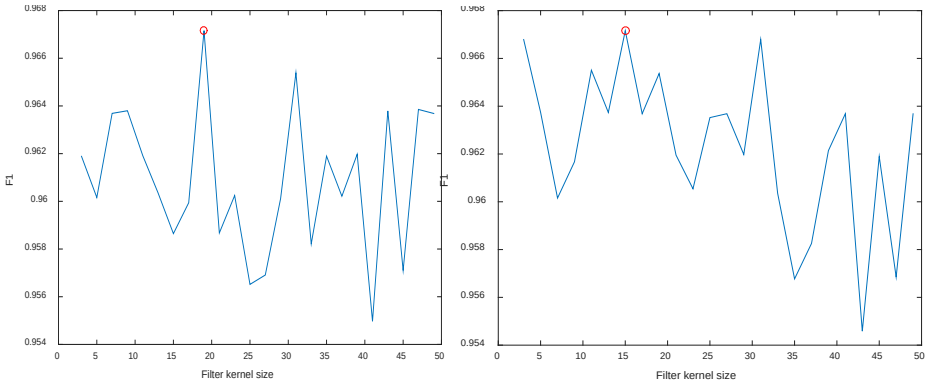


Figure 29: Determination of filter bank's kernel size. 5-fold cross validation performance (using $F_1$ score as a statitical measure) performed by varying filter kernel size. (left) plot of $F_1$ score variation for full kernel filter bank. (right) $F_1$ score variation for MR8 filter bank. Red circles indicate the location of best performance size (full kernel, kernel is 19x19, MR8 kernel is 15 x 15).

### *5.7.2 Training and Model Creation using Regions from Clinical Dataset*

Results of the SFV-CV and the LOPO experiments are shown in Table 10. First, we note that, the MR8 performs as well as the full filter bank. This is a clear indicator that

orientation invariant description is not a disadvantage (i.e. salient information for classification is not lost). Second, the fact that MR8 does as well as the full filter bank is also evidence that it is detecting the most distinctive features. These results are encouraging since reduction of the features space down to 8 from 38 is a significant computational advantage, making the process more suitable for on-line usage.

| | **SFV-CV** | | **LOPO** | |
|---|---|---|---|---|
| | **Full filter bank** | **MR8** | **Full filter bank** | **MR8** |
| $F_1$ Score | 0.929±0.026 | 0.933±0.027 | 0.815±0.265 | 0.825±0.258 |
| Precision | 0.986±0.015 | 0.975±0.016 | 0.899±0.274 | 0.894±0.273 |
| Recall | 0.879±0.046 | 0.896±0.048 | 0.785±0.278 | 0.866±0.266 |

Table 10: Performance statistics for the two experiments (showing mean±sd), SFV-CV and LOPO.

In the next experiment, we tested the calcium against each of the other main plaque types (Table 11). It is evident that calcium and fibrous are more easily discriminated compared to calcium and lipid. It suggests that we should consider designing additional filters that not only favor the calcium plaque characteristics but also favor the lipid characteristics. Moreover, we see that the results when using the responses of the full filter are better than when we just use the maximum responses.

| | **5-fold cross validation** | |
|---|---|---|
| | **Full filter bank** | **MR8** |
| | mean±sd | mean±sd |
| Ca-v-lipid | 0.762±0.07 | 0.743±0.004 |
| Ca-v-fiber | 0.835±0.016 | 0.814±0.018 |
| Ca-v-all | 0.778±0.012 | 0.759±0.010 |

Table 11: Performance of calcium classification versus classification of the other main plaque types.

### *5.7.3 Evaluation on Independent Validation Dataset*

We evaluated our algorithm performance on the independent validation dataset confirmed with cryo-imaging. Example result (Figure 31) show cryo and IVOCT input images,

manual plaque annotations, and classifier outputs. For the purpose of quantifying the automatic calcification on the validation dataset, we counted the number of SIs scanned where classification is considered TP if more than 25% of the SI covered a true calcified region. Using this criterion, the performance of the scanned image shown in Figure 31 is shown in the form of a confusion table (Figure 30). Clearly, due to the fact that the majority of the SIs scanned are not calcium, using accuracy will not reflect the performance accurately, so we choose to compute the $F_1$ score as described above, yielding $F_1 = 0.72$.

| | | Actual | |
|---|---|---|---|
| | | Calcium | Non-calcium |
| predicted | Calcium | **9** | **2** |
| | Non-calcium | **5** | **493** |

Figure 30: Confusion table showing independent validation image classification results (Figure 31)

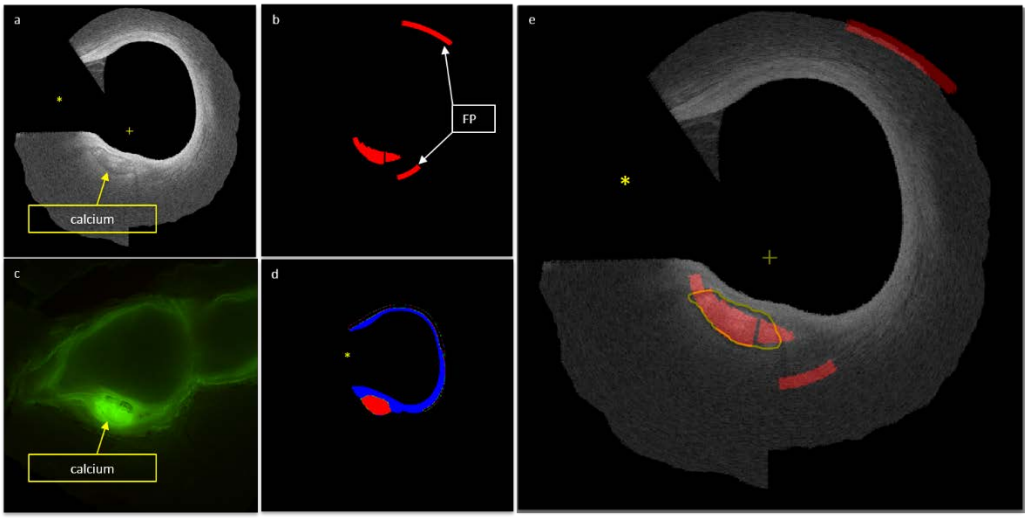


Figure 31: Independent validation classification. a) Original IVOCT imaged where the guidewire (marked by yellow asterisk) and data beyond lumen and back border are masked out. Notice the calcified region with sharp borders. b) Results of automated classification. C) Corresponding registered cryo-image. Notice how the calcified region is much brighter when using fluoroscopy. D) Expert annotation of the plaque types present in the image (blue is fiber and red is calcium). e) IVOCT image with automated classification overlay. The yellow line represents the experts annotation of the calcified region (can also be seen in part a). Red represents the classification and the blue represents fiber, the "+" sign represents the center of the image.

Finally, in terms of time performance, the MR8 yielded a classifier which is more than 30% faster, yet, as can be seen in the results above, the accuracy measurements are not significantly affected. When using MR8 filter bank, the average time to compute features (histogram) for a single frame is 2.6 seconds and for full filter bank 3.7 seconds (measured by running Matlab). This means that the feature creation using MR8 filter bank is 30% less expensive than full filter bank, thus making the algorithm suitable for on-line application.

## 5.8 Discussion

The presence of calcium in the coronary arteries is an indication of intimal atherosclerosis [171]. Because of the demonstrated value of coronary calcium detection

in predicting significant coronary disease and because of its independent predictive value for coronary events [172], it is important to be able to precisely and efficiently detect and quantify coronary calcium.

Automated calcium plaque classification represents the key step to help in treatment decision making in clinical settings and reduce the human interaction during post-procedure analyses. We have presented a novel approach for completely automatic intravascular calcium classification in close to real time performance which significantly improves on the state of the art [141]. It presents the following advantages. First, our model representation captures efficiently "texture like" visual structures where we do not impose any constraints on, or requiring any a priori knowledge of, the catheter type, IVOCT machine type or any other conditions under which the images were acquired. The second is the learning algorithm which does not require manual extraction of objects or features. The third is the independence of region segmentation and feature extraction, which are never perfect. Finally, we have shown that the results of the reduced filter bank (MR8) do not significantly affect the performance, yet speed is improved by more than 30%, a very important parameter to consider when an on-line application is required.

In Figure 31, we note two important "artifacts" which are caused by the scanning algorithm: First, the classifier's output looks bulky. This is due to the way we extract SIs from a new pullback: we scan the image with a scanning window that is being labeled in its entirety as calcium or non-calcium, there is no partial-window labeling. This results in over estimation of the calcified region however, it preserves the ratio between different sizes of circumferential calcified regions. Second, the farther the scanning window is from the catheter in r-θ view, the larger the size in Cartesian view is (a square in r-θ view

is transformed into an arc in Cartesian view). This causes the area in Cartesian view to look as if it is larger. This characteristic is also shown in the false positives (part b). Another thing to note is the fact that the classifier can discriminate calcium from any other plaque type (in this case, fiber). This emphasizes the advantage of using a one-class classifier, where the classifier does not have to classify one class or the other, but it simply indicates if a plaque belong to the class of interest (calcium) or not, a very elegant solution to a problem other researchers encountered [103, 134, 141, 167].

Our choice of one-class classifier approach can be proven useful in another aspect. Because a one-class classifier defines class boundary just with the knowledge of *positive* class ("*positive*" being the class of interest, calcium in our case), we can use its parameter such that they reflect expert annotation quality. For example, we can create a one-class classifier model, using cryo-imaging as annotation tool (as done in our study as described above). We can then compare the classifier results to, say, three experts, and quantify the quality of their annotation according to their deviation from the model. Since we assume that cryo-based-imaging is a reliable ground truth, this quantification can be used a scoring mechanism for expert annotation.

Finally, we are continuously working to improve the results in several ways: We will improve the visualization of the scanning window such that when switching between $r$-$\theta$ view and Cartesian view, the classified area is preserved. Pixel-based feature set will be improved using a different or enhanced feature set (i.e. improved dictionary). SI-based feature set will be enhanced by modifying histogram creation combined with additional SI-specific features. Dimension reduction will be addressed to adjust the method to cope with very large pullbacks. In addition, we will address the incorporation of a post-

processing step in the third dimension (i.e. along the pullback direction). This way the impact of the spatial variability of coronary cross-sectional morphology will be reduced and the accuracy of the classification will increase.

## 5.9 Conclusion

We have demonstrated an *automatic* method for calcified plaque segmentation. The promising results show that the method has the potential to be used in the clinic to facilitate quantitative analysis of intravascular IVOCT images. Although additional validation is needed, the presented method holds great promise for reliable, robust, and clinically applicable segmentation of calcium in IVOCT image sequences on and off line, thus change clinical practice.

## 5.10 Acknowledgement

This project was supported by the National Heart, Lung, and Blood Institute through grants NIH R21HL108263 and 1R01HL114406-01, and by the National Center for Research Resources and the National Center for Advancing Translational Sciences through grant UL1RR024989. These grants are collaboration between Case Western Reserve University and University Hospitals of Cleveland.

# Chapter 6 Automated Volumetric Intravascular Plaque Classification Using Optical Coherence Tomography (OCT)

## 6.1 Introduction

Cardiovascular diseases are the leading cause of death worldwide. An estimated 17.5 million people died from a cardiovascular disease in 2012, representing 31% of all global deaths. Of these deaths, an estimated 7.4 million were due to coronary heart disease and 6.7 million were due to stroke [173]. The underlying disease process in the blood vessels that results in coronary heart disease (heart attack) and cerebrovascular disease (stroke) is known as *atherosclerosis*. It is a complex pathological process where fatty material and cholesterol are deposited inside the lumen of medium and large-sized blood vessels (arteries). These deposits (plaques) cause the inner surface of the arteries to become irregular and the lumen to become narrow, making it harder for blood to flow through. Further, the plaque can rupture, triggering the formation of a blood clot, which may eventually lead to disease.

To treat atherosclerosis, we must first have access to an imaging technique with suitable resolution. As we describe in the next section, the recently approved intravascular optical coherence tomography (IVOCT) approach fulfills this need. In IVOCT, a probe is inserted into a blood vessel. As the probe moves through the vessel, it collects images of the vessel wall. These images are subsequently analyzed by experts to identify at-risk regions.

A major issue when working with IVOCT, however, is that it can produce more than 500 image frames in a single scan, resulting in an explosion of image data. This can

be difficult and labor-intensive to analyze manually, taking up to one hour of examination for each frame by a trained analyst. This often precludes measurements from every frame, and plaque classification is not even done because it is infeasible in terms of time. Further, this manual process is also prone to error. In prior work [83] , our group has found evidence of up to 5% intra and 6% inter-rater variability among analysts looking at these images.

The goal of our work is to enable an effective detection and diagnosis of atherosclerosis, which is a necessary precursor for effective treatment. We do it in three ways: (i) reduce the effort involved, (ii) improve the accuracy of high-risk plaque identification and (iii) make the diagnosis available as early in the process as possible. The prevalence of atherosclerosis means achieving these goals can have a major impact on health worldwide.

We anticipate fulfilling our goals in two steps. In the first step, reported in this chapter, we develop an automated method to process single frames generated by IVOCT scans. We demonstrate that it is accurate and efficient on real IVOCT data, it outperforms a previously published baseline [141] , and the output can be used by analysts to greatly reduce their annotation effort. In the second step, our goal is to integrate this approach into a real time visualization that accompanies an IVOCT scan. We would like to produce 3D images as in Figure 1, by stacking the output of multiple 2D frames. These images will be annotated with different detected plaque types, and will be used for rapid identification of high-risk regions for intervention and management and guidance.

In the rest of the chapter, we first describe IVOCT. Next, we describe how we extract meaningful features from IVOCT images for our automated analysis, followed by

a description of our classifier. We then describe empirical results that illustrate the performance characteristics of our approach, and discuss current limitations and future work.

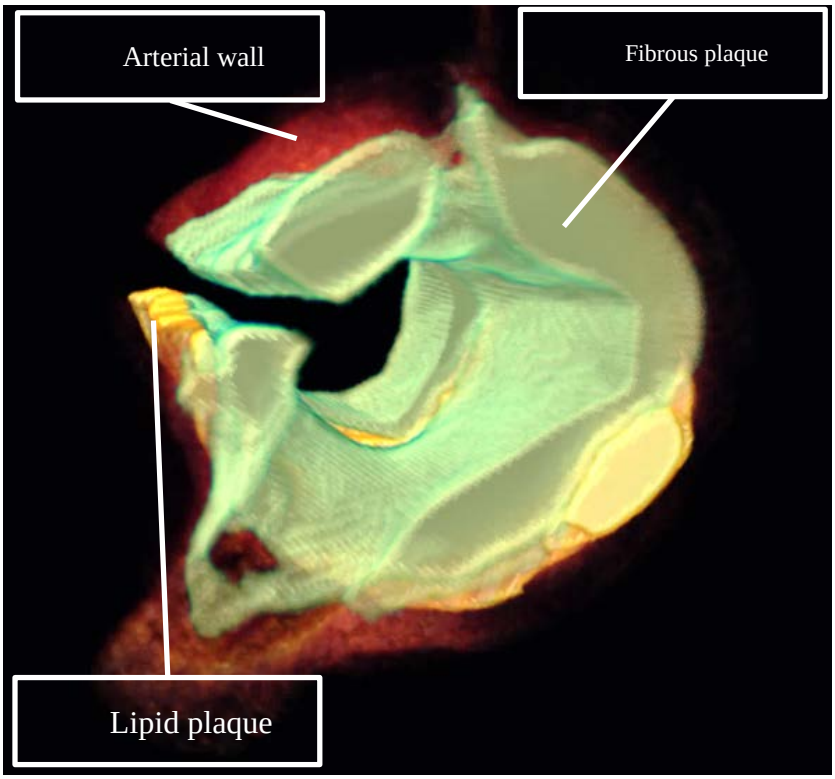


Figure 32: Example of desired 3D output (using current automated approach's output). This greatly enhances the physician's ability to make (pre)treatment decisions.

## 6.2 Optical Coherence Tomography (OCT)

Before OCT was approved, Intravascular Ultrasound (IVUS) was used to identify plaques. IVUS has a resolution of ~200 μm and is able to detect for example, calcium. However, it cannot measure the distance between the superficial calcium and the lumen, nor can it assess the thickness of calcium due to acoustic distortion [174] . The underlying concept of OCT is similar to that of ultrasound; by measuring the delay time of optical echoes reflected or backscattered from subsurface structures in tissues, we can obtain structural

information as a function of depth within the tissue [89]. However, OCT does not possess the limitations of IVUS.

In IVOCT we obtain cross-sectional images by inserting a flexible imaging probe (catheter) into the blood vessel to be imaged. The catheter has an optical fiber coupled to a lens and micro-prism. The micro-prism reflects the OCT beam perpendicular to the catheter longitudinal direction and captures the light that is back-scattered from that tissue (the reflected beam is referred to as an *A-Line*). The probe is then rotated and pulled back. This *pullback* creates a two-dimensional image (referred to as *polar* or *r-θ* image) by assembling successive A-lines next to each other resulting in an image shown in Figure 33b. This image is then transformed to Cartesian coordinates to produce the image shown in Figure 33c. A typical pullback contains 271 images covering 54*mm* and an image contains 504 A-lines.

Different tissues have different qualities that influence the back-reflectance. The longer the distance traveled, the longer the delay in returning to a detector. The delay in the returning light from deeper structures compared with shallow structures is used to reconstruct images.

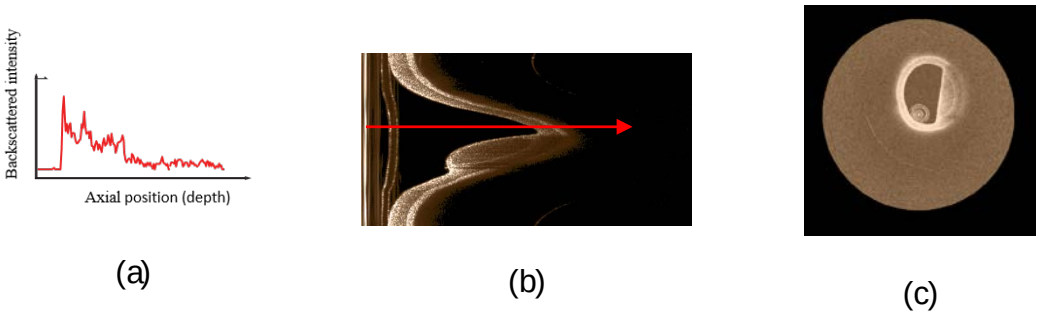


Figure 33: (a) Backscattered intensity of a single A-line (b) polar (r-θ) image (the red line is the A-line in (a)). (c) the polar image converted to the more human readable x-y.

Since its approval for clinical use, IVOCT has become an invaluable tool for vascular assessments due to its high contrast and microscopic resolution (5-15 μm), which is superior to other *in-vivo* imaging modalities such as IVUS. It has been shown that IVOCT is able to distinguish between key types of plaque [32] , and aid in assessment of new coronary artery stent designs [83, 88] . These characteristics make it ideal for our purposes.

Our group has access to a large database of manually analyzed OCT images obtained in a clinical setting. Images were collected on the C7-XR system from St. Jude Medical Inc., Westford, MA. It has an OCT Swept Source having a 1310 *nm* center wavelength, 110 *nm* wavelength range, 50 kHz sweep rate, and ~12 *mm* coherence length. The pullback speed was 20 mm/s and the pullback length was 54 mm. Images from this source were used in training our machine learning approaches, described below.

## 6.3 Representing an OCT Image

In order to build our system, we need to automatically and accurately identify different plaque types in OCT images. In this section, we describe image characteristics that are key to identifying different plaque types. In constructing our features we use the qualitative description of the different plaques' characteristics in prior work [32] described below. This also provides the ability to interpret results in a meaningful way.

A **fibrous plaque (**Figure 34 part A**)** has high backscattering and the region has relatively homogeneous intensity values. We see that the average intensity is high (bright). Likewise, the intensity is not attenuated much along the A-line.

A **lipid plaque (**Figure 34 part B**)** is a low intensity region with poorly delineated borders, a fast IVOCT signal drop-off, and little or no OCT signal backscattering, within a lesion that is covered by a fibrous cap. We see that the intensity starts very bright and decreases quickly along the A-line.

A **calcified plaque (**Figure 34 part C**)** appears as a low intensity or heterogeneous region with a sharply delineated border (leading, trailing, and/or lateral edges). Calcium is darker than fibrous plaque with greater variation in intensity level.

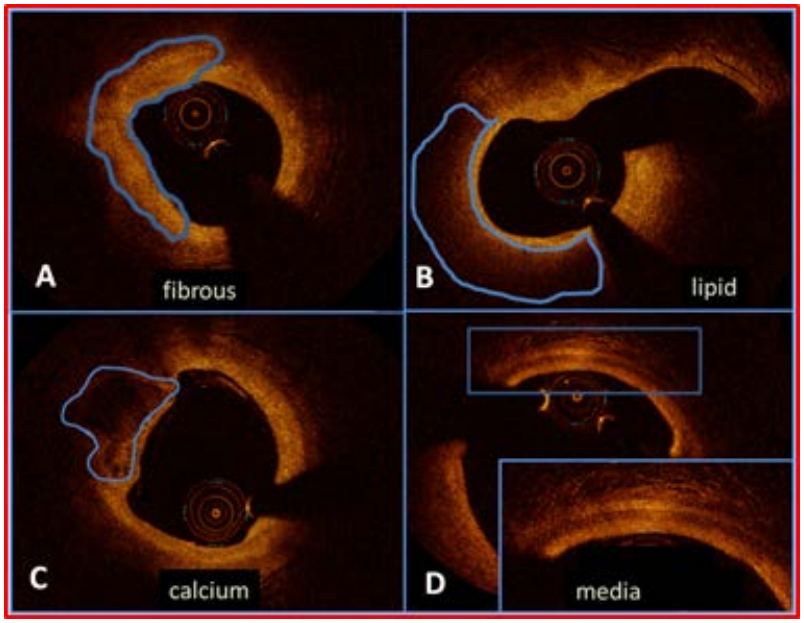


Figure 34: Appearance of plaque types in clinical images. A is fibrous, B is lipid and C is calcium. D shows the appearance of a normal blood vessel wall which has layered structure.

Based on this description, we construct a set of eight (real-valued) features for each pixel in the image. We compute these features using a three-dimensional (3D) neighborhood centered on the pixel of interest. The third dimension comes from neighboring frames (human analysts will often use adjacent frames when annotating a frame). In these features, $\sigma$ represents the standard deviation of the intensity values within a 3D neighborhood.

**Distance to lumen ($D_l$):** This is a measure of the distance of the center pixel from the lumen border (i.e. the wall of the blood vessel). This feature helps identify lipid plaques since they are typically within a fibrous plaque as above.

**Beam penetration ($D_d$)** – This is a measure of the length of the beam from the lumen border to the back-border (the border beyond which the near infrared beam does not reach and the signal is at baseline). It depends on tissue type, thus can distinguish between plaques. This feature is invariant for pixels across an A-line but varies across A-lines.

**Mean Intensity ($\bar{I}$):** This represents the average signal intensity of the different plaque types within the 3D neighborhood. As can be seen from Figure 3, this is a very distinctive feature.

**Homogeneity (H):** This is a local coefficient of variation, ($\sigma / \bar{I}$). It helps in distinguishing between heterogeneous intensity regions and homogeneous intensity regions.

**Relative Smoothness of Intensity (S)**: This is defined as: $S = 1 - 1/(1+\sigma^2)$. S is 0 for constant intensity regions and it approaches 1 for large deviations in intensity values.

**Entropy (E):** Entropy is another measure of the variability of the signal intensity within the respective plaque type regions. To compute it, we construct a histogram of the intensity distribution within a 3D-neighborhood. Then entropy is defined as:

$$E = -\sum_{i=0}^{L-1} p(z_i)\log_2 p(z_i),$$

where $p(z_i)$ is the probability of the intensity level $z_i$, $i$=1,…,L for L bins in the histogram of intensity levels. It is expected that within homogeneous regions the entropy will be low and within heterogeneous regions it will be high. Similar features as these are often used in image processing applications [138].

The final two features we use are *optical parameters*. These features are based on models of light transmission and reflectance described below.

**Attenuation coefficient, $\mu_t$** – This feature measures the rate at which the signal intensity drops off within the tissue. Calcified plaque has lower attenuation, and as a result, IVOCT can see deeper into these tissues, compared to lipid where IVOCT does not see as deeply. For this reason, the attenuation coefficient (or penetration depth) gives useful information about plaque types.

**Incident intensity, $I_0$** – This represents the backscattering characteristics of the plaque at the point where the light touches it. This feature is excellent at distinguishing fibrous plaques, which are very reflective.

In order to estimate $I_o$ and $\mu_t$, we modeled the OCT signal as Lambert-Beer exponential decay function [175] , with the addition of baseline $I_{baseline}$ to account for noise and other sources that elevate the expected signal.

$$I_d(r) = I_0 T(r) S(r) \exp(-\mu_t r) + I_{baseline} \tag{4.4}$$

Here *T(r)* is the longitudinal point spread function which describes the shape and focal point of the beam and thus affects the contrast of the image, and *S(r)* is the Gaussian coherence function which describes the signal roll-off with depth [75] . In order to identify the unknown parameters in these two functions, we use nonlinear optimization over their unknown variables. After estimating *T(r)* and *S(r)*, and subtracting the baseline

intensity, we use least squares estimation to find the unknowns $I_o$ and $\mu_t$ for each separate A-line [106] . We verified these estimates by fabricating *phantom* (realistic imitations) blood vessels with known plaque types and checking the estimates against measured values in these cases.

## 6.4 The Plaque-Type Classifier

After extracting features from pixels in our OCT images, we then train a support vector machine (SVM) [145] with a radial basis function (RBF) kernel for classification of the individual pixels. The SVM is a state-of-the-art classification method. It is widely used due to its high accuracy, ability to deal with high-dimensional data, and flexibility in modeling diverse data sources. We use a standard SVM formulation (omitting details due to space). Given that we are interested in classifying three different plaque types, we use a one-versus-rest (OVR) approach for multi-class classification. There are two parameters which must be input to the SVM: C, the regularization parameter that trades off margin size and training error, and γ, the RBF kernel's bandwidth. In our experiments, we select these parameters using an internal 5-fold stratified cross validation loop and a two-dimensional grid search.

## 6.5 Empirical Evaluation

We now describe experiments to test our hypothesis that the system we described will be able to accurately and efficiently classify different plaque types from OCT images.

The clinical images (*in-vivo*) that we use were selected from the database available at our institutions. The images consist of 35 IVOCT pullbacks of the Left

Anterior Descending (LAD) and the Left Circumflex (LCX) coronary arteries of patients acquired prior to stent implantation, with a total of 287 images across 35 patients. An expert cardiologist on our team then labeled volumes of interest (VOIs) as belonging to one of the three plaque types in the images. The expert marked the VOIs of a particular plaque type using freehand brush strokes. On the clinical images the expert annotated 311 VOIs (roughly equal number from each plaque type). VOIs were of various sizes and shapes. Most consisted of 2-5 image frames, 50-200 A-lines, and 20-50 sample points in each A-line.

We also acquired a second set of 106 images from blood vessels used in cadaver studies. Since in this case the blood vessels can be extracted and cryogenically frozen and imaged, they are much easier to label very accurately for the expert. However, since this is *ex-vivo*, we do not use these images for training our classifiers, but use them to validate the [1]results. We call these images "Cryo-images" below to distinguish them from the previous set.

Next, we preprocess all images for speckle noise reduction, baseline subtraction, catheter optical system correction, and catheter eccentricity correction. We segment the lumen and the back-border using dynamic programming. To do this, we use a cost function from prior work [119] . An example of the results of the back-border segmentation is shown in Figure 35 in both ($r$-$\theta$) view and ($x$-$y$) view. Segmenting the image in this way is important because (i) the regions of interest are contained between these borders and the rest of the pixels do not contain any relevant information, and (ii) it

enables us to properly compute the distance to the lumen and the beam penetration depth discussed above, which are important signals for different plaque types.

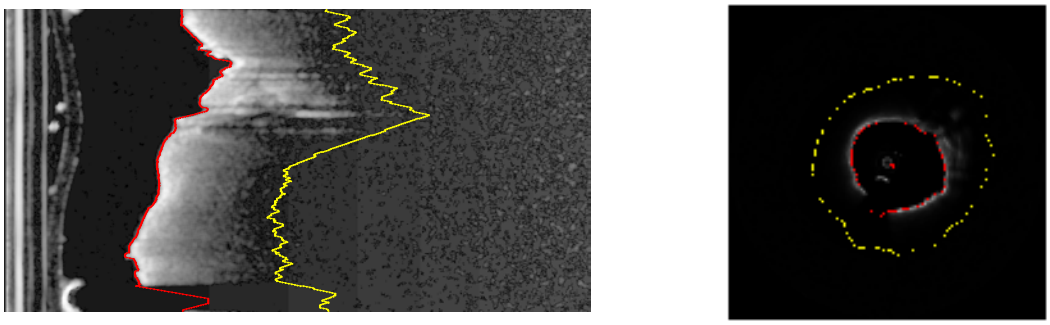

(a) (b)

Figure 35: An illustration of back border segmentation (yellow line) along with lumen segmentation (red line) in a typical clinical image in both views. (a) is the polar image and (b) is the x-y image. The yellow line is broken due to view conversion). Asterisk marks the guide-wire shadowing artifact.

Next, we generate features by scanning the annotated VOIs in the image pixel by pixel. For each pixel, we construct a 7 x 11 x 3 neighborhood (0.035mm x 0.055mm x 0.6mm) around it. As long as the neighborhood is within the VOI, the features of the box are computed as explained above and the values are assigned to the pixel. In the cryo-images (images that did not take part in the training at all), we generated features for *all pixels* between border regions in a similar way.

For cross validation we use the processed images with a *leave-one-pullback-out* strategy. Here, in each iteration, we hold out all the data from one pullback as the test set and use the remaining 34 pullbacks as the training set. This mimics practical usage where the system will operate on novel pullbacks and is more stringent than using random folds. In a second experiment, we ran the trained classifiers on the cryo-images (these were not used at all during training/cross validation). We ran our experiments on a 64-bit Windows 7 machine with 3$^{rd}$ generation Intel Core i7 and 16 GB RAM.

## 6.6 Results and Discussion

The Receiver Operating Curves (ROC) for each OVR classifier from the cross validation experiment is shown in Figure 36. The summary statistics are shown in Table 12, where the accuracy, sensitivity and specificity are noted at the optimal operating point along the curves. The ROC describes the system's behavior for a range of confidence threshold settings and enables the cardiologist (the end user) to decide on weighting the false positives (FP) and false negatives (FN) unequally (a very desirable property according to our expert).

| | CALCIUM | LIPID | FIBROUS |
|---|---|---|---|
| ACCURACY | 92.2±6.28% | 96.95±2.79% | 96.17±4.0% |
| SENSITIVITY | 93.0±2.58% | 98.95±2.35% | 94.28±5.23% |
| SPECIFICITY | 96.5±3.39% | 93.65±2.77% | 95.89±2.18% |
| AUC | 0.9837 | 0.9947 | 0.9959 |

Table 12: Performance measures: Area under ROC and the accuracy, sensitivity and specificity at the optimal operating point on the ROC curves.

The overall accuracy results averaged over 35 folds are shown in Table 13. As can be seen from all of these results, our approach has excellent accuracy for all three plaque types. In fact, across the 35 folds, the median accuracy for all three plaque types is 100%, indicating that our classifiers are (in most cases) able to perfectly separate the plaque types using the features we designed. In a few folds, the accuracy is lower than 100%. We conjecture that this is because some pullbacks have many more images associated with them than others. When such a pullback is held out, the training set size becomes much smaller, and yields a classifier with lower accuracy.

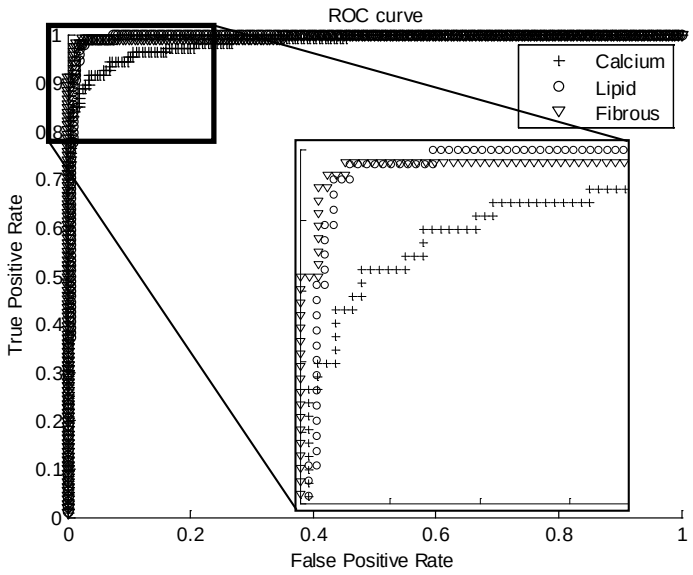


Figure 36: ROC curve for all three plaque types. Area Under the Curve (AUC) values are 0.9837, 0.9947 and 0.9959 for calcium, lipid and fibrous respectively.

In the second experiment, we ran our trained classifier on the cryo-images. We also ran a baseline approach following [141]. This approach used beam attenuation estimates from a layer model applied to single A-lines and 2D texture and geometric measures as features for classification with the added requirement of manual region of interest selection for analysis. These results are shown in Table 14. Here the "Other" row corresponds to pixels in these images that belong to none of the three plaque types. The accuracy of the approach in this case is lower, possibly because these are ex-vivo images which have somewhat different characteristics from the training set. However, our approach still outperforms the state of the art. Further, these values are still at a very useful level according our expert. In particular, cardiologists now divide an image into quadrants and simply state whether a quadrant contains a certain plaque type. If we use

this as a performance measure, our current approach has perfect accuracy on the cryo-images.

| | ACCURACY | MEDIAN ACC. |
|---|---|---|
| OVERALL | 90.70±8.28% | |
| CALCIUM | 92.14±10.74% | 100% |
| LIPID | 96.40±8.87% | 100% |
| FIBROUS | 100%±0.0% | 100% |

Table 13: Accuracy results for leave-one-pullback-out experiment

| | OUR APPROACH | BASELINE |
|---|---|---|
| OVERALL | 81.15% | 69.4% |
| CALCIUM | 97.62% | 66.88% |
| LIPID | 87.65% | 67.07% |
| FIBROUS | 97.39% | 77.95% |
| OTHER | 77.96% | 30.46% |

Table 14: Accuracy results for Cryo-images.

The results also indicate that in some cases some plaque types may be confused with others. For example, the average intensity of a lipid region may be very close to that of calcium. However, they may still be separable due to the fact that the lipid's attenuation coefficient is much higher.

To confirm our intuitive understanding of the plaques' characteristics we performed a *leave-one-feature-out* experiment. In this experiment, we ran the classifier using all of the features and noted the accuracy measures (as shown in Table 13). We then removed each feature at a time to see the impact on the accuracy. We found that removing the attenuation parameter had the biggest impact on the lipid accuracy reducing it down to 92.4±8.87% while removing the average intensity feature, had a significant effect on the fibrous' accuracy and uncertainty (down to 95.2%±10.75). In addition to high accuracy, our approach was also efficient at classification. Each test fold (on average 200,000 datapoints) was classified in 0.0366 seconds by our implementation. This facilitates future real-time usage.

Finally, we consider whether an automatic classification procedure such as this can be useful in reducing the amount of time taken to process images in a clinical setting. In an initial experiment, we found that cardiologists would spend approximately 5 hours analyzing a section of a blood vessel. We then created a tool (Figure 37) with our classifier built in. The cardiologist would run the classifier for a new image and then, using the tool, analyze the results and correct some of the errors in the predictions. We found that this process took at most an hour, a reduction of 80%. This effort reduction indicates that improving the tool will make it deployable in the near future.

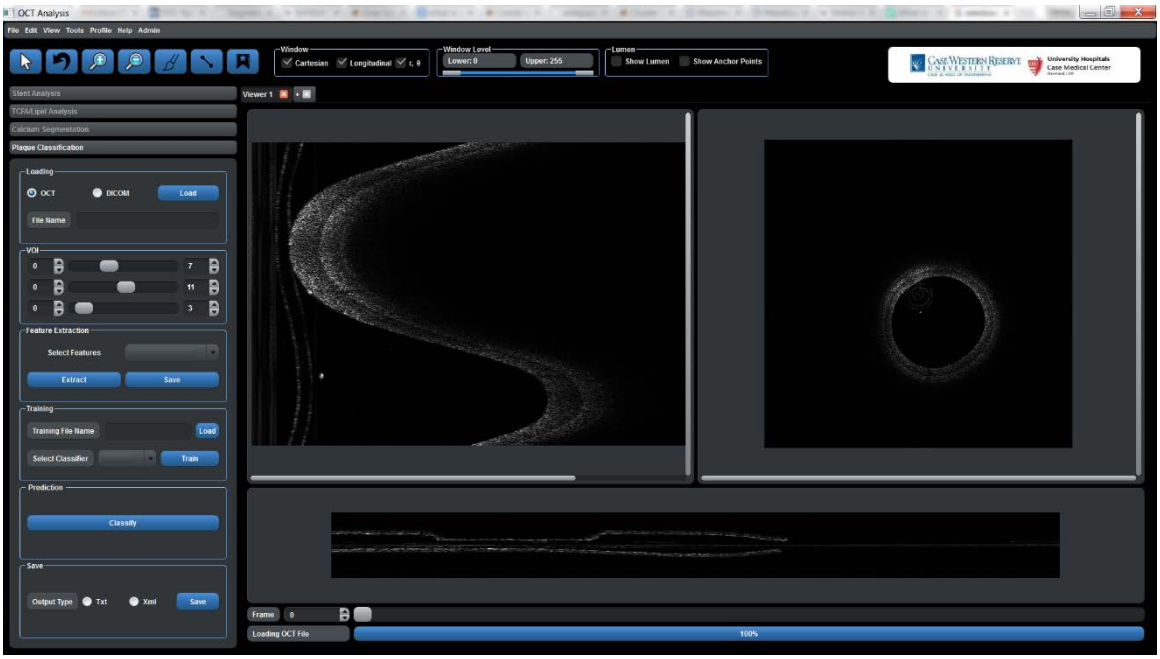


Figure 37: User Interface of Editing tool.

## 6.7 Conclusion

In this chapter, we have discussed an important emerging application: an automated approach to early plaque detection in blood vessels. Our approach analyzes OCT images to solve this task. Using a carefully designed feature set, we show that an SVM with an RBF kernel is a high-accuracy classifier for this task. Our results are of significant impact

on this important problem [100] with implications for early diagnosis of cardiovascular disease. In future work, we plan to work on further improving our classification tool and integrating it with a real-time 3D visualization module which will be able to quantify (volume, area covered, etc.) the presence of calcified regions. This can help in decision making regarding stent implantation and pre-implantation treatment (e.g. directional atherectomy). We also plan to add an explanatory module to help explain the automated classification process to the cardiologists, and accept feedback in an active learning environment.

# Chapter 7 Summary and Future Work

This dissertation presents multiple machine-learning-based algorithms for fully automated, on-line and off-line plaque image analysis using IVOCT. We investigated and developed a variety of image analysis algorithms for automated quantitative diagnosis of CAD for the purpose of intervention planning. On the one hand, we developed an algorithm suitable for common IVOCT image analysis tasks in research labs. On the other hand, we developed an algorithm which can be used in the clinic as a tool for the purpose of treatment planning decision support visualizations and quantifications. The algorithms have been validated using a large number of clinical datasets with the combination of, arguably, the most accurate ground truth available for IVOCT, cryo-images. The algorithms have been proven to be robust and their scalability to larger datasets can be done easily.

In Chapter 1, CAD and related imaging and image processing technologies, in particular OCT and IVOCT image analysis, were introduced. The ever-increasing demand for new imaging methods that can provide additional information about the coronary wall to better characterize and stratify high-risk plaques and to guide interventional and pharmacologic management of patients with coronary artery disease brought about the IVOCT. While there are a number of imaging modalities that facilitate the assessment of coronary artery pathology, it is shown that IVOCT is the first modality with the necessary resolution to identify and follow CAD development. The IVOCT is shown to be valuable for assessment of superficial vascular features, such as superficial atherosclerotic plaques. A brief review of the IVOCT principles was also given. Then, we

discussed the major topic of this dissertation, IVOCT image analysis, its unmet needs, and gave a detailed review of the relevant previous work done in the field.

In Chapter 2 we discuss algorithms for computation and verification of plaque optical properties of the three main plaque types and compared the results to blood vessel phantoms designed for this purpose. We based our analysis approach on robust statistical measures and showed that the observation that the optical properties can be instrumental as discriminative features which can be used to numerically distinguish between the main three plaque types is correct.

We further enhance the notion of plaque separation in Chapter 3 where we describe a complete processing pipeline designed to further enhance the IVOCT image quality enabling accurate and efficient feature extraction for the purpose of creating automated machine learning methods for plaque discrimination.

In Chapter 4 we propose the SVM as a machine learning method to be used as a classifier for off-line plaque classification. We have shown that a careful feature design, conforming to qualitative plaque characteristics, along with clever design of classifier parameters (i.e. thresholding of probabilities) can achieve very accurate classification performance. We used cryo-imaging as ground truth for validation and verification of our method and showed that clinically-useful metrics can be derived from our results.

Superficial calcified plaques (CP) can strongly affect the successful implantation of stents and today, is the most widely treated plaque in the clinic. In Chapter 5 we developed a close-to-real-time method for calcified plaque segmentation. We achieve real-time performance by not imposing any constraints on, or requiring any a priori knowledge of, the catheter type, IVOCT machine type or any other conditions under

which the images were acquired. Automatically classifying CP under such general conditions is a very demanding task. However, we show that the proposed novel algorithm, based on probability distribution of pixel responses, is highly accurate and efficient.

Chapter 6 introduces the software that packages most of the developed algorithms in a single comprehensive application whose architecture is focused towards web-based service to be access by an interest party as SaaS (Software as a Service) application. Being offered on the web, we also added the functionality of study creation, cloud storage, medical image transfer and hosting, automated image analysis tools, clinical trial management and collaboration tools. These tools provide all of the necessary means required for the secure storage, analysis, reporting and data management required in any kind of clinical-related interaction among medical professionals.

## 7.1 Future Work

The main emphasis and accomplishments of this dissertation was to enable automated IVOCT image analysis for the purpose of intervention planning, however, being in its infancy stage, IVOCT image analysis has many unmet needs. Below, we discuss some important topics for future directions from the aspect, which we believe, will push the field forward to practical implementation. However, it is important to note that other issues such as neointima hyperplasia (NIH) formation analysis, macrophage accumulation measurements etc., which are extremely important subjects to study, are not discussed since such discussion is done in other places (e.g. [71]). Furthermore, we

developed software which will be offered as a web service (using the Software as a service, Saas model) in the future.

### *7.1.1 Atlas for IVOCT*

One of the main issues that needs to be addressed by the IVOCT research community is the creation of high quality Atlas. Here, an atlas refers to a set of IVOCT images, a corresponding cryo-image/histology and expert annotation mask. Because IVOCT images can vary significantly, and when combined with expert annotation disagreements on plaque interpretation and annotation, a very different ground-truth results. Such a pool of images would serve to enhance the reproducibility and reliability of future findings. Today, researchers do not have the means to perform quality comparison with competing methods, thus a claim for "success" of a certain method is always local and subjective. Case Western Reserve University and its collaborator, University Hospitals Core lab, are at a unique position to create such an atlas. The atlas should also contain cryo-images and corresponding images of IVOCT (both from cadavers), thus providing a potential researcher a tool to perform validation on their own. The atlas can also be expanded to specific models for a population of images with parameters that are learned from a training dataset and so on. The main point here is to enable reasonable means for comparison and analysis to anyone, regardless of their ability to access an IVOCT dataset source.

### *7.1.2 Stent Analysis*

There have been numerous research activities addressing the issue of stent analysis [83, 84, 176]. However, to our knowledge, none of the researchers have addressed the issue

of real-time performance. We believe that the proposed algorithm discussed in Chapter 5 has the potential to be successful in stent analysis. The application of the algorithm has the advantage of automatic feature creation, thus, can cope with metallic stent (which appear as very bright spots in the IVOCT image) as well as non-metallic stents (whose appearance may vary). Bio absorbable stents [177] use degradable polymers instead of metals. When imaged with IVOCT, bio absorbable stents exhibit very different characteristics from metallic stents. For instance, one type of bio absorbable stent, BVS stent, has a box-like shape at baseline and may change the appearance thereafter before being fully absorbed by the tissue [177]. Different bio absorbable stents may have different appearances, a characteristic which is ideally, solved with automatic feature generation approach as discuss in Chapter 5. To our knowledge, in the research community today, only metallic stent analysis is investigated [83].

### *7.1.3 Quantitative Measurements*

Methods for quantitative measurements of the blood vessel structure are important for future application of OCT technology. One aspect is the identification of normally structured vessel wall. This means that reliable methods for identifying intima-media border (IEM) as well as media-adventitia border (EEM) have to be developed to ensure proper quantification.

### *7.1.4 Parallel Processing and GPU-Accelerated Image Processing*

Feature extraction, training and classification methods using machine learning techniques are commonly applied in data analysis such as in this dissertation. Despite their success, as shown above, in terms of modeling and accuracy performance it is known that some of

these techniques are computationally bound as input sample size and model complexity are increased. Investigating opportunities for potential performance improvements is therefore of great importance if these techniques are to be applied to much larger data volumes expected from current and future intravascular modalities.

Acceleration of classification as well as feature extraction using many-core devices will be the first natural step, where utilizing the GPU platform should also be considered. The development approach and optimization steps that should be taken to maximize the performance should be flexible enough to allow for various classification algorithms to be used. It should enable to process three-dimensional medical imaging so that it is not limited to IVOCT, but any 3D data source (IVUS, CT MRI etc.).

Offloading computationally intensive sections of machine learning classification techniques to many-core devices is more beneficial for higher volumes of input data and for increasing model complexity. Many-core implementations can offer a platform to improve discrimination capabilities of a given method by parallelizing repeated applications of the feature extraction process as well as the training process to determine optimal input parameters. In addition, GPU kernels can be processed concurrently which would allow workloads to be multiplexed either on the same dataset or on disjointed workloads to provide a computationally efficient acceleration service for the application.

To illustrate what we mean, we will use the SVM algorithm used in Chapter 3 as an example. We believe that a successful implementation will make 3D IVOCT plaque classification a suitable application to be used in a clinical application setting taking it beyond “research-only”.

One of the main tasks in feature extraction for multi-class SVM (Chapter 3) was the calculation of the optical attenuation parameter, $\mu$. To do it, we had to perform two main operations, line fitting and sorting. The computational complexity of the line fitting is $O(C^2n)$ where C is the number of features (in our case, it's one since we compute only the attenuation), n is the number of points to be fitted, and in the sorting step it is O(n) if the range of image values is small, e.g. the typical (0,..., 255), since the sort can be implemented as BINSORT. The point is that computation times vary widely, but in the current implementation, we use serial process and do not use the GPU. This means that this single operation of finding the attenuation can be cut in half, just by using two separate processes. We believe that multi-core computer with clever GPU utilization will create a real-time classification algorithm which can be used in a clinical setting. Further, in the classification step, as discussed in [178] and shown in Figure 38, the GPU-based SVM performance improvement is also evident, especially as we increase the number of voxels (in the figure, named "vectors") to be analyzed.

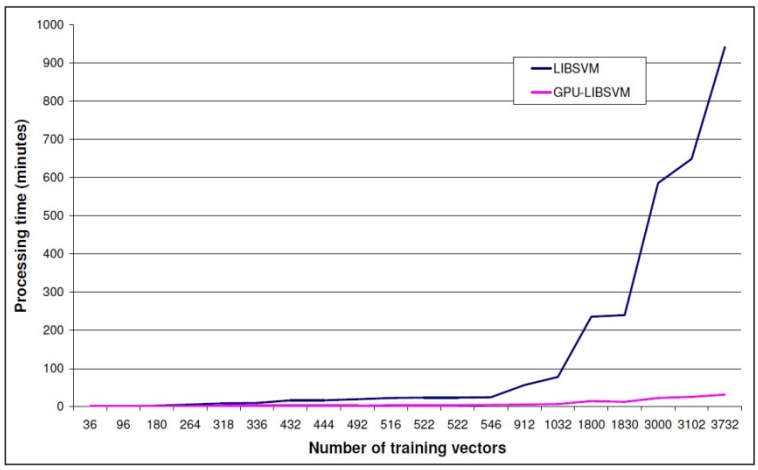


Figure 38: LIBSVM GPU-based implementation expected improvement. GPU-accelerated LIBSVM gives a performance gain depending on the size of input data set. This gain is increasing dramatically with the size of the dataset (source: http://mklab.iti.gr/project/GPU-LIBSVM)

# References


[1] N. CDC, "Underlying Cause of Death 1999-2013 on CDC WONDER Online Database. Data are from the Multiple Cause of Death Files, 1999-2013, as compiled from data provided by the 57 vital statistics jurisdictions through the Vital Statistics Cooperative Program. Accessed Feb. 3, 2015.," *Google*, released 2015.

[2] C. Emslie, "Women, men and coronary heart disease: a review of the qualitative literature," *J Adv Nurs*, vol. 51, pp. 382-95, Aug 2005.

[3] N. Alie, M. Eldib, Z. A. Fayad, and V. Mani, "Inflammation, Atherosclerosis, and Coronary Artery Disease: PET/CT for the Evaluation of Atherosclerosis and Inflammation," *Clin Med Insights Cardiol*, vol. 8, pp. 13-21, 2014.

[4] R. Virmani, A. P. Burke, A. Farb, and F. D. Kolodgie, "Pathology of the vulnerable plaque," *J Am Coll Cardiol*, vol. 47, pp. C13-8, Apr 18 2006.

[5] G. N. Levine, E. R. Bates, J. C. Blankenship, S. R. Bailey, J. A. Bittl, B. Cercek, *et al.*, "2015 ACC/AHA/SCAI Focused Update on Primary Percutaneous Coronary Intervention for Patients With ST-Elevation Myocardial Infarction: An Update of the 2011 ACCF/AHA/SCAI Guideline for Percutaneous Coronary Intervention and the 2013 ACCF/AHA Guideline for the Management of ST-Elevation Myocardial Infarction: A Report of the American College of Cardiology/American Heart Association Task Force on Clinical Practice Guidelines and the Society for Cardiovascular Angiography and Interventions," *Circulation*, Oct 21 2015.

[6] D. E. Kandzari, A. S. Kini, D. Karmpaliotis, J. W. Moses, P. E. Tummala, J. A. Grantham, *et al.*, "Safety and Effectiveness of Everolimus-Eluting Stents in Chronic Total Coronary Occlusion Revascularization: Results From the EXPERT CTO Multicenter Trial (Evaluation of the XIENCE Coronary Stent, Performance, and Technique in Chronic Total Occlusions)," *JACC: Cardiovascular Interventions*, vol. 8, pp. 761-769, 2015.

[7] R. Virmani, F. D. Kolodgie, A. P. Burke, A. V. Finn, H. K. Gold, T. N. Tulenko, *et al.*, "Atherosclerotic plaque progression and vulnerability to rupture: angiogenesis as a source of intraplaque hemorrhage," *Arterioscler Thromb Vasc Biol*, vol. 25, pp. 2054-61, Oct 2005.

[8] P. Greenland, R. O. Bonow, B. H. Brundage, M. J. Budoff, M. J. Eisenberg, S. M. Grundy, *et al.*, "ACCF/AHA 2007 clinical expert consensus document on coronary artery calcium scoring by computed tomography in global cardiovascular risk assessment and in evaluation of patients with chest pain: a report of the American College of Cardiology Foundation Clinical Expert Consensus Task Force (ACCF/AHA Writing Committee to Update the 2000 Expert Consensus Document on Electron Beam Computed Tomography) developed in collaboration with the Society of Atherosclerosis Imaging and Prevention and the Society of Cardiovascular Computed Tomography," *J Am Coll Cardiol*, vol. 49, pp. 378-402, Jan 23 2007.

[9] L. Wexler, B. Brundage, J. Crouse, R. Detrano, V. Fuster, J. Maddahi, *et al.*, "Coronary artery calcification: pathophysiology, epidemiology, imaging

methods, and clinical implications. A statement for health professionals from the American Heart Association. Writing Group," *Circulation,* vol. 94, pp. 1175-92, Sep 1 1996.

[10] M. J. Pletcher, J. A. Tice, M. Pignone, and W. S. Browner, "Using the coronary artery calcium score to predict coronary heart disease events - A systematic review and meta-analysis," *Archives of Internal Medicine,* vol. 164, pp. 1285-1292, Jun 28 2004.

[11] A. P. Burke, D. K. Weber, F. D. Kolodgie, A. Farb, A. J. Taylor, and R. Virmani, "Pathophysiology of calcium deposition in coronary arteries," *Herz,* vol. 26, pp. 239-44, Jun 2001.

[12] R. Detrano, A. D. Guerci, J. J. Carr, D. E. Bild, G. Burke, A. R. Folsom, *et al.*, "Coronary calcium as a predictor of coronary events in four racial or ethnic groups," *New England Journal of Medicine,* vol. 358, pp. 1336-1345, Mar 27 2008.

[13] R. Virmani, A. P. Burke, F. D. Kolodgie, and A. Farb, "Vulnerable plaque: the pathology of unstable coronary lesions," *J Interv Cardiol,* vol. 15, pp. 439-46, Dec 2002.

[14] K. Nishida, T. Kimura, K. Kawai, I. Miyano, Y. Nakaoka, S. Yamamoto, *et al.*, "Comparison of outcomes using the sirolimus-eluting stent in calcified versus non-calcified native coronary lesions in patients on-versus not on-chronic hemodialysis (from the j-Cypher registry)," *The American journal of cardiology,* vol. 112, pp. 647-655, 2013.

[15] H. Fujimoto, M. Nakamura, and H. Yokoi, "Impact of Calcification on the Long-Term Outcomes of Sirolimus-Eluting Stent Implantation-Subanalysis of the Cypher Post-Marketing Surveillance Registry," *Circulation Journal,* vol. 76, pp. 57-64, 2012.

[16] E. Cavusoglu, A. S. Kini, J. D. Marmur, and S. K. Sharma, "Current status of rotational atherectomy," *Catheterization and cardiovascular interventions,* vol. 62, pp. 485-498, 2004.

[17] M. A. Costa, D. J. Angiolillo, M. Tannenbaum, M. Driesman, A. Chu, J. Patterson, *et al.*, "Impact of stent deployment procedural factors on long-term effectiveness and safety of sirolimus-eluting stents (final results of the multicenter prospective STLLR trial)," *The American journal of cardiology,* vol. 101, pp. 1704-1711, 2008.

[18] D. Chamié, H. G. Bezerra, G. F. Attizzani, H. Yamamoto, T. Kanaya, G. T. Stefano, *et al.*, "Incidence, predictors, morphological characteristics, and clinical outcomes of stent edge dissections detected by optical coherence tomography," *JACC: Cardiovascular Interventions,* vol. 6, pp. 800-813, 2013.

[19] G. S. Mintz, S. E. Nissen, W. D. Anderson, S. R. Bailey, R. Erbel, P. J. Fitzgerald, *et al.*, "American College of Cardiology clinical expert consensus document on standards for acquisition, measurement and reporting of intravascular ultrasound studies (IVUS) 33: A report of the American College of Cardiology Task Force on clinical expert consensus documents developed in collaboration with the european society of cardiology endorsed by the society of cardiac angiography and interventions," *Journal of the American College of Cardiology,* vol. 37, pp. 1478-1492, 2001.

[20] P. G. Yock and P. J. Fitzgerald, "Intravascular ultrasound: state of the art and future directions," *Am J Cardiol,* vol. 81, pp. 27E-32E, Apr 9 1998.
[21] F. Prati, E. Arbustini, A. Labellarte, B. Dal Bello, L. Sommariva, M. T. Mallus, *et al.*, "Correlation between high frequency intravascular ultrasound and histomorphology in human coronary arteries," *Heart,* vol. 85, pp. 567-570, May 2001.
[22] M. Yamagishi, M. Terashima, K. Awano, M. Kijima, S. Nakatani, S. Daikoku, *et al.*, "Morphology of vulnerable coronary plaque: insights from follow-up of patients examined by intravascular ultrasound before an acute coronary syndrome," *Journal of the American College of Cardiology,* vol. 35, pp. 106-111, 2000.
[23] G. J. Tearney, I. K. Jang, and B. E. Bouma, "Optical coherence tomography for imaging the vulnerable plaque," *Journal of biomedical optics,* vol. 11, pp. 021002-021002, 2006.
[24] K. Jansen, G. van Soest, and A. F. van der Steen, "Intravascular photoacoustic imaging: a new tool for vulnerable plaque identification," *Ultrasound Med Biol,* vol. 40, pp. 1037-48, Jun 2014.
[25] J. Bec, D. M. Ma, D. R. Yankelevich, J. Liu, W. T. Ferrier, J. Southard, *et al.*, "Multispectral fluorescence lifetime imaging system for intravascular diagnostics with ultrasound guidance: in vivo validation in swine arteries," *J Biophotonics,* vol. 7, pp. 281-5, May 2014.
[26] G. J. Ughi, J. Verjans, A. M. Fard, H. Wang, E. Osborn, T. Hara, *et al.*, "Dual modality intravascular optical coherence tomography (OCT) and near-infrared fluorescence (NIRF) imaging: a fully automated algorithm for the distance-calibration of NIRF signal intensity for quantitative molecular imaging," *Int J Cardiovasc Imaging,* vol. 31, pp. 259-68, Feb 2015.
[27] J. Li, T. Ma, J. Jing, J. Zhang, P. M. Patel, K. Kirk Shung, *et al.*, "Miniature optical coherence tomography-ultrasound probe for automatically coregistered three-dimensional intracoronary imaging with real-time display," *J Biomed Opt,* vol. 18, p. 100502, Oct 2013.
[28] F. J. Van der Meer, D. J. Faber, D. M. B. Sassoon, M. C. Aalders, G. Pasterkamp, and T. G. van Leeuwen, "Localized measurement of optical attenuation coefficients of atherosclerotic plaque constituents by quantitative optical coherence tomography," *Medical Imaging, IEEE Transactions on,* vol. 24, pp. 1369-1376, 2005.
[29] N. A. Patel, D. L. Stamper, and M. E. Brezinski, "Review of the ability of optical coherence tomography to characterize plaque, including a comparison with intravascular ultrasound," *Cardiovasc Intervent Radiol,* vol. 28, pp. 1-9, Jan-Feb 2005.
[30] E. Regar, J. A. Schaar, E. Mont, R. Virmani, and P. W. Serruys, "Optical coherence tomography," *Cardiovasc Radiat Med,* vol. 4, pp. 198-204, Oct-Dec 2003.
[31] D. Huang, E. A. Swanson, C. P. Lin, J. S. Schuman, W. G. Stinson, W. Chang, *et al.*, "Optical coherence tomography," *Science,* vol. 254, pp. 1178-81, Nov 22 1991.

[32] H. Yabushita, B. E. Bouma, S. L. Houser, H. T. Aretz, I. K. Jang, K. H. Schlendorf, *et al.*, "Characterization of human atherosclerosis by optical coherence tomography," *Circulation,* vol. 106, pp. 1640-1645, 2002.

[33] G. J. Tearney, S. A. Boppart, B. E. Bouma, M. E. Brezinski, N. J. Weissman, J. F. Southern, *et al.*, "Scanning single-mode fiber optic catheter-endoscope for optical coherence tomography," *Opt Lett,* vol. 21, pp. 543-5, Apr 1 1996.

[34] G. J. Tearney, M. E. Brezinski, B. E. Bouma, S. A. Boppart, C. Pitris, J. F. Southern, *et al.*, "In vivo endoscopic optical biopsy with optical coherence tomography," *Science,* vol. 276, pp. 2037-9, Jun 27 1997.

[35] R. Leitgeb, C. K. Hitzenberger, and A. F. Fercher, "Performance of fourier domain vs. time domain optical coherence tomography," *Optics Express,* vol. 11, pp. 889-894, Apr 21 2003.

[36] M. A. Choma, M. V. Sarunic, C. H. Yang, and J. A. Izatt, "Sensitivity advantage of swept source and Fourier domain optical coherence tomography," *Optics Express,* vol. 11, pp. 2183-2189, Sep 8 2003.

[37] S. H. Yun, G. J. Tearney, J. F. de Boer, N. Iftimia, and B. E. Bouma, "High-speed optical frequency-domain imaging," *Optics Express,* vol. 11, pp. 2953-2963, Nov 3 2003.

[38] J. F. de Boer, B. Cense, B. H. Park, M. C. Pierce, G. J. Tearney, and B. E. Bouma, "Improved signal-to-noise ratio in spectral-domain compared with time-domain optical coherence tomography," *Optics Letters,* vol. 28, pp. 2067-2069, Nov 1 2003.

[39] S. H. Yun, G. J. Tearney, B. J. Vakoc, M. Shishkov, W. Y. Oh, A. E. Desjardins, *et al.*, "Comprehensive volumetric optical microscopy in vivo," *Nat Med,* vol. 12, pp. 1429-33, Dec 2006.

[40] H. M. Garcia-Garcia, N. Gonzalo, E. Regar, and P. W. Serruys, "Virtual histology and optical coherence tomography: from research to a broad clinical application," *Heart,* vol. 95, pp. 1362-74, Aug 2009.

[41] N. Gonzalo, P. W. Serruys, T. Okamura, H. M. van Beusekom, H. M. Garcia-Garcia, G. van Soest, *et al.*, "Optical coherence tomography patterns of stent restenosis," *Am Heart J,* vol. 158, pp. 284-93, Aug 2009.

[42] G. J. Tearney, S. Waxman, M. Shishkov, B. J. Vakoc, M. J. Suter, M. I. Freilich, *et al.*, "Three-Dimensional Coronary Artery Microscopy by Intracoronary Optical Frequency Domain Imaging," *Jacc-Cardiovascular Imaging,* vol. 1, pp. 752-761, Nov 2008.

[43] I. K. Jang, B. E. Bouma, D. H. Kang, S. J. Park, S. W. Park, K. B. Seung, *et al.*, "Visualization of coronary atherosclerotic plaques in patients using optical coherence tomography: comparison with intravascular ultrasound," *Journal of the American College of Cardiology,* vol. 39, pp. 604-609, 2002.

[44] H. G. Bezerra, M. A. Costa, G. Guagliumi, A. M. Rollins, and D. I. Simon, "Intracoronary optical coherence tomography: a comprehensive reviewclinical and research applications," *JACC: Cardiovascular Interventions,* vol. 2, pp. 1035-1046, 2009.

[45] M. Terashima, H. Kaneda, and T. Suzuki, "The Role of Optical Coherence Tomography in Coronary Intervention," *Korean Journal of Internal Medicine,* vol. 27, pp. 1-12, Mar 2012.

[46] P. Barlis, P. W. Serruys, N. Gonzalo, W. J. van der Giessen, P. J. de Jaegere, and E. Regar, "Assessment of culprit and remote coronary narrowings using optical coherence tomography with long-term outcomes," *American Journal of Cardiology,* vol. 102, pp. 391-395, Aug 15 2008.

[47] I. K. Jang, G. J. Tearney, B. MacNeill, M. Takano, F. Moselewski, N. Iftima, *et al.*, "In vivo characterization of coronary atherosclerotic plaque by use of optical coherence tomography," *Circulation,* vol. 111, pp. 1551-1555, 2005.

[48] S. Chia, O. C. Raffel, M. Takano, G. J. Tearney, B. E. Bouma, and I. K. Jang, "In-vivo comparison of coronary plaque characteristics using optical coherence tomography in women vs. men with acute coronary syndrome," *Coronary Artery Disease,* vol. 18, pp. 423-427, Sep 2007.

[49] T. Kubo, T. Imanishi, S. Takarada, A. Kuroi, S. Ueno, T. Yamano, *et al.*, "Assessment of culprit lesion morphology in acute myocardial infarction - Ability of optical coherence tomography compared with intravascular ultrasound and coronary angioscopy," *Journal of the American College of Cardiology,* vol. 50, pp. 933-939, Sep 4 2007.

[50] O. C. Raffel, G. J. Tearney, D. D. Gauthier, E. F. Halpern, B. E. Bouma, and I. K. Jang, "Relationship between a systemic inflammatory marker, plaque inflammation, and plaque characteristics determined by intravascular optical coherence tomography," *Arteriosclerosis Thrombosis and Vascular Biology,* vol. 27, pp. 1820-1827, Aug 2007.

[51] B. E. Bouma, G. J. Tearney, H. Yabushita, M. Shishkov, C. R. Kauffman, D. D. Gauthier, *et al.*, "Evaluation of intracoronary stenting by intravascular optical coherence tomography," *Heart,* vol. 89, pp. 317-320, Mar 2003.

[52] K. Toutouzas, S. Vaina, M. I. Riga, and C. Stefanadis, "Evaluation of dissection after coronary stent implantation by intravascular optical coherence tomography," *Clin Cardiol,* vol. 32, pp. E47-8, Jul 2009.

[53] E. Regar, J. Schaar, and P. W. Serruys, "Images in cardiology. Acute recoil in sirolimus eluting stent: real time, in vivo assessment with optical coherence tomography," *Heart,* vol. 92, p. 123, Jan 2006.

[54] T. Sawada, J. Shite, T. Shinke, S. Watanabe, H. Otake, D. Matsumoto, *et al.*, "Persistent malapposition after implantation of sirolimus-eluting stent into intramural coronary hematoma - Optical coherence tomography observations," *Circulation Journal,* vol. 70, pp. 1515-1519, Nov 2006.

[55] E. Regar, H. M. M. van Beusekom, W. J. van der Giessen, and P. W. Serruys, "Optical coherence tomography findings at 5-year follow-up after coronary stent implantation," *Circulation,* vol. 112, pp. E345-E346, Dec 6 2005.

[56] P. Barlis, J. Tanigawa, and C. Di Mario, "Coronary bioabsorbable magnesium stent: 15-month intravascular ultrasound and optical coherence tomography findings," *European Heart Journal,* vol. 28, pp. 2319-2319, Oct 2007.

[57] R. Gupta, O. C. Raffel, and I. K. Jang, "Severe intimal hyperplasia after sirolimus eluting stent deployment: evaluation by optical coherence tomography," *BMJ Case Rep,* vol. 2009, p. bcr2006091918, 2009.

[58] S. Li, L. Gai, T. Yang, L. Zhang, X. Xu, Q. Bai, *et al.*, "Evaluation of long-term follow-up with neointimal coverage and stent apposition after sirolimus-eluting

stent implantation by optical coherence tomography," *Catheter Cardiovasc Interv,* vol. 81, pp. 768-75, Apr 2013.

[59] D. Matsumoto, J. Shite, T. Shinke, H. Otake, Y. Tanino, D. Ogasawara, *et al.*, "Neointimal coverage of sirolimus-eluting stents at 6-month follow-up: evaluated by optical coherence tomography," *European Heart Journal,* vol. 28, pp. 961-967, 2007.

[60] E. Camenzind, P. G. Steg, and W. Wijns, "Stent thrombosis late after implantation of first-generation drug-eluting stents: a cause for concern," *Circulation,* vol. 115, pp. 1440-55; discussion 1455, Mar 20 2007.

[61] T. Kume, T. Akasaka, T. Kawamoto, N. Watanabe, E. Toyota, Y. Neishi, *et al.*, "Assessment of coronary arterial plaque by optical coherence tomography," *The American journal of cardiology,* vol. 97, pp. 1172-1175, 2006.

[62] B. D. MacNeill, I. K. Jang, B. E. Bouma, N. Iftimia, M. Takano, H. Yabushita, *et al.*, "Focal and multi-focal plaque macrophage distributions in patients with acute and stable presentations of coronary artery disease," *J Am Coll Cardiol,* vol. 44, pp. 972-9, Sep 1 2004.

[63] J. Rieber, O. Meissner, G. Babaryka, S. Reim, M. Oswald, A. Koenig, *et al.*, "Diagnostic accuracy of optical coherence tomography and intravascular ultrasound for the detection and characterization of atherosclerotic plaque composition in ex-vivo coronary specimens: a comparison with histology," *Coron Artery Dis,* vol. 17, pp. 425-30, Aug 2006.

[64] G. Tearney, I. Jang, and B. Bouma, "Evidence of cholesterol crystals in atherosclerotic plaque by optical coherence tomographic (OCT) imaging," *Eur Heart J,* vol. 24, p. 1462, 2003.

[65] G. J. Tearney, H. Yabushita, S. L. Houser, H. T. Aretz, I. K. Jang, K. H. Schlendorf, *et al.*, "Quantification of macrophage content in atherosclerotic plaques by optical coherence tomography," *Circulation,* vol. 107, pp. 113-119, 2003.

[66] M. J. Suter, S. K. Nadkarni, G. Weisz, A. Tanaka, F. A. Jaffer, B. E. Bouma, *et al.*, "Intravascular optical imaging technology for investigating the coronary artery," *JACC Cardiovasc Imaging,* vol. 4, pp. 1022-39, Sep 2011.

[67] T. Kume, T. Akasaka, T. Kawamoto, H. Okura, N. Watanabe, E. Toyota, *et al.*, "Measurement of the thickness of the fibrous cap by optical coherence tomography," *American Heart Journal,* vol. 152, Oct 2006.

[68] F. D. Kolodgie, A. P. Burke, A. Farb, H. K. Gold, J. Yuan, J. Narula, *et al.*, "The thin-cap fibroatheroma: a type of vulnerable plaque: the major precursor lesion to acute coronary syndromes," *Curr Opin Cardiol,* vol. 16, pp. 285-92, Sep 2001.

[69] S. Waxman, F. Ishibashi, and J. E. Muller, "Detection and treatment of vulnerable plaques and vulnerable patients: novel approaches to prevention of coronary events," *Circulation,* vol. 114, pp. 2390-411, Nov 28 2006.

[70] K. Fujii, H. Hao, M. Shibuya, T. Imanaka, M. Fukunaga, K. Mild, *et al.*, "Accuracy of OCT, Grayscale IVUS, and Their Combination for the Diagnosis of Coronary TCFA An Ex Vivo Validation Study," *Jacc-Cardiovascular Imaging,* vol. 8, pp. 451-460, Apr 2015.

[71] G. J. Tearney and e. al., "Consensus Standards for Acquisition, Measurement, and Reporting of Intravascular Optical Coherence Tomography Studies A Report From the International Working Group for Intravascular Optical Coherence Tomography Standardization and Validation," *Journal of the American College of Cardiology,* vol. 59, pp. 1058-1072, Mar 20 2012.

[72] J. E. Phipps, D. Vela, T. Hoyt, D. L. Halaney, J. J. Mancuso, L. M. Buja, *et al.*, "Macrophages and Intravascular OCT Bright Spots A Quantitative Study," *Jacc-Cardiovascular Imaging,* vol. 8, pp. 63-72, Jan 2015.

[73] A. Taruya, A. Tanaka, T. Nishiguchi, Y. Matsuo, Y. Ozaki, M. Kashiwagi, *et al.*, "Vasa Vasorum Restructuring in Human Atherosclerotic Plaque Vulnerability A Clinical Optical Coherence Tomography Study," *Journal of the American College of Cardiology,* vol. 65, pp. 2469-2477, Jun 16 2015.

[74] S. Waxman, M. I. Freilich, M. J. Suter, M. Shishkov, S. Bilazarian, R. Virmani, *et al.*, "A Case of Lipid Core Plaque Progression and Rupture at the Edge of a Coronary Stent: Elucidating the Mechanisms of Drug-Eluting Stent Failure," *Circulation-Cardiovascular Interventions,* vol. 3, pp. 193-196, Apr 2010.

[75] G. Van Soest, E. Regar, S. Koljenovi+„, G. L. J. H. van Leenders, N. Gonzalo, S. van Noorden, *et al.*, "Atherosclerotic tissue characterization in vivo by optical coherence tomography attenuation imaging," *Journal of biomedical optics,* vol. 15, pp. 011105-011105, 2010.

[76] G. Guagliumi, G. Musumeci, V. Sirbu, H. G. Bezerra, N. Suzuki, L. Fiocca, *et al.*, "Optical coherence tomography assessment of in vivo vascular response after implantation of overlapping bare-metal and drug-eluting stents," *JACC Cardiovasc.Interv.*, vol. 3, pp. 531-539, 2010.

[77] G. Guagliumi, V. Sirbu, G. Musumeci, H. G. Bezerra, A. Aprile, H. Kyono, *et al.*, "Strut coverage and vessel wall response to a new-generation paclitaxel-eluting stent with an ultrathin biodegradable abluminal polymer: Optical Coherence Tomography Drug-Eluting Stent Investigation (OCTDESI)," *Circ.Cardiovasc.Interv.*, vol. 3, pp. 367-375, 2010.

[78] G. F. Attizzani and H. G. Bezerra, "Contemporary assessment of stent strut coverage by OCT," *Int J Cardiovasc Imaging,* vol. 29, pp. 23-7, Jan 2013.

[79] D. Chamie, Z. Wang, H. Bezerra, A. M. Rollins, and M. A. Costa, "Optical Coherence Tomography and Fibrous Cap Characterization," *Curr Cardiovasc Imaging Rep,* vol. 4, pp. 276-283, Aug 2011.

[80] H. Lu, M. Gargesha, Z. Wang, D. Chamie, G. F. Attizzani, T. Kanaya, *et al.*, "Automatic stent detection in intravascular OCT images using bagged decision trees," *Biomedical optics express,* vol. 3, pp. 2809-2824, 2012.

[81] H. Lu, M. Gargesha, Z. Wang, D. Chamie, G. F. Attizani, T. Kanaya, *et al.*, "Automatic stent strut detection in intravascular OCT images using image processing and classification technique," in *SPIE Medical Imaging*, 2013, pp. 867015-867015-8.

[82] Z. Wang, M. W. Jenkins, H. Bezerra, M. Costa, D. Wilson, and A. Rollins, "Single-shot stent segmentation in intravascular OCT pullbacks," in *Biomedical Optics*, 2012, p. BTu4B. 5.

[83] H. Lu, M. Gargesha, Z. Wang, D. Chamie, G. F. Attizani, T. Kanaya, *et al.*, "Automatic stent detection in intravascular OCT images using bagged decision trees," *Biomedical Optics Express*, vol. 3, pp. 2809-2824, 2012.
[84] Z. Wang, M. Jenkins, G. Linderman, H. Bezerra, Y. Fujino, M. Costa, *et al.*, "3-D Stent Detection in Intravascular OCT Using a Bayesian Network and Graph Search," *IEEE Trans Med Imaging*, Feb 24 2015.
[85] W. Wijns, J. Shite, M. R. Jones, S. W.-L. Lee, M. J. Price, F. Fabbiocchi, *et al.*, "Optical coherence tomography imaging during percutaneous coronary intervention impacts physician decision-making: ILUMIEN I study," *European heart journal*, vol. 36, pp. 3346-3355, 2015.
[86] G. T. Stefano, H. G. Bezerra, E. Mehanna, H. Yamamoto, Y. Fujino, W. Wang, *et al.*, "Unrestricted utilization of frequency domain optical coherence tomography in coronary interventions," *The international journal of cardiovascular imaging*, vol. 29, pp. 741-752, 2013.
[87] P. R. Liebson and L. W. Klein, "Intravascular Ultrasound in Coronary Atherosclerosis - a New Approach to Clinical-Assessment," *American Heart Journal*, vol. 123, pp. 1643-1660, Jun 1992.
[88] Z. Wang, "Volumetric quantification of fibrous caps using intravascular optical coherence tomography," *Biomedical Optics Express*, vol. 3, p. 1413, 2012.
[89] G. J. Tearney, E. Regar, T. Akasaka, T. Adriaenssens, P. Barlis, H. G. Bezerra, *et al.*, "Consensus Standards for Acquisition, Measurement, and Reporting of Intravascular Optical Coherence Tomography Studies," *Journal of the American College of Cardiology*, vol. 59, pp. 1058-1072, Mar 20 2012.
[90] K. P. Murphy, *Machine learning : a probabilistic perspective*. Cambridge, Mass.: MIT Press, 2012.
[91] C. M. Bishop, *Pattern recognition and machine learning*. New York: Springer, 2006.
[92] K. Person, "On Lines and Planes of Closest Fit to System of Points in Space. Philiosophical Magazine, 2, 559-572," ed, 1901.
[93] R. A. Fisher, "The use of multiple measurements in taxonomic problems," *Annals of eugenics*, vol. 7, pp. 179-188, 1936.
[94] B. Thompson, *Canonical correlation analysis : uses and interpretation*. Beverly Hills: Sage Publications, 1984.
[95] J. R. Quinlan, "Induction of decision trees," *Machine learning*, vol. 1, pp. 81-106, 1986.
[96] K. Kira and L. A. Rendell, "The feature selection problem: Traditional methods and a new algorithm," in *AAAI*, 1992, pp. 129-134.
[97] R. O. Duda, P. E. Hart, and D. G. Stork, *Pattern classification*, 2nd ed. New York: Wiley, 2001.
[98] R. Tibshirani, "Regression shrinkage and selection via the lasso," *Journal of the Royal Statistical Society. Series B (Methodological)*, pp. 267-288, 1996.
[99] D. J. Hand, *Construction and assessment of classification rules* vol. 15: Wiley Chichester, 1997.
[100] K. Wagstaff, "Machine learning that matters," *arXiv preprint arXiv*, p. 1206.4656, 2012.

[101] Z. Wang, M. W. Jenkins, H. Bezerra, M. Costa, D. Wilson, and A. Rollins, "Single-shot stent segmentation in intravascular OCT pullbacks."
[102] C. Xu, J. M. Schmitt, S. G. Carlier, and R. Virmani, "Characterization of atherosclerosis plaques by measuring both backscattering and attenuation coefficients in optical coherence tomography," *Journal of biomedical optics,* vol. 13, pp. 034003-034003, 2008.
[103] C. V. B. Lambros S. Athanasiou, George Rigas, Antonis I. Sakellarios, Themis P. Exarchos, Panagiotis K. Siogkas, Andrea Ricciardi, Katerina K. Naka, Michail I. Papafaklis, Lampros K. Michalis, Francesco Prati, Dimitrios I. Fotiadis, "Methodology for fully automated segmentation and plaque characterization in intracoronary optical coherence tomography images," 2014.
[104] C. t. Bisaillon, M. L. Dufour, and G. Lamouche, "Artery phantoms for intravascular optical coherence tomography: healthy arteries," *Biomedical Optics Express,* vol. 2, pp. 2599-2613, 2011.
[105] G. Lamouche, B. F. Kennedy, K. M. Kennedy, C. E. Bisaillon, A. Curatolo, G. Campbell, *et al.,* "Review of tissue simulating phantoms with controllable optical, mechanical and structural properties for use in optical coherence tomography," *Biomedical Optics Express,* vol. 3, p. 1381, 2012.
[106] M. Gargesha, R. Shalev, D. Prabhu, K. Tanaka, A. M. Rollins, M. Costa, *et al.*, "Parameter Estimation of Atherosclerotic Tissue Optical Properties from 3D Intravascular OCT " *SPIE Journal of Medical Imaging,* vol. 2, p. 14, January, 2, 2015 2015.
[107] E. Falk, P. K. Shah, and V. Fuster, "Coronary plaque disruption," *Circulation,* vol. 92, pp. 657-71, Aug 1 1995.
[108] J. S. Lee, J. H. Wen, T. L. Ainsworth, K. S. Chen, and A. J. Chen, "Improved Sigma Filter for Speckle Filtering of SAR Imagery," *Ieee Transactions on Geoscience and Remote Sensing,* vol. 47, pp. 202-213, Jan 2009.
[109] A. Lopes, R. Touzi, and E. Nezry, "Adaptive Speckle Filters and Scene Heterogeneity," *Ieee Transactions on Geoscience and Remote Sensing,* vol. 28, pp. 992-1000, Nov 1990.
[110] J. Rogowska and M. E. Brezinski, "Evaluation of the adaptive speckle suppression filter for coronary optical coherence tomography imaging," *Ieee Transactions on Medical Imaging,* vol. 19, pp. 1261-1266, Dec 2000.
[111] J. M. Schmitt, S. H. Xiang, and K. M. Yung, "Speckle in optical coherence tomography: An overview," *Saratov Fall Meeting '98: Light Scattering Technologies for Mechanics, Biomedicine, and Material Science,* vol. 3726, pp. 450-461, 1999.
[112] J. W. Goodman, "Some Fundamental Properties of Speckle," *Journal of the Optical Society of America,* vol. 66, pp. 1145-1150, 1976.
[113] J. S. Lee, "Speckle analysis and smoothing of synthetic aperture radar images," *Computer graphics and image processing,* vol. 17, pp. 24-32, 1981.
[114] C. Xu, J. M. Schmitt, T. Akasaka, T. Kubo, and K. Huang, "Automatic detection of stent struts with thick neointimal growth in intravascular optical coherence tomography image sequences," *Phys Med Biol,* vol. 56, pp. 6665-75, Oct 21 2011.

[115] H. Lu, M. Gargesha, Z. Wang, D. Chamie, G. F. Attizani, T. Kanaya, *et al.*, "Automatic stent strut detection in intravascular OCT images using image processing and classification technique," pp. 867015-867015.

[116] R. Huber, D. C. Adler, and J. G. Fujimoto, "Buffered Fourier domain mode locking: Unidirectional swept laser sources for optical coherence tomography imaging at 370,000 lines/s," *Opt Lett,* vol. 31, pp. 2975-7, Oct 15 2006.

[117] D. J. Faber, F. J. Van der Meer, M. C. G. Aalders, and T. G. van Leeuwen, "Quantitative measurement of attenuation coefficients of weakly scattering media using optical coherence tomography," *Optics Express,* vol. 12, pp. 4353-4365, 2004.

[118] D. Levitz, L. Thrane, M. H. Frosz, P. E. Andersen, C. B. Andersen, J. Valanciunaite, *et al.*, "Determination of optical scattering properties of highly-scattering media in optical coherence tomography images," *Optics Express,* vol. 12, pp. 249-259, Jan 26 2004.

[119] Z. Wang, H. Kyono, H. G. Bezerra, D. L. Wilson, M. A. Costa, and A. M. Rollins, "Automatic segmentation of intravascular optical coherence tomography images for facilitating quantitative diagnosis of atherosclerosis," pp. 78890N-78890N.

[120] J. M. Schmitt, S. H. Xiang, and K. M. Yung, "Speckle in optical coherence tomography," *Journal of Biomedical Optics,* vol. 4, pp. 95-105, Jan 1999.

[121] J. S. Lee, "Digital Image-Enhancement and Noise Filtering by Use of Local Statistics," *Ieee Transactions on Pattern Analysis and Machine Intelligence,* vol. 2, pp. 165-168, 1980.

[122] K. M. Yung, S. L. Lee, and J. M. Schmitt, "Phase-domain processing of optical coherence tomography images," *J Biomed Opt,* vol. 4, pp. 125-36, Jan 1999.

[123] R. C. Gonzalez and R. E. Woods, *Digital image processing*, 3rd ed. Upper Saddle River, N.J.: Prentice Hall, 2008.

[124] M. Bashkansky and J. Reintjes, "Statistics and reduction of speckle in optical coherence tomography," *Optics Letters,* vol. 25, pp. 545-547, Apr 15 2000.

[125] G. J. Ughi, T. Adriaenssens, P. Sinnaeve, W. Desmet, and J. D'Hooge, "Automated tissue characterization of in vivo atherosclerotic plaques by intravascular optical coherence tomography images," *Biomed.Opt.Express,* vol. 4, pp. 1014-1030, 2013.

[126] J. A. Finegold, P. Asaria, and D. P. Francis, "Mortality from ischaemic heart disease by country, region, and age: statistics from World Health Organisation and United Nations," *Int J Cardiol,* vol. 168, pp. 934-45, Sep 30 2013.

[127] K. C. Briley-Saebo, P. X. Shaw, W. J. Mulder, S.-H. Choi, E. Vucic, J. G. S. Aguinaldo, *et al.*, "Targeted molecular probes for imaging atherosclerotic lesions with magnetic resonance using antibodies that recognize oxidation-specific epitopes," *Circulation,* vol. 117, pp. 3206-3215, 2008.

[128] S. Takarada, T. Imanishi, T. Kubo, T. Tanimoto, H. Kitabata, N. Nakamura, *et al.*, "Effect of statin therapy on coronary fibrous-cap thickness in patients with acute coronary syndrome: assessment by optical coherence tomography study," *Atherosclerosis,* vol. 202, pp. 491-7, Feb 2009.

[129] K. Komukai, T. Kubo, H. Kitabata, Y. Matsuo, Y. Ozaki, S. Takarada, *et al.*, "Effect of Atorvastatin Therapy on Fibrous Cap Thickness in Coronary

Atherosclerotic Plaque as Assessed by Optical Coherence Tomography," *Journal of the American College of Cardiology,* vol. 64, pp. 2207-2217, Dec 2 2014.

[130] L. Vignali, E. Solinas, and E. Emanuele, "Research and clinical applications of optical coherence tomography in invasive cardiology: a review," *Curr Cardiol Rev,* vol. 10, pp. 369-76, Nov 2014.

[131] M. Z. Galon, Z. Wang, H. G. Bezerra, P. A. Lemos, A. Schnell, D. L. Wilson, *et al.*, "Differences determined by optical coherence tomography volumetric analysis in non‐culprit lesion morphology and inflammation in ST‐segment elevation myocardial infarction and stable angina pectoris patients," *Catheterization and Cardiovascular Interventions,* vol. 85, pp. E108-E115, 2015.

[132] G. J. Tearney and B. E. Bouma, "Atherosclerotic plaque characterization by spatial and temporal speckle pattern analysis," *Opt Lett,* vol. 27, pp. 533-5, Apr 1 2002.

[133] Ronny Shalev, Madhusudhana Gargesha, David Prabhu, Kentaro Tanaka, Andrew M. Rollins, Guy Lamouche, *et al.*, "Processing to determine optical parameters of atherosclerotic disease from phantom and clinical intravascular OCT 3D pullbacks," *Submitted to JMI, November 2015,* 2015.

[134] Z. Wang, H. Kyono, H. G. Bezerra, H. Wang, M. Gargesha, C. Alraies, *et al.*, "Semiautomatic segmentation and quantification of calcified plaques in intracoronary optical coherence tomography images," *Journal of biomedical optics,* vol. 15, pp. 061711-061711, 2010.

[135] A. G. Roy, S. Conjeti, S. G. Carlier, A. Konig, A. Kastrati, P. K. Dutta, *et al.*, "Bag of forests for modelling of tissue energy interaction in optical coherence tomography for atherosclerotic plaque susceptibility assessment," in *Biomedical Imaging (ISBI), 2015 IEEE 12th International Symposium on*, 2015, pp. 428-431.

[136] R. Shalev, M. Gargesha, D. Prabhu, K. Tanaka, A. M. Rollins, M. Costa, *et al.*, "Validation of parameter estimation methods for determining optical properties of atherosclerotic tissues in intravascular OCT," *Proceedings of SPIE,* vol. 9037, March, 2014.

[137] R. C. Gonzalez, R. E. Woods, and S. L. Eddins, *Digital Image processing using MATLAB*, 2nd ed. S.I.: Gatesmark Pub., 2009.

[138] R. C. Gonzalez, R. E. Woods, and S. L. Eddins, *Digital Image processing using MATLAB®*, 2nd ed. United States: Gatesmark Publishing, 2009.

[139] K. W. Gossage, T. S. Tkaczyk, J. J. Rodriguez, and J. K. Barton, "Texture analysis of optical coherence tomography images: feasibility for tissue classification," *J Biomed Opt,* vol. 8, pp. 570-5, Jul 2003.

[140] R. M. Haralick, Shanmuga.K, and I. Dinstein, "Textural Features for Image Classification," *Ieee Transactions on Systems Man and Cybernetics,* vol. Smc3, pp. 610-621, 1973.

[141] G. J. Ughi, T. Adriaenssens, P. Sinnaeve, W. Desmet, and J. D'hooge, "Automated tissue characterization of in vivo atherosclerotic plaques by intravascular optical coherence tomography images," *Biomedical Optics Express,* vol. 4, pp. 1014-1030, Jul 1 2013.

[142] D. A. Clausi, "An analysis of co-occurrence texture statistics as a function of grey level quantization," *Canadian Journal of remote sensing,* vol. 28, pp. 45-62, 2002.
[143] B. E. Boser, Isabelle M. Guyon, and Vladimir N. Vapnik, "A training algorithm for optimal margin classifiers," *Proceedings of the fifth annual workshop on Computational learning theory. ACM*, 1992.
[144] B. Schölkopf, C. J. C. Burges, and A. J. Smola, *Advances in kernel methods : support vector learning*. Cambridge, Mass.: MIT Press, 1999.
[145] N. Cristianini and J. Shawe-Taylor, *An introduction to support vector machines : and other kernel-based learning methods*. Cambridge ; New York: Cambridge University Press, 2000.
[146] V. N. Vapnik, *Statistical learning theory*. New York: Wiley, 1998.
[147] K. Hajian-Tilaki, "Receiver operating characteristic (ROC) curve analysis for medical diagnostic test evaluation," *Caspian journal of internal medicine,* vol. 4, p. 627, 2013.
[148] W. J. Youden, "Index for Rating Diagnostic Tests," *Cancer,* vol. 3, pp. 32-35, 1950.
[149] O. Salvado, D. Roy, M. Heinzel, E. McKinley, and D. Wilson, "3D Cryo-Section/Imaging of Blood Vessel Lesions for Validation of MRI Data," *Proc SPIE Int Soc Opt Eng,* vol. 6142, pp. 377-386, Mar 1 2006.
[150] C.-W. Hsu, C.-C. Chang, and C.-J. Lin, "A practical guide to support vector classification," ed, 2003.
[151] J. R. Jensen, F. Qiu, and K. Patterson, "A neural network image interpretation system to extract rural and urban land use and land cover information from remote sensor data," *Geocarto International,* vol. 16, pp. 21-30, 2001.
[152] D. Stalling, M. Westerhoff, and H.-C. Hege, "38–Amira: a highly interactive system for visual data analysis," *Visualization Handbook,* 2005.
[153] M. Greiner, D. Pfeiffer, and R. Smith, "Principles and practical application of the receiver-operating characteristic analysis for diagnostic tests," *Preventive veterinary medicine,* vol. 45, pp. 23-41, 2000.
[154] K. A. Spackman, "Signal detection theory: Valuable tools for evaluating inductive learning," in *Proceedings of the sixth international workshop on Machine learning*, 1989, pp. 160-163.
[155] F. J. Provost and T. Fawcett, "Analysis and visualization of classifier performance: Comparison under imprecise class and cost distributions," in *KDD*, 1997, pp. 43-48.
[156] F. Provost and T. Fawcett, "Robust classification systems for imprecise environments," in *AAAI/IAAI*, 1998, pp. 706-713.
[157] C. K. Chow, "On optimum recognition error and reject tradeoff," *Information Theory, IEEE Transactions on,* vol. 16, pp. 41-46, 1970.
[158] P. J. Fitzgerald, T. A. Ports, and P. G. Yock, "Contribution of Localized Calcium Deposits to Dissection after Angioplasty - an Observational Study Using Intravascular Ultrasound," *Circulation,* vol. 86, pp. 64-70, Jul 1992.
[159] K. H. Henneke, E. Regar, A. Konig, F. Werner, V. Klauss, J. Metz, *et al.*, "Impact of target lesion calcification on coronary stent expansion after rotational atherectomy," *American Heart Journal,* vol. 137, pp. 93-99, Jan 1999.

[160] I. Zeb, D. Li, K. Nasir, S. S. Mao, and M. Budoff, "Coronary Artery Calcium Progression as a Strong Predictor of Adverse Future Coronary Events," *Journal of the American College of Cardiology*, vol. 61, pp. E984-E984, Mar 12 2013.

[161] R. A. Kronmal, R. L. McClelland, R. Detrano, S. Shea, J. A. Lima, M. Cushman, *et al.*, "Risk factors for the progression of coronary artery calcification in asymptomatic subjects - Results from the Multi-Ethnic Study of Atherosclerosis (MESA)," *Circulation*, vol. 115, pp. 2722-2730, May 29 2007.

[162] R. Shalev, D. Prabhu, D. Nakamura, S. Nishino, A. M. Rollins, H. G. Bezerra, *et al.*, "Machine Learning Plaque Classification from Intravascular OCT Image Pullbacks," 2016 Submitted.

[163] G. J. Tearney, E. Regar, T. Akasaka, T. Adriaenssens, P. Barlis, H. G. Bezerra, *et al.*, "Consensus Standards for Acquisition, Measurement, and Reporting of Intravascular Optical Coherence Tomography Studies: a report from the International Working Group for Intravascular Optical Coherence Tomography Standardization and Validation
" *Journal of the American College of Cardiology*, vol. 59, pp. 1058-1072, Mar 20 2012.

[164] O. G. Cula and K. J. Dana, "3D texture recognition using bidirectional feature histograms," *International Journal of Computer Vision*, vol. 59, pp. 33-60, Aug 2004.

[165] T. Leung and J. Malik, "Representing and recognizing the visual appearance of materials using three-dimensional textons," *International Journal of Computer Vision*, vol. 43, pp. 29-44, 2001.

[166] J. Canny, "A Computational Approach to Edge-Detection," *Ieee Transactions on Pattern Analysis and Machine Intelligence*, vol. 8, pp. 679-698, Nov 1986.

[167] R. Shalev, D. Prabhu, D. Nakamura, S. Nishino, H. G. Bezerra, S. Ray, *et al.*, "Machine Learning Plaque Classification from Intravascular OCT Image Pullbacks," To be submitted in February of 2016 submitted.

[168] J. Malik, S. Belongie, T. Leung, and J. B. Shi, "Contour and texture analysis for image segmentation," *International Journal of Computer Vision*, vol. 43, pp. 7-27, 2001.

[169] C. C. Chang and C. J. Lin, "LIBSVM: A Library for Support Vector Machines," *Acm Transactions on Intelligent Systems and Technology*, vol. 2, 2011.

[170] Y. Q. Chen, X. S. Zhou, and T. S. Huang, "One-class SVM for learning in image retrieval," *2001 International Conference on Image Processing, Vol I, Proceedings*, pp. 34-37, 2001.

[171] A. S. Agatston, W. R. Janowitz, F. J. Hildner, N. R. Zusmer, M. Viamonte, and R. Detrano, "Quantification of Coronary-Artery Calcium Using Ultrafast Computed-Tomography," *Journal of the American College of Cardiology*, vol. 15, pp. 827-832, Mar 15 1990.

[172] J. Margolis, J. Chen, Y. Kong, R. Peter, V. Behar, and J. Kisslo, "The diagnostic and prognostic significance of coronary artery calcification. A report of 800 cases," *Radiology*, vol. 137, pp. 609-616, 1980.

[173] S. Mendis, Pekka Puska, and Bo Norrving.,, "Global atlas on cardiovascular disease prevention and control. ," *World Health Organization*, 2011.

[174] G. S. Mintz, J. J. Popma, A. D. Pichard, K. M. Kent, L. F. Satler, Y. C. Chuang, *et al.*, "Patterns of calcification in coronary artery disease. A statistical analysis

of intravascular ultrasound and coronary angiography in 1155 lesions," *Circulation*, vol. 91, pp. 1959-65, Apr 1 1995.

[175] L. V. Wang and H.-i. Wu, *Biomedical optics : principles and imaging*. Hoboken, N.J.: Wiley-Interscience, 2007.

[176] G. J. Ughi, T. Adriaenssens, K. Onsea, P. Kayaert, C. Dubois, M. Coosemans, *et al.*, "Automated stent strut coverage and apposition analysis of in-vivo intra coronary Optical Coherence Tomography images," *Optical Coherence Tomography and Coherence Domain Optical Methods in Biomedicine Xv*, vol. 7889, 2011.

[177] P. W. Serruys, J. A. Ormiston, Y. Onuma, E. Regar, N. Gonzalo, H. M. Garcia-Garcia, *et al.*, "A bioabsorbable everolimus-eluting coronary stent system (ABSORB): 2-year outcomes and results from multiple imaging methods," *Lancet*, vol. 373, pp. 897-910, Mar 14 2009.

[178] A. Athanasopoulos, A. Dimou, V. Mezaris, and I. Kompatsiaris, "GPU acceleration for support vector machines," in *WIAMIS 2011: 12th International Workshop on Image Analysis for Multimedia Interactive Services, Delft, The Netherlands, April 13-15, 2011*, 2011.